ÇUKUROVA UNIVERSITY

INSTITUTE OF NATURAL AND APPLIED SCIENCES

MSc THESIS

Analyzing and Investigating the Dynamics of Land Use and Land Cover (LULC) Transformation using Satellite Data: A Case Study of Adana, Türkiye

Mwila LAMPI

Remote Sensing and Geographic Information Systems Department

April, 2024

ÇUKUROVA UNIVERSITY
INSTITUTE OF NATURAL AND APPLIED SCIENCES

MSc THESIS APPROVAL

Analyzing and Investigating the Dynamics of Land Use and Land Cover (LULC) Transformation using Satellite Data: A Case Study of Adana, Türkiye

---

Mwila LAMPI

Remote Sensing and Geographic Information Systems Department

This Master's Thesis was evaluated by the following Jury Members on xx/xx/xxxx and was approved by unanimity / majority of votes.

Jury : Prof. Dr. Niyazi ARSLAN

: Prof. Dr. Umut ORHAN

: Assoc. Prof. Dr. Aliihsan ŞEKERTEKİN

This Thesis was written in the Department of Remote Sensing and Geographic Information, Institute of Natural and Applied Sciences.

Thesis Number:

Prof. Dr. Sadık DİNÇER
Director Institute of Natural and Applied Sciences

CONTENTS

ABSTRACT I
ÖZ II
GENİŞLETİLMİŞ ÖZET III
ACKNOWLEDGEMENTS VI
LIST OF TABLES VII
LIST OF FIGURES VIII
SYMBOLS AND ABBREVIATIONS XI
1. INTRODUCTION 1
1.1. Background 1
1.2. Literature Study 3
1.2.1. Satellite Data 3
1.2.2. Remote Sensing Techniques 4
1.3. Aim and Research Objectives 5
2. PRELIMINARY WORK 7
2.1. General Studies Related with Remote Sensing 7
2.2. LULC Studies Related to the Local Area 8
2.3. Global Land Cover Maps 9
2.4. Remote Sensing Satellites and Software 10
2.4.1. Remote Sensing Satellites 10
2.4.2. Remote Sensing Software 11
2.4.3. Sentinel 2 Remote Sensing Data Capabilities 12
3. MATERIAL AND METHOD 15
3.1. Material 15
3.1.1. Study Area 16
3.1.2. General Description of the Study Area 17
3.2. Method 18
3.2.1. Index Calculation with Spectral Indices 19
3.2.2. Classification in Remote Sensing 20
3.2.3. Processing with Google Earth Engine (GEE) 21
4. RESULTS AND DISCUSSIONS 33
4.1. NSpectral Indices 33
4.1.1. NDVI Index 34
4.1.2. NDWI Index 41
4.1.3. NDSI Index 47
4.1.4. NDBI Index 54

4.2. LULC Maps 60
4.3. Factors Influencing Accuracy Metrics in Land Cover Classification 79
4.4. Subset Implementation 80
4.4.1. Subset Region 80
4.5. Change Detection 89
4.5.1. Problems Related to Change Detection 91
4.6. Ground Truth Data 92
5. CONCLUSION 105
REFERENCES 107
CURRICULUM VITAE 113

CUKUROVA UNIVERSITY
INSTITUTE OF NATURAL AND APPLIED SCIENCES

MSc THESIS

Analyzing and Investigating the Dynamics of Land Use and Land Cover (LULC) Transformation using Satellite Data: A Case Study of Adana, Turkiye

Mwila LAMPI

Advisor: Prof.Dr. Niyazi ARSLAN

Department of Remote Sensing and Geographic Information Systems

ABSTRACT

The main aim of this research is to analyze and investigate the dynamics of Land Use and Land Cover (LULC) Transformation in Adana, Turkiye on a yearly basis from 2018 to 2022 using Machine Learning (ML) in Google Earth Engine (GEE) and GIS software tools such as ArcGIS Pro for mapping and presentation of results. Sentinel 2A Image collections were used for classification due to their high resolution (10m), wide swath and multi-spectral imaging capabilities. Distinctive and separate supervised classification was done on image collections for 2018, 2019, 2020, 2021 and 2022 using JavaScript in GEE. Seven (7) useful classes namely Water, Trees, Flooded Vegetation, Crops, Built Area, Bare Ground and Rangeland with reference to the ESRI Global Land Cover Map were analyzed and mapped. To achieve high accuracy results, various Supervised Machine Learning Algorithms were tested for the best solution, combined with visual inspection.

The Overall Accuracy and Kappa Statistics for the main region on a yearly basis was 85% and 86% for 2018, 86% and 81% for 2019, 90% and 85% for 2020, 85% and 83% for 2021 and lastly 89% and 83% for 2022 respectively.

However, despite various methods of obtaining accurate results for a large area, discrepancies and misclassifications in the classes with complex pixels and spatial information were observed. To address this problem, a distinctive subset covering key features and geography from the selected region and surrounding region was used to show the trend in changes and obtain better accurate results related to the difference in the classes over time.

The Overall Accuracy and Kappa Statistics of the subset was 91% and 88% for 2018, 88% and 85% for 2019, 90% and 84% for 2020, 89% and 86% for 2021 and finally 85% and 80% for 2022 respectively. The main drivers for the changes in LULC areas were attributed to the expansion of Built-up Areas, Growth in Crop Production, Deforestation and Afforestation and Climate Change related issues.

Keywords: Land Use Land Cover, Sentinel 2A, Machine Learning, GEE

ÇUKUROVA ÜNİVERSİTESİ
FEN BİLİMLERİ ENSTİTÜSÜ

YÜKSEK LİSANS

Uydu Verileri Kullanılarak Arazi Kullanımı ve Arazi Örtüsü (AKAÖ) Dönüşüm Dinamiklerinin İncelenmesi ve Analizi: Adana, Türkiye'de bir Vaka Çalışması

Mwila LAMPI

Danışman: Prof.Dr. Niyazi ARSLAN

Uzaktan Algılama ve Coğrafi Bilgi Sistemleri Anabilim Dalı

ÖZ

Bu araştırmanın temel amacı, haritalama ve sonuçların sunumu için Google Earth Engine (GEE) ve ArcGIS Pro gibi CBS yazılım araçlarında Makine Öğrenimi (ML) kullanarak Adana, Türkiye'deki Arazi Kullanımı ve Arazi Örtüsü (LULC) Dönüşümünün dinamiklerini 2018'den 2022'ye kadar yıllık bazda analiz etmek ve araştırmaktır. Sentinel 2A Görüntü koleksiyonları, yüksek çözünürlük (10m), geniş alan ve çok spektral görüntüleme yetenekleri nedeniyle sınıflandırma için kullanılmıştır. GEE'de JavaScript kullanılarak 2018, 2019, 2020, 2021 ve 2022 görüntü koleksiyonları üzerinde ayırt edici ve ayrı denetimli sınıflandırma yapılmıştır. ESRI Küresel Arazi Örtüsü Haritası referans alınarak Su, Ağaçlar, Taşkın Bitki Örtüsü, Ekinler, Yerleşik Alan, Çıplak Zemin ve Mera olmak üzere yedi (7) faydalı sınıf analiz edilmiş ve haritalanmıştır. Yüksek doğrulukta sonuçlar elde etmek için çeşitli Denetimli Makine Öğrenimi Algoritmaları, görsel inceleme ile birlikte en iyi çözüm için test edilmiştir.

Yıllık bazda ana bölge için Genel Doğruluk ve Kappa İstatistikleri sırasıyla 2018 için %85 ve %86, 2019 için %86 ve %81, 2020 için %90 ve %85, 2021 için %85 ve %83 ve son olarak 2022 için %89 ve %83 olmuştur.

Bununla birlikte, geniş bir alan için doğru sonuçlar elde etmenin çeşitli yöntemlerine rağmen, karmaşık pikseller ve uzamsal bilgiler içeren sınıflarda tutarsızlıklar ve yanlış sınıflandırmalar gözlemlenmiştir. Bu sorunu ele almak için, seçilen bölge ve çevresindeki bölgeden temel özellikleri ve coğrafyayı kapsayan ayırt edici bir alt küme kullanılmıştır.

Anahtar Kelimeler: Arazi kullanımı arazi örtüsü, Sentinel 2A, Makine Öğrenmesi, GEE

GENİŞLETİLMİŞ ÖZET

Çalışmada, analiz için yüksek çözünürlüklü ve doğru sonuçlar sağlayabilen uydu verileri kullanılmıştır. Bu nedenle GEE'de Earth Engine snippet ee.ImageCollection ("COPERNICUS/S2_SR") ile Sentinel-2 MSI (Multispectral Instrument) Level-2A verisi seçilmiştir. Sentinel-2 MSI Seviye-2A verileri, atmosferik etkiler için düzeltilen ve ardından yerüstü yansıma sağlamak için işlenen ham Sentinel-2 MSI Seviye-1C verilerinden türetilen bir uzaktan algılama verisi türüdür. Seviye-2A ürünü atmosferik olarak düzeltilmiş yüzey yansıtma verilerini üretmek için bulut maskeleme ve atmosferik düzeltme gibi daha ileri işleme adımları uygulanarak üretilmektedir.

Sentinel-2 MSI Seviye-2A verileri 10 metreye kadar konumsal çözünürlüğe sahip olup, görünür, yakın kızılötesi ve kısa dalga kızılötesi dalga boyları dahil olmak üzere 13 spektral banttan oluşmaktadır. Bu yüksek konumsal ve spektral çözünürlük, arazi örtüsü ve arazi kullanımı sınıflandırması, bitki örtüsü haritalaması ve çevresel değişikliklerin izlenmesi için idealdir.

Seviye-2A ürünü ayrıca bulut ve su maskeleri gibi sınıflandırma sonuçlarının doğruluğunu artırmaya yardımcı olabilecek ek bilgiler de sağlamaktadır. Ayrıca, veriler ücretsiz olarak kullanılabilmekte ve çeşitli yazılım araçları ve platformları aracılığıyla kolayca erişilebilmektedir.

Genel olarak, Sentinel-2 MSI Seviye-2A verileri, yüksek konumsal ve spektral çözünürlüğünün yanı sıra, erişilebilirliği ve ek bilgileri nedeniyle çok çeşitli uygulamalar için değerli bir kaynak olduğundan araştırma için tercih edilmiştir.

Çalışma ayrıca, 2018'den 2022'ye kadar 5 yıllık bir süre boyunca AKAÖ dönüşümündeki değişiklikleri analiz etmek ve araştırmak için Makine Öğrenimi tekniklerini ve yüksek çözünürlüklü uydu verileri kullanmanın etkinliğini de göstermiştir. AKAÖ dönüşüm sürecini anlamak ve doğru sonuçlar için en iyi yöntemleri kullanmak araştırma boyunca kritik öneme sahipti ve çeşitli hızlı analizler ve deneylerden sonra yalnızca en iyi yöntem seçilmiştir. Çalışma için Maksimum Olabilirlik (ML), Rastgele Orman (RF) ve Destek Vektör Makinesi (SVM) gibi çeşitli Makine Öğrenimi Algoritmaları kullanılmış ve test edilmiştir. Maksimum Olabilirlik Algoritması, eğitim verilerinin istatistiksel özelliklerine dayanarak her bir pikselin belirli bir sınıfa ait olma olasılığını hesaplayan bir sınıflandırıcı olarak tanımlanabilir (Jensen, 1996). Algoritma, her bir pikselin her bir sınıfa ait olma olasılığını, sınıfın istatistiksel parametrelerine dayalı olarak hesaplamak ve böylece pikseli en yüksek olasılığa sahip sınıfa atamak için tasarlanmıştır. Buna karşılık, Rastgele Orman Algoritması, eğitim sırasında bir karar ağaçları havuzu kullanan ve sınıfların modu veya bireysel ağaçların ortalama tahmini olan sınıfı çıkaran bir sınıflandırıcıdır (Breiman, 2001). Destek Vektör Makinesi (DVM) de tanımlanan sınıflar arasındaki marjı maksimize ederken verileri farklı sınıflara ayıran optimum hiper düzlemi belirleyerek çalışan bir algoritmadır (Hastie ve ark., 2009).

Yaygın olarak kullanılan üç (3) Makine Öğrenimi Algoritmasının tümü dikkate alınmış ve test edilmiştir, Rastgele Orman Algoritması, yüksek piksel değerlerine sahip geniş uygulama bölgesine atfedilen gürültülü ve karmaşık verileri işlemedeki sağlamlığı nedeniyle daha iyi ve doğru sonuçlar üretmiştir. Algoritma, sonuçların doğruluğunu artırmak için görsel inceleme ve yanlış sınıflandırılmış piksellerin manuel olarak yeniden sınıflandırılması ile birlikte kullanılmıştır. Sınıflandırmanın performansını değerlendirmek ve sınıflardaki değişimi göstermek için her yıl için Genel Doğruluk ve Kappa İstatistiği hesaplanmıştır.

Ancak (Inoue ve ark., 2020) gibi çeşitli araştırmacıların belirttiği gibi, daha karmaşık ve zaman alıcı olabilen büyük miktarda verinin işlenmesindeki zorluklar gibi çeşitli faktörler nedeniyle büyük alanları sınıflandırmak büyük bir zorluk olabilmektedir. Ayrıca, büyük alanlar; Ağaçlar, Yerleşik Alanlar, Meralar ve Ekinler gibi farklı spektral imzalara sahip farklı türde arazi örtüsü sınıfları içerebildiğinden onları ayırt etmek zorlaşmaktadır (Wulder ve ark., 2016). Bu tür karışık piksellerin varlığı ve bir ROI'de farklı arazi örtüleri arasındaki spektral benzerlik, sınıflandırma sürecini daha da karmaşık hale getirmektedir.

Ayrıca, ilgili çalışma için bir sınıflandırma algoritmasının seçimi, sonuçların doğruluğunu ve eğitim verilerinin kalitesini büyük ölçüde etkilemektedir. Buna ek olarak, büyük alanlar yoğun hesaplama ve önemli hesaplanabilir kaynaklar ve bellek gerektirmektedir (Congalton ve Green, 2019).

Çalışma, geniş bir alana sahip olan Adana'ya odaklandığından, tartışılan tüm yöntemler araştırmanın doğru sonuçları için analiz edilmiştir. Daha doğru sonuçlar elde etmek için çalışılan bölgede bir alt küme seçilmiştir. Bir alt küme elde etmek, sınıflandırma sürecinin hesaplama karmaşıklığının azaltılması ve dolayısıyla eğitim verilerinin kalitesinin artırılması açısından faydalıdır.

Bir alt küme tanımlamak spektral karışıklık, karışık pikseller ve farklı sınıflarla ilişkili spektral imzaların etkilerini büyük ölçüde azaltabilir. Spektral karışıklık, iki veya daha fazla sınıf benzer spektral imzalara sahip olduğunda, karışık pikseller ise bir piksel farklı arazi örtülerinin bir karışımını içerdiğinde meydana gelmektedir (Lu ve Weng, 2007). Seçilen bölgenin alt kümesine odaklanmak, farklı arazi örtüsünün spektral imzalarıyla ilgili sorunları en aza indirmeye yardımcı olmuş ve elde edilen çeşitli eğitim örneklerinin yayılmasını kolaylaştırmıştır. Seçilen bölgeden alınan alt kümede Rastgele Orman Algoritması ile birlikte kullanılan eğitim örnekleri (ROI), sınıflandırmayı daha doğru hale getirmiştir.

Çalışma için uygun Makine Öğrenimi Algoritması ve alt küme başarıyla seçildikten sonra, jeo-mekansal verileri analiz etmek için erişimi kolay ve güçlü araçlar sağlayan bulut tabanlı bir platform olan GEE kullanılmıştır. GEE, çeşitli programlama dilleriyle kullanılabilen kullanıcı dostu etkileşimli bir kod editörü sağlamaktadır. Kolay erişimi ve GEE'de yüklü kod parçacıkları nedeniyle çalışma için birincil programlama dili olan JavaScript seçilmiştir. Ayrıca hem yeni başlayanlar hem de deneyimli programcılar için kullanımı kolaydır.

GEE kod editörü, kullanıcıların kod yazmasına ve çalıştırmasına, çıktıları görmesine ve hataları ayıklamasına olanak tanıyan etkileşimli bir ortam sağlamaktadır. GEE'deki JavaScript şu anda çeşitli araştırmacılar, bilim adamları için Uzaktan Algılama ile ilgili tüm uygulamalarda kolay kodlama olanağı sağlamaktadır. Dil aynı zamanda büyük miktarda veriyi işlemek için çok uygundur ve sağlam hesaplama için optimize edilmiştir. Bu da onu GEE'de büyük veri kümelerini işlemek için çok verimli hale getirmektedir. Ayrıca, verilerin yüklenmesi, işlenmesi ve analiz edilmesi kolay olan yerleşik işlevler ve kütüphaneler de içermektedir.

Yıllık zaman dilimi için tüm analiz ve sınıflandırma, Normalleştirilmiş Fark Bitki Örtüsü İndeksi (NDVI), Normalleştirilmiş Fark Su İndeksi (NDWI), Normalleştirilmiş Fark Kar İndeksi (NDSI) ve Normalleştirilmiş Fark Bina İndeksi (NDBI) gibi spektral indekslerin ortalama değerlerinin elde edilmesi de dahil olmak üzere GEE'de gerçekleştirilmiştir. Bu spektral indeksler, sınıflandırma için doğru eğitim örneklerinin elde edilmesinde çok önemli bir rol oynamıştır. Örneğin, kırmızı ve yakın kızılötesi bantların yansıma değerlerini kullanarak bir bölgedeki bitki örtüsünü tahmin etmek için kullanılan spektral bir indeks olan NDVI, sınıflandırma sonuçlarının doğruluğunu artırmak için GEE'deki eğitim verileri için ekinler ve bitki örtüsü eğitim örneklerini seçmek için kullanılmıştır. Benzer şekilde, bir bölgedeki su kütlelerini tanımlamak için kullanılan spektral bir indeks olan NDWI, göller, nehirler ve su havzaları gibi su kütlelerini tanımlamak için eğitim örneklerini seçmek üzere yeşil ve yakın kızılötesi bantların yansıma değerlerini kullanarak bir bölgedeki su kütlelerini tanımlamak için kullanılmıştır. Ayrıca, NDSI için yeşil ve kısa dalga kızılötesi bantları ve NDBI için kısa dalga kızılötesi ve yakın kızılötesi bantlar kullanılarak sırasıyla kar/buz ve yerleşik alanların analizi gerçekleştirilmiştir. NDSI ve NDBI spektral indeksleri, yerleşik alanların ve karın tanımlanmasında da hayati önem taşıyan eğitim örneklerini toplamak için kullanılmıştır.

GEE'de başarılı bir şekilde sınıflandırıldıktan sonra veriler, haritalama ve sonuçların sunumu için GeoTIFF dosyaları olarak ArcGIS Pro'ya aktarılmıştır. ArcGIS Pro, GEE ile karşılaştırıldığında, hem vektör hem de Raster veri kümelerini analiz etmek için çeşitli seçenekler sunan, ancak büyük miktarda veriyi işlemekle sınırlı olan yazılım tabanlı bir araçtır. Her iki aracı da en iyi şekilde kullanmak için analiz ve sınıflandırma GEE'de, Haritalama ve Sunum ise ArcGIS Pro'da yapılmıştır.

ACKNOWLEDGEMENTS

I would like to express my gratitude and acknowledgement to everyone who had contributed to the successful completion of my thesis entitled "Analyzing and Investigating the Dynamics of Land Use and Land Cover (LULC) Transformation using Satellite Data: A Case Study of Adana, Turkiye".

First and foremost, I am grateful and thankful to my supervisor, Prof.Dr. Niyazi ARSLAN, for his tremendous guidance, support, and constructive feedback throughout the entire research process. His valuable insights and expert advice were instrumental in shaping the direction of my research and ensuring its quality for appropriate results.

My sincere appreciation goes to my mum Jenny Tembo LAMPI, Brother Chilekwa LAMPI and friends for their emotional support and encouragement throughout my academic journey since birth. The love, understanding, and encouragement has been my source of strength and motivation all these years. Their efforts and support have played a crucial role in my academic journey and have contributed to my personal and professional growth. I am deeply grateful for the time, effort, and resources that they have invested in me, and I will always cherish their support.

I am also indebted to the staff of the Remote Sensing and Geographic Information Systems Department at Cukurova University, who shared their knowledge and expertise throughout my Masters studies and provided me with the necessary resources and equipment.

I also acknowledge the support and encouragement extended to me by my colleagues and research participants in various research groups and platforms across the globe, who also provided me with valuable feedback, advice and insights during various stages of my research. Their constructive suggestions helped me improve the quality of my work and contributed significantly to the success of this research.

In conclusion, I am deeply grateful to everyone who has contributed to the successful completion of this thesis. Your support, encouragement, and contributions have been valuable to achieve this personal milestone.

I also express my thanks to the readers and reviewers of this thesis for their time, effort, and valuable feedback. Their critical review and constructive criticism helped me improve the quality of my work and achieve the desired outcomes. I hope that my study will contribute to the existing body of knowledge in Remote Sensing and Geographic Information Systems and provide insights for policymakers, planners, and researchers working on the same or similar scope of research in Turkiye and across the globe.

LIST OF TABLES

Table 2. 1. Spectral features of Sentinel 2 bands (ESA) 13
Table 4.1 2018 and 2019 NDVI Mean Values..39
Table 4.2 2020, 2021 and 2022 NDVI Mean Values..40
Table 4.3 2018 and 2019 NDWI Mean Values..45
Table 4.4 2020, 2021 and 2022 NDWI Mean Values..46
Table 4.5 2018 and 2019 NDSI Mean Values 52
Table 4.6 2020, 2021 and 2022 NDSI Mean Values 53
Table 4.7 2018 and 2019 NDBI Mean Values..58
Table 4.8 2020, 2021 and 2022 NDBI Mean Values..59
Table 4.9 Consumer's Accuracy values for 2018, 2019, 2020, 2021 and 2022................................75
Table 4.10 Producer's Accuracy values for 2018, 2019, 2020, 2021 and 2022................................76
Table 4.11 Overall Accuracy and Kappa Statistics values for 2018, 2019, 2020, 2021 and 2022 ...77
Table 4.12 Areas values in square kilometers for 2018, 2019, 2020, 2021 and 2022........................78
Table 4.13 Subset Consumer's Accuracy values for 2018, 2019, 2020, 2021 and 2022 85
Table 4.14 Subset Producer's Accuracy values for 2018, 2019, 2020, 2021 and 2022 86
Table 4.15 Subset Overall Accuracy and Kappa Static values for 2018, 2019, 2020, 2021 and 2022..87
Table 4.16 Area values in square kilometers for 2018, 2019, 2020, 2021 and 2022 88
Table 4.17 Change in LULC (Study Area) Values 90
Table 4.18 Change in LULC (Subset) Values..90

LIST OF FIGURES

Figure 3.1 The Study Area 16
Figure 3.2 Workflow of the Study Area........ 19
Figure 3.3 Sentinel 2 Imagery Import 22
Figure 3.4 Pre-processing and Visualization........ 22
Figure 3.5 Cloud Cover Masking........ 23
Figure 3. 6 Merge Cloud Cover Image to Real Image 23
Figure 3.7 Spectral Indices Calculation 24
Figure 3.8 Time Series Chart and Histogram........ 25
Figure 3.9 Classification and Training Implementation........ 26
Figure 3.10 Classifier Training and Hyperparameters Tuning........ 27
Figure 3.11 Accuracy Assessment 30
Figure 4.1 NDVI Maps for 2018, 2019, 2020, 2021 and 2022 34
Figure 4.2 2018 NDVI Time Series 36
Figure 4.3 2019 NDVI Time Series 37
Figure 4.4 2020 NDVI Time Series 37
Figure 4.5 2021 NDVI Time Series 37
Figure 4.6 2022 NDVI Time Series 38
Figure 4.7 NDWI Maps for 2018, 2019, 2020, 2021 and 2022 41
Figure 4.8 2018 NDWI Time Series 43
Figure 4.9 2019 NDWI Time Series 43
Figure 4.10 2020 NDWI Time Series 43
Figure 4.11 2021 NDWI Time Series 44
Figure 4.12 2022 NDWI Time Series 44
Figure 4.13 NDSI Maps for 2018, 2019, 2020, 2021 and 2022........ 47
Figure 4.14 2018 NDSI Time Series........ 50
Figure 4.15 2019 NDSI Time Series........ 50
Figure 4.16 2020 NDSI Time Series........ 50
Figure 4.17 2021 NDSI Time Series........ 50
Figure 4.18 2022 NDSI Time Series........ 51
Figure 4.19 NDBI Maps for 2018, 2019, 2020, 2021 and 2022 54
Figure 4.20 2018 NDBI Time Series 56
Figure 4.21 2019 NDBI Time Series 57
Figure 4.22 2020 NDBI Time Series 57
Figure 4.23 2021 NDBI Time Series 57
Figure 4.24 2022 NDBI Time Series 57

Figure 4.25 Land Use and Land Cover (LULC) Map of Adana Province in 2018 61
Figure 4.26 Land Use and Land Cover (LULC) Map of Adana Province in 2019 62
Figure 4.27 Land Use and Land Cover (LULC) Map of Adana Province in 2020 63
Figure 4.28 Land Use and Land Cover (LULC) Map of Adana Province in 2021 64
Figure 4.29 Land Use and Land Cover (LULC) Map of Adana Province in 2022 65
Figure 4.30 Water (LULC) Maps of Adana Province 67
Figure 4. 31 Tree (LULC) Maps of Adana Province 68
Figure 4.32 Flooded Vegetation (LULC) Maps of Adana Province 69
Figure 4.33 Crops (LULC) Maps of Adana Province 70
Figure 4.34 Built Area (LULC) Maps of Adana Province 72
Figure 4.35 Bare Ground (LULC) Maps of Adana Province 73
Figure 4.36 Rangeland (LULC) Maps of Adana Province 74
Figure 4.37 Subset Map from Study Area 81
Figure 4.38 LULC Map (Subset) of Adana Province in 2018 82
Figure 4.39 LULC Map (Subset) of Adana Province in 2019 82
Figure 4.40 LULC Map (Subset) of Adana Province in 2020 83
Figure 4.41 LULC Map (Subset) of Adana Province in 2021 84
Figure 4.42 LULC Map (Subset) of Adana Province in 2022 85
Figure 4.43 Classified Map of Adana 93
Figure 4.44 Water Map of Adana (2018) 94
Figure 4.45 Water Map of Adana (2019) 94
Figure 4.46 Water Map of Adana (2020) 95
Figure 4.47 Water Map of Adana (2021) 95
Figure 4.48 Water Map of Adana (2022) 95
Figure 4.49 Built Area Map of Adana (2018) 96
Figure 4.50 Built Area Map of Adana (2019) 96
Figure 4.51 Built Area Map of Adana (2020) 96
Figure 4.52 Built Area Map of Adana (2021) 97
Figure 4.53 Built Area Map of Adana (2022) 97
Figure 4.54 Crops Map of Adana (2018) 97
Figure 4.55 Crops Map of Adana (2019) 98
Figure 4.56 Crops Map of Adana (2020) 98
Figure 4.57 Crops Map of Adana (2021) 98
Figure 4.58 Crops Map of Adana (2022) 99
Figure 4.59 Flooded Vegetation Map of Adana (2018) 99
Figure 4.60 Flooded Vegetation Map of Adana (2019) 99
Figure 4.61 Flooded Vegetation Map of Adana (2020) 100

Figure 4.62 Flooded Vegetation Map of Adana (2021) 100
Figure 4.63 Flooded Vegetation Map of Adana (2022) 100
Figure 4.64 Training Sample Map of Adana........ 103
Figure 4.65 Subset Training Sample Map of Adana 104

SYMBOLS AND ABBREVIATIONS

LULC: Land Use Land Cover
ML: Machine Learning
GEE: Google Earth Engine
ROI: Region of Interest
MSI: Multispectral Instrument
NDVI: Normalized Difference Vegetation Index
NDWI: Normalized Difference Water Index
NDSI: Normalized Difference Snow Index
NDBI: Normalized Difference Built-up Index
GIS: Geographical Information Systems
LiDAR: Light Detection and Ranging
DEMs: Digital Elevation Models
SVM: Support Vector Machine
ESA: European Space Agency
USGS: United States Geological Survey
NASA: National Aeronautics and Space Administration
MODIS: Moderate Resolution Imaging Spectroradiometer
AWS: Amazon Web Services
EODA: Earth Observation Data Analysis
FAO: Food and Agriculture Organization
LCCS: Land Cover Classification System
QA: Quality Assurance

1. INTRODUCTION

1.1. Background

Land Use and Land Cover (LULC) change is a very important study that has proven to be very vital in the modern society and evolution of human activities. The term LULC involves two distinct but interrelated aspects of the relationship between man and the environment. Land use can be easily stated as human activities related to the use of the environment such as Agriculture, Urbanization, Forestry, Mining etc. Whereas, Land cover is associated with the natural and physical aspect of the geography of the Earth such as water, forestry, rock, soil etc. (Das and Angadi, 2020)**.**

The rapidly change in environment and its usage has advanced and opened a path for various countries and researchers to develop ways of sustaining the environment and its habitants. The growing global changes in climate, biodiversity and economic and social development can be greatly attributed to ecosystem changes, civilization and modern technological methods (Yu et al., 2022). It is very crucial to understand the dynamics and changes of LULC to advice on the development of effective policies and strategies for sustainable land management and use.

It is estimated that around the year 2100 continuous changes in the LULC of the Earth's surface will have a much more ripple effect on the environment compared to the damage climate change is bringing about (Chapin et al., 2000). Rapid degradation of the land has been meanly influenced by human activities and lack of strict policies to conserve natural habitats and organized usage of natural resources. Human altered drivers such as Urbanization and Industrialization have greatly impacted LULC. According to Grimm et al. (2008), the year 2010 saw a huge rise in the number of people and activities living in urban areas compared to rural areas. This can be attributed to the rapid urbanization and migration of individuals. Rising challenges such as Food security, ecological problems and climate change are a worrying international concern.

Countries with a huge population such as China have faced huge problems in managing their habitat and environment due to rapid population growth and urban related human activities (He et al., 2014). Urban areas globally are expected to expand to over 1.2 million km^2 by the year 2030 with over 5 billion people occupying urban areas (Seto et al., 2012). In addition, the transformation of most countries from an agriculture economy to a more industry based with technological methods in Agriculture has also impacted LULC changes (del Mar López et al., 2001).

Densely populated continents such as Europe have suffered rapid urbanization and stated that roughly 80% of its population live in industrialized urban areas. The most affected areas are Agriculture lands which have seen a reduction due to modern advancements and new ways of food production (Antrop, 2004). However, as Skog and Steinnes, (2016) stated Agricultural land loss is not only a challenge in developed settlements with a high density of population but also a major challenge in low density settlements as most of the land is transformed into urban settlements.

To address and analyze the changes in LULC across the globe, technological ways and studies have been developed. The development of studies such as Remote Sensing (RS) and Geographical Information Systems (GIS) have broadly enabled humans to develop systems and methods of periodically gather information related to changes in LULC. Most of the technological instruments developed have been designed to gather, analyze and record changes in databases installed on both the Earth and Space. It is with such that these studies are now widely used in fields such as Mining, Meteorology, Agriculture, Oceanography and Land development.

The use of satellite data presents a valuable opportunity to examine and explore the changes in LULC over time, enabling more informed decision-making. In recent times, there have been a growing trend in utilizing satellite data to analyze LULC transformation due to its capability to provide precise and comprehensive information across vast areas, which is crucial for evaluating urbanization patterns (Alam et al., 2020).

Moreover, the use of satellite data is becoming increasingly popular due to its advantages over traditional data collection methods. It is less time-consuming, less expensive, and can provide more precise and up-to-date information on LULC transformation, which is essential for studying urbanization processes. This makes it easier for researchers and makers of decisions to understand the dynamics of LULC transformation and its implications for sustainable development.

Furthermore, Roy and Roy, (2010) stated satellite data has the advantage of providing a comprehensive and objective view of LULC transformation. It can capture changes in LULC at various spatial and temporal scales, making it possible to analyze patterns and trends over long periods. This can aid in identifying areas with more intense land use changes or areas where certain land uses are expanding or declining rapidly. Gained data can also be used to evaluate the impact of land use changes on the environment, such as changes in vegetation cover, soil erosion, and water quality.

Another advantage of satellite data is its usefulness in monitoring LULC changes in remote or inaccessible areas. For example, it can be challenging to gather information on land use changes in mountainous or forested regions or areas that are prone to natural disasters (Faruque et al., 2022). Satellite data can overcome these limitations by providing a bird's eye view of these areas, enabling researchers to monitor changes in LULC remotely.

Moreover, the use of satellite information can support the development of early warning systems for environmental disasters. For example, it can help to detect changes in land use and land cover that are likely to lead to floods, landslides, or other natural disasters. The obtained information can be used to inform emergency response efforts and mitigate the impact of these events.

1.2. Literature Study

This Literature study reviews and highlights the significance of satellite data and remote sensing techniques and studies related to LULC changes across the globe and Turkiye. The main types of satellite data are introduced and widely used classification methods are also discussed.

Satellite data is considered the main raw material in LULC changes and classification. It involves the process of categorizing, mapping, analyzing and obtaining imagery using different Remote Sensing techniques.

1.2.1. Satellite Data

The most crucial preliminary necessity in Remote Sensing studies can be considered as Satellite data, which refer to the digital information and imagery collected by satellites orbiting the Earth. As of 2023, 7702 active satellites are orbiting in space and also include Low Earth Orbit satellites. These modern age equipment are specifically installed with various sensors and instruments used to collect information by detecting and recording electromagnetic radiation across different wavelengths (Yang et al., 2013). The data collected is very essential in providing valuable insights into various aspects of the surface of the Earth, atmosphere, oceans and deep space.

Availability and accessibility of satellite data has increased significantly in recent years, with various space agencies and commercial providers offering access to satellite imagery and data archives. Additionally, advancements in data processing, storage, and analysis techniques, including machine learning and artificial intelligence, have enhanced the utilization and extraction of meaningful information from satellite data.

Satellite data serves as a powerful tool for understanding global and regional phenomena, monitoring environmental changes, and informing evidence-based decision-making. Its applications continue to expand as technology advances, providing valuable insights into our planet's dynamic processes and helping address critical environmental and societal challenges (Genzano et al., 2020).

There are different types of satellite data depending on the sensors, instruments and purpose used. Some of the commonly utilized types include:

1. **Optical Data:** These are satellites designed for optical observation and gather information from the visible, near infrared and shortwave infrared segments of the electromagnetic spectrum. These satellites provide images with various spatial resolutions, allowing for the identification and mapping of land cover types, vegetation health, coastal and marine features, and atmospheric conditions.
2. **Radar Data:** Radar satellites employ synthetic aperture radar (SAR) technology to transmit microwave signals towards the surface of the Earth and measure the backscattered signals. Radar data can penetrate clouds, enabling all-weather imaging

and providing information on topography, surface roughness, vegetation structure, and soil moisture.

3. **Thermal Data**: Satellites equipped with thermal sensors capture data using thermal radiation emitted by the surface of the Earth. This data helps monitor land surface temperature, detect urban heat islands, analyze energy fluxes, and assess the health and stress levels of vegetation.
4. **Hyperspectral Data:** Hyperspectral satellites gather data in hundreds of narrow and plenty spectral bands, enabling a user to have access to a detailed spectral analysis. This data is valuable for identifying and characterizing specific materials, minerals, vegetation types, and environmental conditions.

Satellite data serves as a powerful tool for understanding global and regional phenomena, monitoring environmental changes, and informing evidence-based decision-making. Its applications continue to expand as technology advances, providing valuable insights into our planet's dynamic processes and helping address critical environmental and societal challenges.

1.2.2. Remote Sensing Techniques

Various widely used Remote sensing techniques play a fundamental role in analyzing LULC dynamics using satellite data. These techniques involve the collection and interpretation of information about the Earth's surface from a distance. They provide valuable insights into the spatial and spectral characteristics of land cover classes, allowing researchers to monitor and analyze LULC changes over time. Here are some commonly used remote sensing techniques in LULC analysis:

1. **Multispectral Remote Sensing:** Multispectral remote sensing involves capturing and analyzing electromagnetic radiation from the surface of the Earth in multiple spectral bands. This technique analyzes the electromagnetic radiation that the Earth’s surface reflects or emits in various spectral bands by capturing it (Jensen, 1996). By capturing and analyzing the electromagnetic radiation in different spectral bands from the Earth’s surface, this technique identifies land cover types (Mather and Koch, 2011). The electromagnetic radiation from the surface of the Earth in multiple spectral bands is captured and analyzed by this technique (Lillesand et al., 2015).
2. **Hyperspectral Remote Sensing**: It provides a more detailed and fine-grained analysis of land cover classes by capturing data in numerous narrow and contiguous spectral bands. The technique captures data in many narrow and adjacent spectral bands to provide a finer and more detailed analysis of land cover classes (Thenkabail et al.,

2014). By capturing data in a large number of narrow and continuous spectral bands, this technique enables a more detailed and fine-grained analysis of land cover classes (Goetz et al., 1985). A finer and more detailed analysis of land cover classes is provided by this technique, which captures data in numerous narrow and contiguous spectral bands.

3. **Synthetic Aperture Radar (SAR):** SAR utilizes microwave signals to measure the backscattered energy from the surface of the Earth. It can penetrate clouds and collect data regardless of weather conditions, making it particularly useful for mapping land cover in areas with persistent cloud cover. SAR data provides information about surface roughness, soil moisture, and vegetation structure, which are valuable for LULC analysis. It measures the energy that is backscattered from the surface of the Earth by using microwave signals (Lee et al., 1999). The backscattered energy from the Earth's surface is measured by this technique using microwave signals (Ulaby et al., 1986).
4. **LiDAR (Light Detection and Ranging):** LiDAR is a modern technique that measures the distance between the sensor and the surface of the Earth by emitting laser pulses and recording their reflections. LiDAR data provides highly accurate information on topography, terrain elevation, and 3D structures. It is useful for creating detailed digital elevation models (DEMs), generating high-resolution terrain models, and identifying vegetation height and structure. This technique emits laser pulses and records their reflections to measure the distance between the sensor and the Earth's surface (Lim et al., 2003; Wehr and Lohr, 1999).
5. **Thermal Remote Sensing:** Thermal remote sensing measures the emitted thermal radiation from the surface of the Earth. It is particularly useful for studying urban heat islands, monitoring energy fluxes, and assessing vegetation stress. By analyzing thermal data, researchers can identify variations in land cover based on their thermal properties. This technique measures the thermal radiation that is emitted from the surface of the Earth (Weng et al., 2004). By measuring the thermal radiation, this technique captures the emission from the Earth's surface (Sobrino and Paolini, 2004). The emission from the surface of the Earth is measured by this technique using thermal radiation (Dash et al., 2002).

1.3. Aim and Research Objectives

The main aim of this study is to analyze and investigate the LULC changes in Adana, Turkey over a 5-year period of time from 2018 to 2022 using Sentinel-2 satellite data, Google Earth Engine and essential GIS tools such as ArcGIS Pro. As the study area itself encompasses less studies and research pertaining to LULC, it is important and valid for students and researchers to contribute and analyze the rich geographical features and landscape of the area. Adana's geographical diversity, agricultural significance, vulnerability to various environmental factors make it a very ideal location for remote sensing research and applications. Moreover, as the area is the hub for Turkey's agriculture and booming infrastructure it is right for scientific researchers to provide up to date remote sensing information which is very essential in addressing issues in Agriculture, Flood and Water Management, Natural Resource Management, Urban and Regional Planning, Disaster Response and Recovery and more importantly Environment Education. By fully harnessing and utilizing the power of Remote Sensing technologies and GIS tools, vulnerabilities to various environmental factors and local challenges can be easily addressed and precautions implemented. In addition, as most remote sensing studies are conducted over long periods of year, such as from 2010 to 2020, rather than on a yearly basis, for 5-year period is crucial to address and correctly understand the annual and cumulative changes in the Earth environment over the study area. Data collected can be crucial for similar future research studies, policy and decision making, creation of databases that can show short term trends or long-term correlation in LULC over periods of time for up-to-date statistical significance and data availability.

To achieve maximum and accurate results, the combination of Multispectral Remote Sensing and Machine Learning will be a key focus in the sense that Multispectral Remote Sensing involves using sensors that capture bands such as visible, near infrared and additional bands necessarily for in-depth analyses of LULC. Additionally, most of the multispectral data is freely available on satellites with high resolution such as Sentinel-2 making it easy to obtain good quality imagery and band combinations. However, as Machine Learning models automatically extract relevant features and spectral information, especially through cloud platforms such as Google Earth Engine, the data complexity and processing are greatly reduced compared to the old traditional methods of LULC studies. The application of sophisticated algorithms to multispectral imagery greatly enhances the accuracy and classification of the results leading to more precise and reliable data which will be essential for this study.

As the study literature states, it is essential to analyze and study LULC changes to give insights and information on the changes on the surface of the Earth. The results obtained in this study will help to raise awareness, act as a reference for similar studies and offer suggestions on how land can be used. The main objectives and steps to fulfill the study's aim are;

- Obtain high resolution multispectral satellite imagery with less cloud cover.
- Implement a Random Forest Machine Learning Algorithm in GEE for analysis and classification.
- Map Spectral Indices such as NDVI, NDWI, NDBI and NDSI
- Map the LULC of the study area for years 2018 to 2022.
- Analyze the LULC changes over the time period.
- Highlight the strengths and weakness of using Machine Learning Algorithms in cloud-based environments for classification and mapping LULC change.

2. PRELIMINARY WORK

2.1. General Studies Related with Remote Sensing

Studies in Remote Sensing encompass a variety and wide range of research areas and applications. Generally, the choice of focus depends on the needed information and objectives. The fundamental task of categorizing the surface of the Earth is very curial in monitoring the changes in LULC overtime and involves the development and evaluation of classification algorithms, spectral, spatial, temporal information and accuracy assessment techniques. General studies conducted in Remote Sensing include, Agricultural Monitoring, Wetland studies, Natural Hazard Assessment, Ecological studies, Land use and Land cover classification, Climate Change Impact and Urbanization and Settlement Planning. Notable works and scientific finding have been conducted by various authors globally to address norms and uses of Remote Sensing to the field and study on Urbanization and Environmental Monitoring (Qian et al., 2020). Similarly, to address the significant implications of human activities on the environment, Dr. Martin Herold's research has provided valuable contributions and addressed global environmental challenges and land cover (Herold et al., 2008). Thenkabail et al. (2014) a leading expert in Agricultural Remote Sensing has also published extensively on topics such as Crop Mapping, Crop Yield Estimation and Precision Agriculture using satellite imagery. Achard and Hansen (2012) has also made tremendous progress in forest monitoring through his notable projects such as the Global Forest Change which provides a wealth of data, maps and tools for monitoring global land cover changes, including deforestation and agricultural expansion. Additionally, to address Wetland and Waterbody monitoring, Dr. Rich conducted extensive research on wetland mapping and mapping to access health, dynamics and ecological changes using satellite imagery (Rich, 2012) while Dr Phinn's research is instrumental in advancing the ability to monitor and protect coastal and wetland ecosystems critical for biodiversity, carbon storage and coastal resilience (Phinn et al., 2012).

As this study entirely focuses on LULC, various key players in the field have also made tremendous research and scientific projects to ascertain results both globally and locally in relation to the study area. Global studies include Land use change in the Amazon rain forest, their drives, including deforestation and agricultural expansion. The Sahel region of Africa has also seen LULC studies with a focus on analyzing the implications of climate change and land activities (Diouf and Lambin, 2001). Munthali et al., (2019) analyzed LULC change dynamic by using both supervised and unsupervised classification algorithms for multi temporal analysis in Dedza district, Malawi. Additionally, areas like the Greater Beirut Area, Lebanon have also seen the use of Remote Sensing techniques to detect changes in LULC with a key focus in Urbanization (Masri et al., 2002). A study was also conducted to assess the Urban Growth and Sprawl in the Red River Delta of Hanoui in Vietnam (Mauro, 2020) by renowned experts to give an understanding in the rapid change of population in the region. Wang et al. (2020) also conducted a study in the Qinghai-Tibet

Plateau, to provide an insight into the environment. Remote Sensing and Digital Image Processing book by Jensen (1996) provides remote sensing principles and digital image processing techniques while covering topics such as image interpretation, classification and the combining of remote sensing data with GIS. The book is considered an essential resource for students, researchers and professionals in the field. Lambin and Geist (2006) also produced an influential book that delves into the relationship between land use and land cover change processes and their broader consequences. It greatly underlines the significances of Remote Sensing and GIS in monitoring and understanding the changes and socio-environmental impacts of LULC changes, making it a vital resource for research and policy makers.

2.2. LULC Studies Related to the Local Area

The local area associated with the study area is not exempt to LULC studies and various key researchers have made tremendous tides and effort to contribute to the Global Scientific Knowledge and Information related to usage of Remote Sensing and GIS technology. Akyürek et al. (2018) used two different sets of satellite images, Sentinel 2A and Landsat-8, along with supervised classification and several spectral indices, to study the changes that happened during the building of the new airport in Istanbul. Yılmaz (2010) used the CORINE program to classify the land cover of the coastal town of Silivri, which is part of greater Istanbul. . Göksel and Balçık (2019) used enhanced SPOT 5 MS satellite images and a maximum likelihood supervised classification technique to study the growth of the urban area in the Akdeniz district of Mersin, Turkey. Karakuş (2019) used maps from the Landsat satellite image to show the best land use and development of residential areas in the city of Sivas in Turkey. Ikiel et al., (2013) used an integrated approach that involved analyzing satellite images using random forest classification of Landsat Time series. Ettehadi Osgouei et al. (2019) also used a multi index-based Support Vector Machine (SVM) classification to study the complex and morphologically diverse LULC patterns of Istanbul city. Spruce et al., (2020) discussed using existing LULC maps to study changes with 9 classes per date using GIS overlay techniques. Zadbagher et al. (2018) used Cellular Automata and Markov Chain (CA-MC) models to predict the LULC changes in the Seyhan Basin in Turkey that are likely to happen by 2036. The LULC prediction for the year 2036 showed a 50% increase in the built-up area class and a 7% decrease in the open spaces class compared to the LULC status of the reference year 2016. Furthermore, Alphan and Yilmaz (2005) also used a remote sensing approach to study the changes in land use/cover (LULC) over time in Cukurova, a large coastal plain on the Southeast Mediterranean coast of Turkey. They studied the most noticeable changes which had happened in agriculture, urban, and natural vegetation cover. To evaluate and improve urban green spaces for compact urban areas in the Cukurova district in Adana, Turkey, Unal and Uslu (2018) used a weighted criteria method to determine the quality and the quantity of active green spaces. Additionally, Iban and Sahin (2022) tried to use Landsat 8 image composites to study LULC changes on construction sites and the Akkuyu Nuclear Power Plant project in the Southern part of Turkey.

2.3. Global Land Cover Maps

The modern age has seen vast advancements in LULC studies as such the need to obtain comprehensive information and accurate data for the distribution and characteristics of land cover and a global scale has risen. Large organized institutions in GIS have developed various technologies and ways of acquiring these changes.

One of the datasets developed are Global Land Cover Maps. These maps have been thoroughly developed over periods of time after intense training and collection of data. Steps involved in designing such huge global maps include obtaining satellite imagery from multiple sensors, pre-processing, image classification, validation and rapid accuracy assessments.

These Global Land Cover Maps are essential in providing information such as monitoring LULC changes over periods of time, modelling climate change and managing resources. Overall, they are used to understand and monitor the changes that are known to affect the environment and create actions to mitigate and adapt to global change (Mora et al., 2014). The widely used maps are as follows;

1. **The Copernicus Global Land Service:** The Copernicus Global Land Service: PROBA-V data are used to create annual land cover maps at 100m for the period 2015-2019 using the United Nations Food and Agriculture Organization's (FAO) Land Cover Classification System (LCCS) and include vegetation continuous field layers with proportional estimates of vegetation cover types.
2. **The ESA Global Cover:** It delivers a global land cover map at 300m resolution for the year 2005-2006 derived from Envisat's MERIS data and based on the FAO LCCS with validation by domain-specific experts from more than 3 000 reference points. This is the most detailed land cover dataset that was ever completely cross-validated.
3. **The Esri 2017/2022 Global Land Cover Map**: The Esri 2017/2022 Global Land Cover Map is a product that provides a consistent map of land cover for the entire world at 10m resolution from the year 2017 to 2022, based on Sentinel-2 data. The map uses a machine learning algorithm to classify the data into 9 land cover classes and has been verified by experts using more than 25 000 reference points. This land cover map is the most recent and detailed coverage available for the entire globe.
4. **MODIS Land Cover (MCD12Q1):** The Moderate Resolution Imaging Spectroradiometer (MODIS) provides global land cover data at a moderate resolution (approximately 500 meters). The MODIS Land Cover Type product (MCD12Q1) categorizes land cover into several classes, including forests, croplands, grasslands,

wetlands, urban areas, and more. It is widely used for global environmental assessments.

5. **Glob Cover:** It is made from a project intended to produce a global land cover map at a 300-meter resolution using data from the ENVISAT satellite. It classifies land cover into over 20 categories and is used for climate modeling, environmental monitoring, and more.
6. **EarthEnv Land Cover:** The EarthEnv Land Cover project offers global land cover maps at various spatial resolutions, including 30 meters, 250 meters, and 1 kilometer. These datasets are designed to support ecological and environmental research.
7. **Dynamic World V1:** It has a 10m near real-time LULC point prediction dataset with class-probabilities and labels for nine classes. Dynamic World predictions are available for the Sentinel-2 L1C collection from 2015-06-27 to present. Because of its revisit time of 2 to 5 days depending on its latitude, Sentinel-2 has extremely high-spatiotemporal coverage. Dynamic World predictions are derived for Sentinel-2 L1C that have Cloudy Pixel Percentage of less or equal to 35%. To remove clouds and cloud shadows, predictions are sampled using a combination of S2 Cloud Probability, Cloud Displacement Index, and a Directional Distance Transform.
8. **Global map of Local Climate Zones:** It has a pixel size of 100m and representative for the nominal year 2018, which is derived from multiple earth observation datasets and local climate zone class labels. As it is a known local climate zone filter, it is the recommended band for most users and includes its other classification bands which are only provided to calculate the local climate zone probability band and other important information.
9. **Copernicus CORINE Land Cover:** It was initiated in 1985 to help with data collection on land in Europe mainly to support environmental policy developments. The project was started by the European Environment Agency in the frame of the EU Copernicus program and implemented by most nations. The number of participating countries has increased over time currently including 33 member countries and six cooperating countries.

2.4. Remote Sensing Satellites and Software

2.4.1. Remote Sensing Satellites

Remote Sensing Satellite and software are designed and integrated to work together. Satellites are considered the base and first step in obtaining information and data through sensors across different wavelengths of the electromagnetic spectrum, while software tools considered the second step as their role is to process, extract, interpret and present results from the acquired data from satellites. There are various satellites across the Globe which include both commercial and non-commercial satellites. The commonly used open source satellites that provide easy to access data are Sentinel, Landsat and MODIS and can be described as follows;

1. **Sentinel:** The European Space Agency (ESA) through the Copernicus Program provide the Sentinel satellites which offer high resolution multispectral imagery. The imagery and data is free and provided through an open source hub. The program consists of various Sentinel satellites designed for specific purposes. For example, the Sentinel-1 consists of twin polar orbital satellites designed to provide spatial information from SAR images necessary for acquiring data for the environment, security, global economics and business-related issues. In addition, they have also developed twin satellites called the Sentinel-2A and Sentinel-2B designed to collect high resolution multispectral imagery necessary to monitor LULC changes, forests, agriculture and flooding issues. More satellites such as Sentinel 4, 5 and 6 are also payloads designed for specific purposes related to monitoring and measuring atmosphere conditions and global sea heights.
2. **Landsat:** Unlike the European Sentinel satellites Landsat satellites are U.S satellites designed to offer similar information and data. They have been in existence since 1970 and are operated by the United States Geological Survey (USGS) and The National Aeronautics and Space Administration (NASA). Their capabilities involve capturing both multispectral and thermal data essential to maintaining LULC changes, climate change, drought and floods, wildfires and biomass changes.
3. **MODIS:** The MODIS is also a key instrument consisting of 36 spectral channels and installed in NASA Earth Observing System satellites called the Terra and Aqua. It is designed to offer a global coverage every 1 to 2 days and widely used in studies related to vegetation monitoring, LULC change and Oceanology.

2.4.2. Remote Sensing Software

Remote sensing software consists of cloud-based software and manual-based software. They both use different approaches and can be both single handily used or integrated to use both approaches for a required analysis or study. Cloud-based remote sensing software offer software applications or platforms that can be easily accessed and operated through the internet on remote servers. These platforms provide remote sensing tools and capabilities, enabling users to upload, process, analyze, and visualize remote sensing data without the need for extensive local computing resources. Cloud-based solutions offer the advantage of scalability, as they can handle large number of datasets and complex processing tasks efficiently. They also facilitate collaboration and data sharing among users located in different locations. Some examples of cloud based remote sensing software include Google Earth Engine (GEE), Amazon Web Services (AWS) Earth

Observation Data Analysis (EODA) platform, and Microsoft Azure AI for Earth. In comparison, Manual-based approaches include traditional methods of analyzing remote sensing data using desktop software tools installed on local computers. These tools often require users to have a certain level of expertise in remote sensing techniques and image processing. Users manually perform various steps in the analysis workflow, such as data preprocessing, image interpretation, classification, and analysis. Desktop software applications like ArcGIS, QGIS, SNAP, ENVI, ERDAS, GLOBAL MAPPER, GEODA and GRASS GIS are some of the commonly used for manual-based remote sensing analysis. These tools provide a wide range of functionalities and allow users to have greater control over the analysis process, but they may require more computational resources and time compared to cloud-based solutions.

However, Cloud-based solutions offer convenience, scalability, and accessibility, particularly for large-scale projects or collaborations while Manual-based approaches provide more control and flexibility but require resources and specialized knowledge in remote sensing analysis. The choice between cloud-based remote sensing software and manual-based approaches depends on various factors, including project requirements, available resources, data size, computational capabilities, and the level of control and expertise needed in the analysis workflow.

2.4.3. Sentinel 2 Remote Sensing Data Capabilities

The Sentinel 2 satellite offers different levels of spatial resolution depending on the sensor and mission. They are designed to provide imagery at a spatial resolution of 10m, 20m and 60m according to the band characteristics. The band characteristics are captured in its special Multispectral Instrument (MSI) installed on both twin Sentinel 2A and Sentinel 2B satellites.

Sentinel 2A and Sentinel 2B offer similar capabilities and their main reasons for deployment was to increase data acquisition, improve coverage and data redundancy by improving the overall effectiveness of the Sentinel 2 mission in monitoring the Earth and its coastal areas. The table below illustrates the Sentinel 2 mission characteristics, wavelength and bandwidth.

However, to further enhance the results of the study the Sentinel-2 MSI: Multispectral instrument, Level 2A data was selected. The Level 2A dataset was made available in 2017 and contains unique features essential for the study such as providing 13 spectral bands ranging from visible to shortwave infrared. Level 2A also provide atmospherically corrected imagery which accounts for the effects of air molecules, gases and aerosols on the reflected radiation thereby increasing the accuracy and comparability of results. In addition, they also contain a scene classification map essential for identifying clouds, cloud shadows, snow, vegetation, water and related cover types hence reducing noise in imagery and facilitating the masking process and filtering of unwanted pixels. The Level 2A is also compatible with Landsat surface reflectance products with similar resolution and spectral range hence enabling the easy usable of both datasets for analysis. Table 2.1 below closely analyzes the differences in spectral features between the Sentinel 2A and Sentinel 2B.

Table 2. 1. Spectral features of Sentinel 2 bands (ESA)

	S2A		**S2B**		
Band	**Ce**	**Ba**	**Centr**	**Ba**	**Re**
B01-Coastal	442	21	442.3	21	60
B02-Blue	492	66	492.1	66	10
B03-Green	559	36	559.0	36	10
B04-Red	664	31	665.0	31	10
B05-Red edge	704	15	703.8	16	20
B06-Red edge	740	15	739.1	15	20
B07-Red edge	782	20	779.7	20	20
B08-NIR 1	832	106	833.0	106	10
B8A-NIR 2	864	21	864.0	22	20
B09-Water	945	20	943.2	21	60
B10	137	31	1376.	30	60
B11-SWIR 1	161	91	1610.	94	20
B12 -SWIR 2	220	175	2185.	185	20

3. MATERIAL AND METHOD

3.1. Material

The study involved usage of high-resolution multispectral imagery through Sentinel-2, Google Earth Engine and ArcGIS Pro. Multispectral Imagery is the core basis of an accurate LULC classification as it provides various essential properties such as multiple wavelength bands, distinct spectral signatures, reduced atmospheric effects, availability of data at regular intervals on open-source platforms and ability for integration with other GIS tools to maximize enhancement. Sentinel-2 imagery was selected as the Multispectral Imagery provider because of its unique features and characteristics as discussed in the previous chapter. As evidently observed most GIS tools and software are designed to work together to provide the best results. However, to easily access the database of all multispectral imagery, cloud-based platforms were preferred to the traditional way of obtaining and downloading raw imagery from the Open-Source hubs such as Copernicus Open Access Hub which provides all Sentinel-2 data because of the time consuming and huge amount of data storage required to process the raw imagery.

Cloud-based platforms offer numerous advantages for handling multispectral imagery, primarily due to their scalability, remote accessibility and robust computational capabilities. Additionally, these platforms excel in data management, providing efficient storage, cataloging, versioning solutions, ensuring data integrity and availability. Most modern cloud-based platforms offer the ability for parallel processing and features such image analysis, preprocessing of data, performing machine learning tasks and integration capabilities with various data source, couple with easy-to-use methods make cloud processing an attractive choice to access Multispectral Imagery.

The study involved the usage of Google Earth Engine (GEE) a cloud based platform more accustomed with LULC studies. GEE boasts access to expensive archive of geospatial and remote sensing data such as Sentinel-2, Landsat, MODIS and various global land cover maps. Its cloud infrastructure excels in processing and analyzing vast geospatial datasets at scale, accommodating the demands of LULC studies often spanning extensive geographic regions. It’s suite of clouds-native geospatial tools simplifies image manipulation and pre-processing, streamlining workflows. Additionally, GEE supports machine learning algorithms for classification tasks which is very essential for this study. Its user-friendly interface and ability to export analyzed and classified results to other GIS tools such as ArcGIS Pro for more advanced visualization and presentation through formats such as GeoTIFF also make it a great choice.

ArcGIS Pro a versatile GIS software with capabilities such as extensive spatial analysis, scenario modelling, report generation, data sharing, map and data visualization in 3D and more importantly custom cartography which is essential in creating visually appealing maps, layouts, advanced symbology, map temples, incorporate legend and scale bars to final results was selected as the tool for the methodology related to the study. The software combines the analytical power of GEE with its customization options and visualization process necessary for refining, validating and effectively communicating all LULC study outcomes.

All the three platforms as described systematically were integrated in the methodology and workflow to acquire the best and accurate results relates to the study area.

3.1.1. Study Area

Adana, Turkey typically utilizes the Universal Transverse Mercator (UTM) projection system with its specific UTM zone falling with zone 36 or zone 37 due to its Southern location. The UTM as known divides the Earth into 60 zones numbered from 1 to 60, starting at approximately 180-degree longitude west of the International Date Line considered zone 1 and continuing eastward to approximately 180-degree longitude east of the International Date Line (zone 60). Each UTM zone covers a longitudinal span of 6 degrees. Additionally, the main purpose of these zones is to minimize the distortion in mapping and allows more accurate representation of geographic features within each specific region and each zone has its own coordinate system to facilitate precise positioning and measurement.

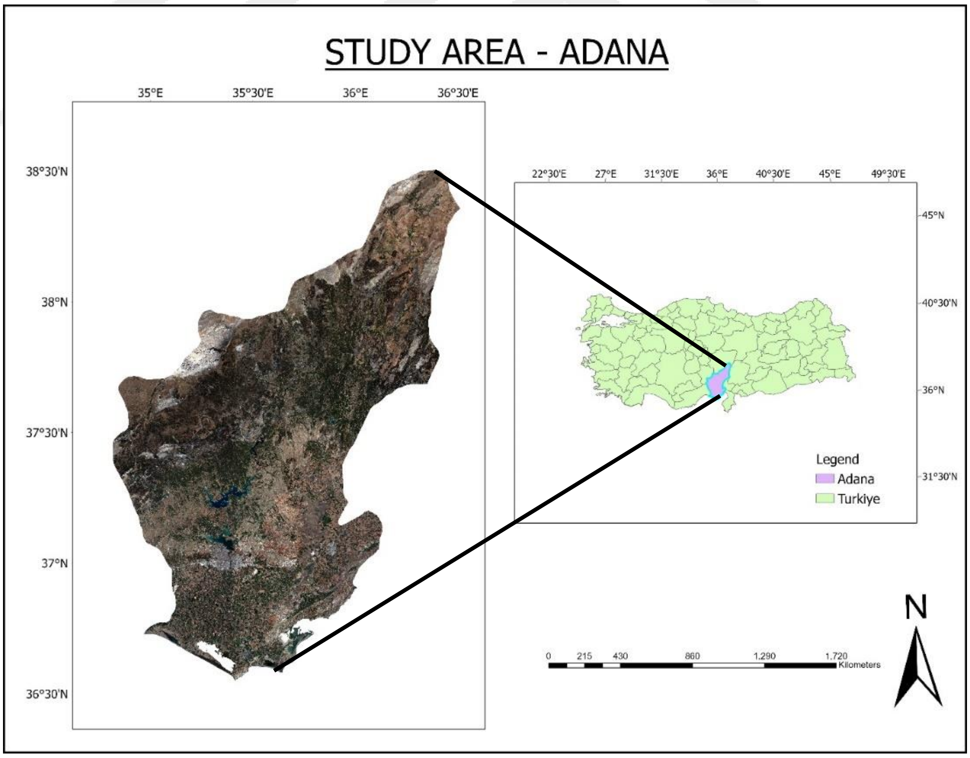

Figure 3.1 The Study Area

Historically, like much of Turkey, Adana employs the European Datum 1950 (ED50) as the reference framework for geospatial data and mapping. However, with the evolvement of datum’s many regions, including Turkey have transitioned to the World Geodetic System 1984

(WGS84) to align with GPS and international mapping standards, making it crucial to confirm the specific datum used in a particular project. Coordinates in the UTM system are expressed in meters as Easting (Y) and Northing (X) from a designated origin point within each UTM zone, with the N indicating the Northern hemisphere. For instance, in the UTM zone 36N of Adana. Coordinates are measured in meters Eastward from the Central Meridian of that zone and meters Northward from the Equator within the Northern hemisphere, facilitating accurate geospatial analysis and mapping applications. The study area (Figure 3.1) represents Adana which, lies at a latitude of approximately 37.000 degrees North and a longitude of about 35.3213 degrees East. The coordinates place it within the Cilicia region, a historical and geographical area in South Eastern Turkey.

3.1.2. General Description of the Study Area

Adana is a dynamic and culturally rich city located in Southern part of Turkey. This city, with its historical significance and modern developments, offers a unique blend of history, culture, geographic and economic vitality. Its geographical location is characterized by its proximity to the Mediterranean coast, approximately 30 kilometers inland from the sea. The city is situated at approximately 37.0000 degrees North latitude and 35.3213 degrees East longitude. The proximity to the Mediterranean has a profound influence on the city's climate and economy. The temperate Mediterranean climate brings hot, dry summers and mild, wet winters, creating an ideal environment for agriculture and other geographical related activities. Additionally, the presence of the Seyhan River, which flows through the heart of Adana plays a crucial role in the city's geography. This river serves as a source of water for irrigation, supporting the area's agriculture. It also adds to the city's aesthetics, with riverside promenades and parks providing scenic spots for relaxation and leisure activities. The city also has Taurus Mountains to the North which serve as a stunning backdrop to the city and source of natural beauty and geographic studies. The Taurus Mountains are known for their rugged terrain, deep valleys, mountaineering, and exploring pristine wilderness. They also contribute to the region's water resources, by feeding the Seyhan River and its tributaries. The plains surrounding Adana, primarily formed by the deposits of the Seyhan River, are among the most fertile in Turkey and have really played a major role in pivoting it as one of the main contributors of agriculture in the country. Moreover, the diverse geography of the region contributes to its biodiversity which is protected. The plains and mountains, surrounding the landscape include wetlands, forests and unique ecosystems. For example, special places such as the Akyatan and Tuzla lagoons which habit unique animal species are designated as protected areas because of the importance they have for the environment and the ecosystem.

The city's strategic location at the crossroads of major transportation routes has made it a key economic center in Turkey. Its city's economy is diverse and its modern infrastructure, including an extensive network of highways, a well-connected airport and a bustling port on the

Mediterranean coast all contribute to its important economic significance in the region. In addition, the city's history is a tapestry woven with influences from numerous civilizations that have inhabited the region over millennia. Notable historical sites include the Grand Mosque locally called the Ulu Cami, an impressive example of Turkish-Islamic architecture, and the Ramazanoğlu Hall also called the Ramazanoğlu Medrese, an exquisite piece of medieval architecture. The city's rich past is also reflected in its archaeological sites and ancient city ruins.

According to the World Population Review 2023, Adana has a population of approximately 1.8 million people making it one of Turkey's most populous and fast-growing cities. It thrives on its industries, attractive investment opportunities, lucrative rich geography and abundance of water bodies and a favorable agriculture climate.

The cultural diversity is evident in its population, comprising Turks, Armenians, Arabs and other ethnic groups, each contributing to the city's unique identity. The fusion of traditions and customs is celebrated during events, where the performing arts take center stage, enriching the city's cultural fabric. Adana's bazaars, also, pulsate with life, offering a glimpse into local customs, crafts, and flavors. Its allure lies in its multifaceted nature, seamlessly blending tradition with progress, offering a tapestry of experiences that captivate the senses and leave an indelible impression on all who explore its vibrant streets and immerse themselves in its rich heritage.

3.2. Method

This chapter provides an overview of the research methodology, placing a strong emphasis on the study's aim and objectives. Each step of the methodology is thoroughly described and explained, offering a clear understanding of the entire process. The chapter also includes the complete JavaScript code script implemented for Machine Learning in the GEE code editor, enabling a practical application of the methodology. Furthermore, to enhance comprehension of the methodology, a detailed workflow is outlined in Figure 3.2, ensuring a logical sequence of tasks and facilitating seamless execution.

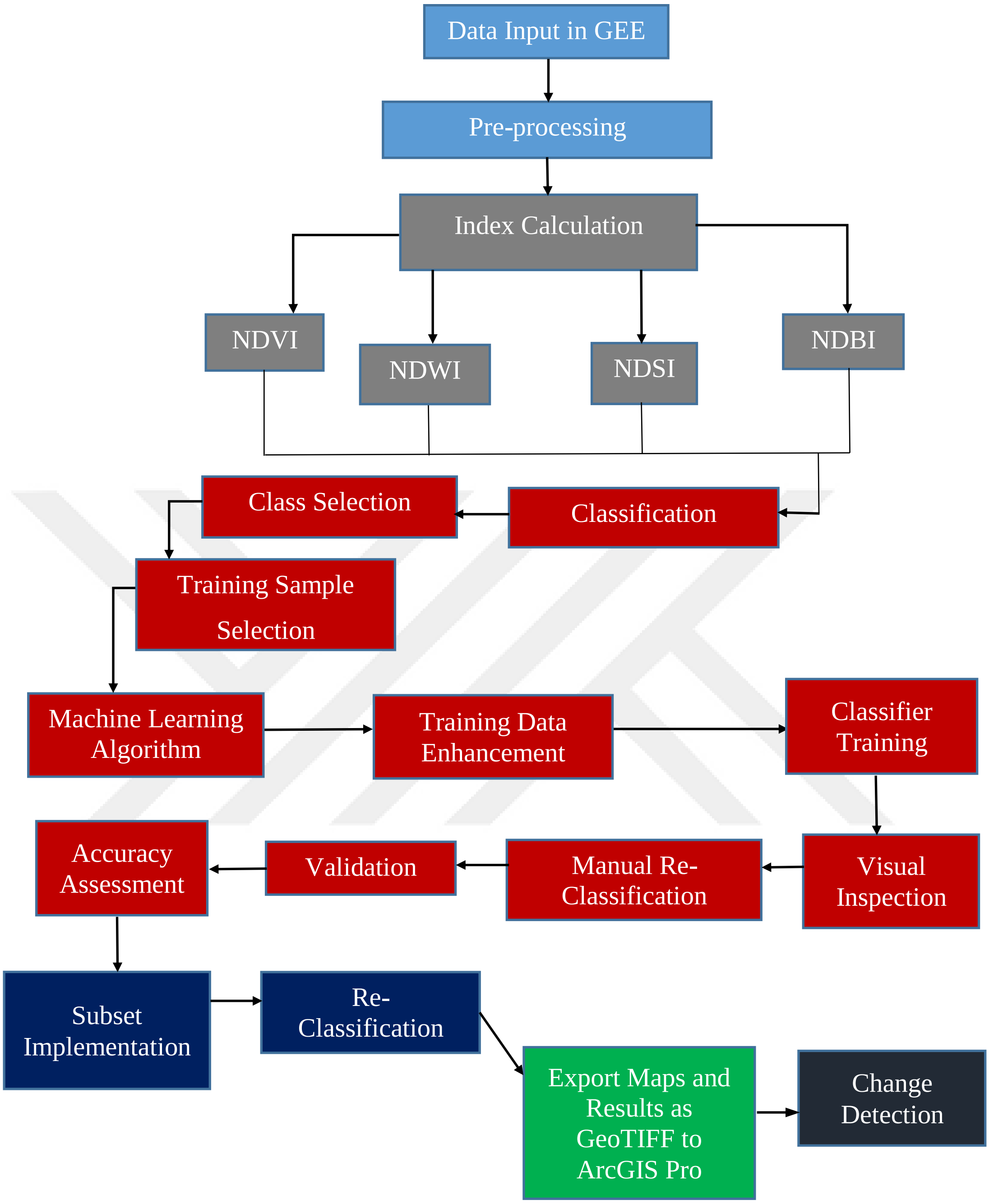

Figure 3.2 Workflow of the Study Area

3.2.1. Index Calculation with Spectral Indices

Spectral Indices can be defined as mathematical formulas and concepts that are designed to use reflectance values of specific spectral bands derived from Remote Sensing data used to better understanding of imagery. There are various spectral indices with different band combinations integrated for a specific purpose. The commonly used indices also used for this study are defined as; Normalized Difference Vegetation Index (NDVI), Normalized Difference Water Index (NDWI), Normalized Difference Snow Index (NDSI) and Normalized Difference Built-up

Index (NDBI). NDVI is an index used to analyze green vegetation and uses the Near-Infrared Band (B8) and Red Band (B4) in Sentinel-2. NDVI is calculated using this formula for Sentinel-2 as follows:

$$\mathrm{NDVI} = \frac{\mathrm{B8-B4}}{\mathrm{B8+B4}} \tag{3.1}$$

NDWI, is a remote sensing index used to calculate the change in the water content of leaves. It is a derived from the Green (B3) and Near-Infrared (B8) band channels. It is calculated as follows:

$$\mathrm{NDWI} = \frac{\mathrm{B3-B8}}{\mathrm{B3+B8}} \tag{3.2}$$

NDSI is also an index that is used to analyze the presence of snow in an acquired pixel of an area and snow detection. It is derived from the Green (B3) and SWIR (B11) bands. The NDSI index for Sentinel-2 is calculated as follows:

$$\mathrm{NDSI} = \frac{\mathrm{B3-B11}}{\mathrm{B3+B11}} \tag{3.3}$$

In addition, to analyze the urban-areas NDBI which is derived from the NIR (B8) and SWIR (B11) bands, can also be estimated by;

$$\mathrm{NDBI} = \frac{\mathrm{B11-B8}}{\mathrm{B11+B8}} \tag{3.4}$$

3.2.2. Classification in Remote Sensing

Classification in remote sensing is described as the process of placing labels to image objects or pixels into different classes based on spectral properties. The labels represent different land cover types and areas. There are two main types of classification in remote sensing and are categorized as Supervised Classification and Unsupervised Classification.

Supervised Classification

Supervised Classification involves obtaining training samples by a user to train a model or classifier. A set of different training samples, from a study area are selected by a user and labeled according to the corresponding desired land cover class. With these trained samples, the chosen classifier implements the spectral patterns related to each class and applies them to the pixels and objects of an image. The widely used Supervised Classification algorithms are Random Forest (RF), Maximum Likelihood Classification (MLC) and Support Vector Machine (SVM).

Unsupervised Classification

Unsupervised Classification involves or relies on installed algorithms to classify a training model. It uses inherited statistical properties and similarities in an image to group pixels or objects into clusters or classes. The algorithm automatically identifies classes or clusters based on the spectral similarity of the pixels or objects. Unsupervised Classification is considered a first step in image classification and analysis and the results are used as a statistical reference while, Supervised Classification is preferred widely for various studies and research because of its ability to provide accurate results and offer a user-friendly environment to implement several algorithms and processes to obtain results.

3.2.3. Processing with Google Earth Engine (GEE)

Google Earth Engine (GEE) is a cloud based geospatial platform that was developed by Google to efficiently analyze and process massive amounts of Earth observation data without the use of traditional conventions. It combines a vast archive of satellite and aerial imagery with a powerful computing infrastructure, allowing users to conduct a wide range of geospatial analyses, from land cover classification to monitoring and climate change analysis.

The platform offers an expansive and up-to-date repository of satellite and Earth observation data, including imagery from missions such as Landsat, Sentinel, MODIS, and more. This extensive data archive is accessible through an easy-to-use JavaScript-based API, which enables users to interact with the data and apply a variety of geospatial algorithms without the need for complex data management and storage. With Earth Engine, users can perform tasks like time series analysis, object detection, change detection and land classification, making it a versatile tool for addressing complex environmental and societal challenges.

The standout features of Google Earth Engine is its scalability and computational power. It leverages Google's cloud infrastructure to distribute computation, enabling users to analyze large datasets and perform data-intensive tasks at speed. This capability is particularly valuable for researchers and organizations working on global-scale environmental monitoring, disaster response, and land management. By providing a platform that integrates data access, analysis tools, and high-performance computing, Google Earth Engine has become an essential resource for those seeking to better understand and address pressing global issues related to Earth's changing environment.

Furthermore, Google Earth Engine provides an open and collaborative platform where users can share their geospatial analyses and findings with the global community and other geospatial users. This collaborative aspect fosters interdisciplinary research and encourages the development of innovative solutions to pressing global issues. As Earth Engine continues to evolve and expand its dataset offerings, it plays an increasingly vital role in advancing our understanding of our planet's dynamic processes and supporting evidence-based decision-making at local, regional, and global scales.

To access the Sentinel 2 MSI Multispectral Instrument, Level 2A in GEE, the collection snippet was accessed from the Earth Engine Data catalog and imported into the code editor as an image collection as shown in Figure 3.3.

```
// Import Sentinel 2 Imagery and define variable
var s2 = ee.ImageCollection("COPERNICUS/S2_SR");
```

Figure 3.3 Sentinel 2 Imagery Import

Secondly, pre-processing parameters were implemented on the image collection. As the study area is prone to clear skies in summer, the filter for the date was placed for a period from June to August for each year. The image collection was filtered to include only images with a cloudy percentage less than 2% and a band collection from B1 to B12. In addition, to create a composite image representing the study area in the specified period, the median value was computed for each band across the filtered images. The shapefile of the study area, which is a widely used geospatial vector data format in GIS applications and is used for storing both the geometry and attribute information of geographic features, such as points, lines, and polygons was inserted as an import file in the code editor and clipped according to the specific region from the satellite imagery. Visualization parameters for the imagery were also added with a focus on the RGB bands B4, B3, B2 and min and max for the pixel values including the gamma value for brightness inserted.

```
// Pre-processing and filtering for 2018 June-August
var image = s2.filter(ee.Filter.bounds(Adana))
               .filter(ee.Filter.date('2018-06-01', '2018-08-31'))
               .filter(ee.Filter.lt('CLOUDY_PIXEL_PERCENTAGE', 2))
               .select(['B1', 'B2', 'B3', 'B4', 'B5', 'B6', 'B7', 'B8',
'B8A', 'B9', 'B11', 'B12'])
               .median()
               .clip(Adana);
// Visualization
var vizParams = {bands: ['B4', 'B3', 'B2'], min: 0, max: 2500, gamma: 1.1};
Map.addLayer(image, vizParams, 'Adana_2018_Summer');
```

Figure 3.4 Pre-processing and Visualization

```
// To remove cloud cover
var mask2clouds = function(image){
var qa = image.select('QA60');
var cloudBitMaks = 1 << 10;
var cirrusBitMaks = 1 << 11;
var mask = qa.bitwiseAnd(cloudBitMaks).eq(0) //specify 0 for no cloud
.and(qa.bitwiseAnd(cirrusBitMaks).eq(0));  //specify 0 for no cirrus
return image.updateMask(mask);
};
```

Figure 3.5 Cloud Cover Masking

Furthermore, as shown in Figure 3.5 pre-processing was conducted to remove cloud cover using the function mask2clouds based on the embedded quality assurance (QA) band. It provides information on the quality and reliability of pixel values in their respective spectral bands and is bit- encoded to represent various flags and indicators related to the acquisition of data and processing. Firstly, the functions select the QA60 band containing the QA from the imagery. The variable cloudBitMaks is assigned a value obtained by left-shifting the number 1 by 10 positions setting the 10^{th} bit to 1 and all other bits to 0 thereby representing the cloud pixels in the QA band. The variable cirrusBitMaks is also assigned a value obtained by left-shifting the number 1 by 11 positions which sets the 11^{th} bit to 1 and all other bits to 0 and represent the cloud pixels in the QA band. Bitwise operations on the QA band are performed to create a cloud and cirrus mask. Iterations are performed on both the cloud bit mask and cirrus mask. It checks if the result is equal to 0 on both meaning no cloud or cirrus cloud and the function later returns the image after applying the mask by masking out the pixels in the image when the mask is false.

The masked image was later merged with the real image to obtain a cloud free composite image. This process is repeated for the years 2019, 2020, 2021 and 2022, respectively, as shown in the Figure 3.6.

```
// Merge cloud free image with real image
var image_cloudfree = s2.filter(ee.Filter.bounds(Adana))
               .filter(ee.Filter.date('2018-06-01', '2018-08-31'))
               .filter(ee.Filter.lt('CLOUDY_PIXEL_PERCENTAGE', 2))
               .map(mask2clouds) // apply map to add the masked image
               .select(['B1', 'B2', 'B3', 'B4', 'B5', 'B6', 'B7', 'B8',
'B8A', 'B9', 'B11', 'B12'])
               .median()
               .clip(Adana);
var vizParams_cloudfree = {bands: ['B4', 'B3', 'B2'], min: 0, max: 2500,
gamma: 1.1};
Map.addLayer(image_cloudfree, vizParams_cloudfree,
'ADANA_2018_CLOUDFREE_SUMMER');
```

Figure 3. 6 Merge Cloud Cover Image to Real Image

To obtain a feature extraction of spectral indices from the study area, four (4) main indices were put into consideration to portray and analyze the main cover types related to LULC studies such as vegetation, water, built-up area, snow etc. The four main spectral indices put into consideration were NDVI, NDWI, NDSI and NDBI Index.

To perform a calculation for NDVI in GEE several key procedures were implemented too. First and foremost, calculation based on the formula for Sentinel 2 was conducted on the cloud free composite image ('image_cloudfree') using the '.normalizedDifference ()' function embedded in GEE. The function performs a calculation between two bands, in this case for NDVI near infrared (NIR) band ('B8') and red band ('B4') by subtracting the value of the second band from the value of the first band and then dividing the result by the sum of the two bands. The resulting NDVI values range from -1 to 1 with visualization parameters set for the results.

Furthermore, to analyze the NDVI change over a year period, the time series analysis was modified to display the average mean NDVI values from each day in 2018. However, to accurately implement this, pre-processing parameters were implemented. The start date was filtered to January 1st and the end date to December 31st, additionally an image collection with Sentinel 2 Level 2A imagery with a cloud pixel percentage of less than 2% was selected as Figure 3.7 clearly outlines. Mask2clouds function applied to remove cloud cover in each collection and implementing the 'distinct' function to remove duplicate images with the same acquisition date.

```
// NDVI
// Calculate NDVI using function
// NDVI = (NIR - Red) / (NIR + Red) or (B8 - B4) / (B8 + B4)
var ndvi_2018 = image_cloudfree.normalizedDifference(['B8','B4']);
Map.addLayer(ndvi_2018, {min:-1, max:1,
palette:['blue','red','yellow','green']}, 'NDVI_2018');
// Create an image collection for the months in the specified date range
// Pre-process data
var startDate = ee.Date.fromYMD(2018, 1, 01);
var endDate = ee.Date.fromYMD(2018, 12, 31);
var s2 = ee.ImageCollection('COPERNICUS/S2_SR')
              .filterBounds(Adana)
              .filterDate(startDate, endDate)
              .filter(ee.Filter.lt('CLOUDY_PIXEL_PERCENTAGE', 2))
              .map(mask2clouds);
var images = s2.map(function(image) {
  var ndvi = image.normalizedDifference(['B8', 'B4']).rename('ndvi_2018');
  return ndvi.set('system:time_start', image.get('system:time_start'));
}).distinct('system:time_start');
```

Figure 3.7 Spectral Indices Calculation

Finally in the code snippet in Figure 3.8, a time series chart was created using the 'ui.Chart.image.doySeries' function to display values for the whole year while also including a histogram to display the frequency distribution of NDVI values within the study area.

```
// Time Series Chart
var chart = ui.Chart.image.doySeries(images, Adana, ee.Reducer.mean(),
10*10)
                 .setChartType('LineChart')
                 .setOptions({
                   title: 'NDVI 2018 Time Series',
                   vAxis: {title: 'NDVI'},
                   hAxis: {title: 'Day Number from Year'},
                   lineWidth: 1,
                   pointSize: 2,
                   series: {0: {color: 'green'}}
                 });
print(chart);
// Add histogram of NDVI values
var ndvi_hist = ui.Chart.image.histogram(ndvi_2018, Adana, 10*10)
                  .setSeriesNames(['NDVI'])
                  .setOptions({
                    title: 'NDVI 2018 Histogram',
                    hAxis: {title: 'NDVI', minValue: -1, maxValue: 1},
                    vAxis: {title: 'Frequency'},
                    colors: ['green']
                  });
print(ndvi_hist);
```

Figure 3.8 Time Series Chart and Histogram

The similar procedure was also applied to obtain yearly values for NDWI, NDSI and NDBI, respectively. The main major changes implemented were the band names and calculations used for the normalized difference embedded function in GEE. NDWI, involved the use of ‘B3’ and ‘B8’, NDSI involved ‘B3’ and ‘B11’ while NDBI involved ‘B11’ and ‘B8’. The time series chart and histogram were also generated for the respective spectral indices. This process was then also applied to the other datasets of 2019, 2020, 2021 and 2022, respectively.

The classification process in GEE involved complex methods and various interactions. This sub-chapter explains all the processes and methods used for classification of the study area.

The first step involved defining the appropriate land cover classes associated with the region. The Esri 2020 Global Land Cover Map was used as a reference to select classes and their appropriate visualization parameters. Seven (7) distinct classes were selected as Water, Trees, Flooded Vegetation, Crops, Built-up Area, Bare Ground and Rangeland. A separate feature collection with the class property and value ranging from 0 to 6 was also assigned to each class including the distinct color referenced from Esri.

Training samples were collected from the ‘image_cloudfree’ true image map and spectral indices maps such as NDVI to correctly identify vegetation areas from the rest. Furthermore, training points were selected in GEE using the ‘Add a marker’ tool and inserted as a Geometry to the imports in the code editor. 110 training samples for Water were selected, 205 for Trees, 166 for Flooded Vegetation, 255 for Crops, 344 for Built-up Area, 53 for Bare Ground and 1314 for Rangeland. The samples were spread across the study area to capture as many training samples as possible for the classifier. Later the individual feature collections representing different land cover classes were merged together using the 'merge ()' function. The seven-class feature collection were merged to create a single training feature collection. The 12 bands were also merged with the cloud free image to create an input.

To increase and enhance the classification process a spatial join with land cover was added using the Copernicus Land Cover Map as shown in Figure 3.9. The spatial join is essential in the essence that it provides reliable ground truth information, increases the discriminate power of the model, ensures an accurate class label assignment, improves transferability and easily facilities the validation and evaluation of classification results.

```
//Classification
// Add and Merge Training information of created training points
var training =
Water.merge(Trees).merge(Flooded_Vegetation).merge(Crops).merge(Built_Area)
.merge(Bare_Ground).merge(Rangeland);
print(training);
// Add the bands and Class properties don't add B10
var label = 'Class';
var bands =
['B1','B2','B3','B4','B5','B6','B7','B8','B8A','B9','B11','B12'];
var input = image_cloudfree.select(bands);
// Spatially join high-resolution land cover dataset with training data
var lc = ee.Image('COPERNICUS/Landcover/100m/Proba-V-C3/Global/2019')
          .select('discrete_classification')
          .clip(Adana);
training = training.map(function(feature){
  return feature.set('lc', lc.reduceRegion({
    reducer: ee.Reducer.mode(),
    geometry: feature.geometry(),
    scale: 10,
  }).get('discrete_classification'))
});
```

Figure 3.9 Classification and Training Implementation

After performing a spatial join, the training and testing data were split and samples with a random value of less than 0.9 were considered part of the training set while samples with a random value greater than or equal to 0.9 were considered part of the testing set, To implement this is in GEE the 'ee.Filter.lessThan ()' and 'ee.Filter.greaterThanOrEquals ()' filters were used to filter the training data accordingly.

A trial and test of all the Machine Learning Algorithms embedded in GEE was conducted on the training data. The Random Forest as shown in Figure 3.10 produced the best results and was selected for classification. In addition, to enhance the classifier the hyper parameters such as number of trees, minimum leaf population, bag fraction, seed and variables per split were also added to the model. After running the classifier to generate a classified image a palette with defined colors referenced from ESRI representing different land cover classes for visualization purposes was inserted in the code editor. Finally, the classified image was added to the map using 'Map.addLayer ()' with the specified visualization parameters.

```
// Classifier Training
var trainImage = input.sampleRegions({
  collection: training,
  properties: [label, 'lc'],
  scale:10,
  tileScale: 4
});
var trainingData = trainImage.randomColumn();
var trainset = trainingData.filter(ee.Filter.lessThan('random',0.9));
var testset =
trainingData.filter(ee.Filter.greaterThanOrEquals('random',0.9));
// Hyperparameters
var classifier = ee.Classifier.smileRandomForest({
  numberOfTrees: 500, // number of trees in the forest
  minLeafPopulation: 10, // minimum number of pixels allowed in a leaf node
  bagFraction: 0.5,
  seed: 0,
  variablesPerSplit: 12
 }).train(trainset,label,bands);
//We define the classified Image
var classified = input.classify(classifier);
//Define a Palette for the classification
var Palette =
['1a5bab','358221','87d19e','ffdb5c','ed022a','ede9e4','c6ad8d'];
print(Palette);
Map.addLayer(classified.clip(Adana), {palette:Palette,
min:0,max:6},'Classified Image');
```

Figure 3.10 Classifier Training and Hyperparameters Tuning

Visual inspection is a necessary step in all remote sensing classification studies, it helps the user to process the accuracy and identity of the results. While automated classification algorithms are able to perform initial land cover classification and analysis, they tend to not always capture all the nuances and variations in the imagery accurately. As such, the results may face some discrepancies in classification. Visual Inspection was important in the essence that it helped identify errors or misclassifications that might have occurred during the automated classification process. By visually examining the classified image in comparison with high-resolution imagery from Google Earth Pro used as ground truth data, discrepancies and inconsistencies were easily identified.

An understanding of the results related to spectral confusion also gave options to explore other methodologies of getting accurate results for the classification. For misclassified pixels Manual Re-Classification was conducted by re-selecting training samples from the incorrectly classified classes and replacing training samples with visually corrected ones referenced from the ground truth data. Incorporating both methodologies to improve and refine the accuracy of land cover classification and final maps proved to be helpful in obtaining overall quality and reliability of the classified information.

An accuracy assessment is also an essential step in land cover classification and involves evaluating the accuracy and reliability of classified results. It helps in identifying areas of high and low accuracy, misclassifications, and potential sources of error and offers guidance of how to improve classification algorithms, parameter selection, training data and determination of classes to be used. To implement the accuracy assessment, five (5) accuracy metrics were put into consideration as;

1. Confusion Matrix
2. Consumer's Accuracy
3. Producer's Accuracy
4. Overall Accuracy
5. Kappa Statistic

A confusion matrix is a table that is commonly used to describe the performance of a classification model or classifier on a set of test data whose true values are known. It contains data on actual and predicted classifications performed by the model. It consists of four components: It has four components:

- True positive (TP) - means predictions are correct and labeled as positive.
- False negative (FN) – means predictions are incorrectly labeled as negative.
- False positive (FP) - refer to incorrectly labeled positive predictions.
- True negative (TN) – refer to correct negative predictions.

This metric measures how accurate the model's predictions are within a given class. It measures the chance that a pixel or object classified as a particular class truly belongs to that class or a portion of the correct positive predictions in the confusion matrix out of all positive predictions.. It is used to specify how the accuracy of the existing data and is calculated using the following formula:

$$\text{Consumer's Accuracy} = \frac{\text{Numbers of specific class correctly classified}}{\text{Row Total}} \times 100 \text{ or } \frac{\text{TP}}{\text{TP+FP}} \times 100 \quad (3.5)$$

This metric evaluates how well the model predicts the occurrence of a specific class. It measures the chance that a pixel or object of a specific class is correctly classified. It is used to determine how well the model predicts new data and is calculated using the following formula:

$$\text{Producer's Accuracy} = \frac{\text{Numbers of features of a specific class}}{\text{Row Total}} \times 100 \ \text{ or } \ \frac{\text{TP}}{\text{TP+FN}} \times 100 \tag{3.6}$$

The overall accuracy is the total number of features correctly classified and divided by the total number of features multiplied by 100. It is calculated as follows:

$$\text{Overall Accuracy} = \frac{\text{Numbers of features correctly classified}}{\text{Total number of features}} \times 100 \tag{3.7}$$

The Kappa Statistic, also known as Cohen's Kappa or simply Kappa, is another important metric used to assess classification accuracy, particularly with categorical data. It quantifies the agreement between the classification results and the reference ground truth data, taking into account the possibility of agreement by chance. The formula for the Kappa statistic is as follows:

$$\text{Kappa Statistic} = \frac{\text{Observed Agreement (Po)} - \text{Estimated Agreement (Pe)}}{1 - \text{Expected Agreement (Pe)}} \tag{3.8}$$

By obtaining all the information related to these 5 metrics, evaluating the process of the classification model to understand the performance and reliability of the output was made easy. The following steps were implemented in GEE to perform an Accuracy Assessment;

1. The test set from the split training data in the classification process was used for testing the accuracy of the classification model.
2. The 'errorMatrix' function was applied to the test set's classified results to generate an error matrix. The 'Class' parameter represents the actual class labels from the reference data, while the 'Classification' parameter represents the predicted class labels from classification.
3. The five (5) accuracy parameters were then printed in the console of the code editor as numerical values to give the information related to the Accuracy Assessment.

```
// Accuracy Assessment
var confusionMatrix = ee.ConfusionMatrix(testset.classify(classifier)
    .errorMatrix({
      actual:'Class',
      predicted:'classification'
  }));
print('Confusion Matrix:', confusionMatrix);
print("Consumer's accuracy", confusionMatrix.consumersAccuracy());
print("Producer's accuracy", confusionMatrix.producersAccuracy());
print('Kappa statistic', confusionMatrix.kappa());
print('Overall Accuracy:', confusionMatrix.accuracy());
```
Figure 3.11 Accuracy Assessment

To obtain a more focused analysis and examination of the study area which was categorized as a large study area. A new methodology that involved extracting a distinct subset from the original study area dataset was implemented. The coordinates and geometry of the subset were defined to include all the 7 land cover classes derived from the initial original dataset. New training samples and feature collections were assigned to the subset including the extraction of spectral indices.

Re-classification with the same Machine Learning Algorithm was performed and later a visual inspection to analyze the results with the initial original image. Both datasets were recorded and accuracies compared for a detailed validation.

Change detection is the final step in GIS analysis, and it is primarily used to identify changes in land cover, land use, and other spatial features. The image differencing method was used in the study to analyze percentage changes in area over a five-year period. Image differencing is a change detection method that compares two images of the same area taken at different times to determine which areas have changed. The difference image can be a thresholder or classified to determine which areas have changed and which have not changed. Image differencing can be applied to single-band or multi-band images, but it requires that the images have the same spatial resolution, spectral resolution, and radiometric calibration. Image differencing can detect both positive and negative changes, but it may not be able to distinguish different types or causes of changes. In contrast to its advantages, image differencing may also be affected by noise, errors, or variations in the data, such as atmospheric effects, illumination conditions, viewing angles, or seasonal changes. Therefore, image differencing may require some preprocessing, filtering, or correction steps to improve the reliability of the results.

Change detection for this study involved subtracting the pixel values of two images taken at different times and divide the result by the pixel value of the first image. This method was easy to implement and interpret, but it may be sensitive to noise, errors, or variations in the data hence required caution and implementation of various parameters and thresholds.

The exportation of Maps and Results was the last step in the study and classification in GEE. The main reasons and aim of the data export in GIS was mapping, visualization and presentation of the results. All the data was exported as GeoTIFF files which are known for preserving the spatial information, pixel values and metadata of the original maps. Exporting as a GeoTIFF helps to retain the accuracy and integrity of the data hence ensuring its full reliability for usage in ArcGIS Pro without loss of information.

ArcGIS Pro in turn, provides a wide range of visualization options for GeoTIFF files and Raster data hence making it suitable for enhancing and customizing the appearance of the maps to suit presentation needs. In addition, ArcGIS Pro and GEE are designed to work compatibly over several projects that involve data exchange.

The whole process of data export involved acquiring all the maps and graphs including the subsets from 2018 to 2022. The data was exported to the Google Drive and later imported to ArcGIS Pro as GeoTIFF files. Further customizing and visualization setting was conducted in ArcGIS Pro and results presented as Maps.

GeoTIFF files are a popular format for storing georeferenced raster images. They can include metadata such as the coordinate system and georeferencing information, which is crucial for ensuring the spatial accuracy of the maps. This makes GeoTIFF an ideal format for exporting data from Google Earth Engine (GEE) to ArcGIS Pro, as it ensures that the spatial information, pixel values, and metadata of the original maps are preserved. This is important in studies where maintaining the integrity and reliability of the data is paramount.

However, ArcGIS Pro offers a wide range of visualization options for GeoTIFF files and raster data. This includes various rendering options, symbology settings, and transparency controls, among others. These features allow you to enhance and customize the appearance of your maps to suit your presentation needs. For instance, you can use different color ramps to represent different ranges of data values, apply transparency to overlay multiple layers, or use 3D visualization tools for a more immersive experience.

4. RESULTS AND DISCUSSIONS

The Chapter provides the comprehensive findings and details obtained through the research methodology. It highlights the step by step process followed and the data acquired to investigate the research topic. The results are presented and discussed in a structured manner, as provided in the material and method’s chapter while also providing valuable insights and interpretations. The key findings are further analyzed and discussed in-depth, focusing on their relevance to the research objectives. Furthermore, research outcomes are compared and contrasted with the initial hypotheses or research questions, highlighting any agreements or disparities. The implications of the findings are explored, considering their practical applications, theoretical contributions, or policy implications while the difficulties of the study are acknowledged, and areas for further research and improvement are identified. The chapter concludes by summarizing the main findings and their significance in addressing the research objectives. The conclusions drawn from the research are reinforced, emphasizing their validity and reliability. Finally, recommendations are provided based on the findings, suggesting practical actions or future directions for the subject area.

4.1. NSpectral Indices

Results and discussions were made for four (4) crucial spectral indices in this study that included NDVI, NDWI, NDSI, and NDBI. However, to technically analyze the spectral indices on a yearly interval, separate analyses were done for the year 2018, 2019, 2020, 2021 and 2022. A time series chart and distinct mean values were obtained for a respective actual day from the total days in a year. As the Sentinel 2A provides an image collection, images based on a less cloud cover were preferred and used to obtain mean distinct values.

Additionally, after analysis of errors and inconsistencies affecting values of spectral indices such as shadows and mixed pixels, sensor limitations, atmospheric effects and class types were put into consideration. Only time series chart values that showed a consistency over a period of time were selected, values that showed rapid abnormal changes over a short period of time were removed.

4.1.1. NDVI Index

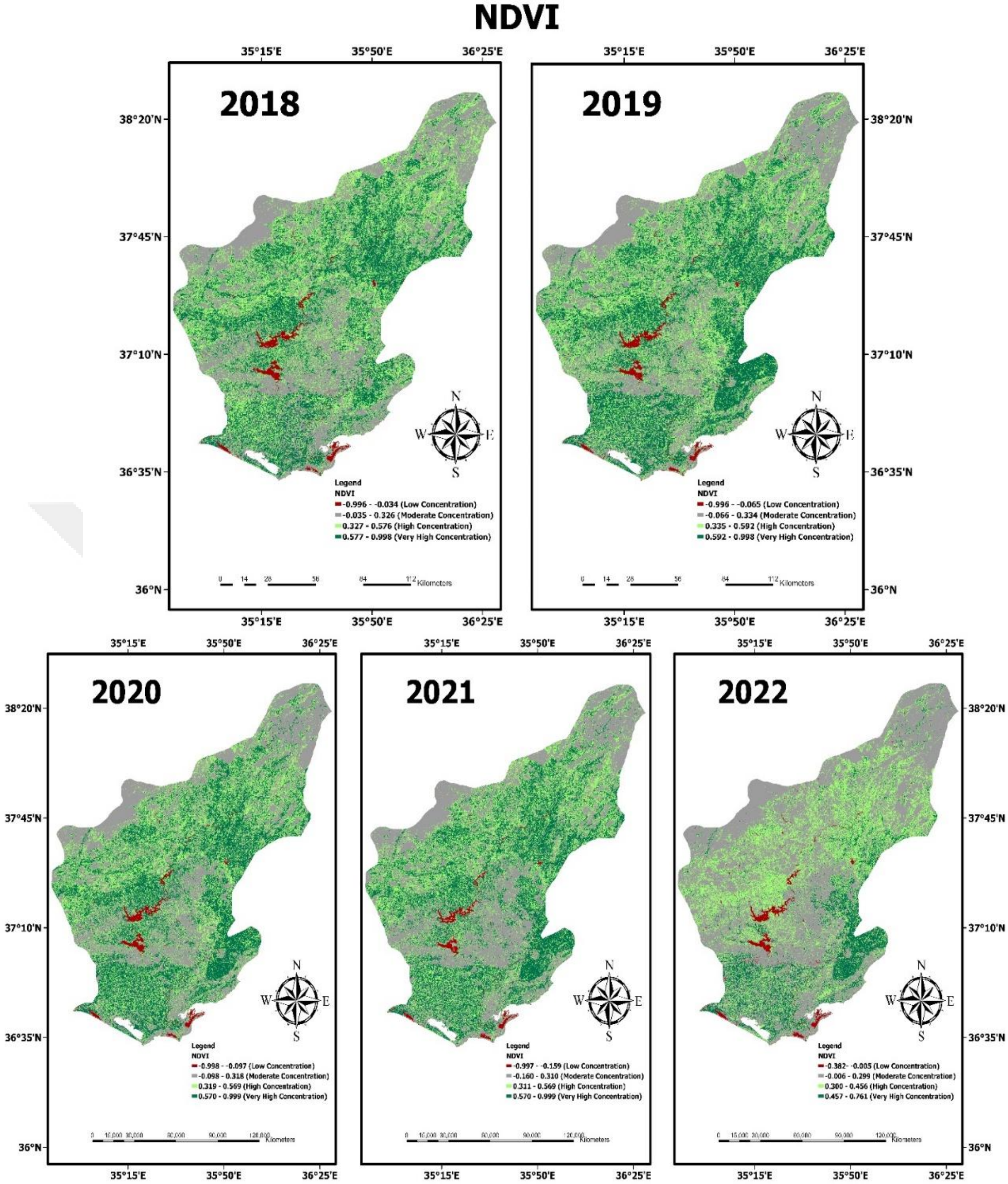

Figure 4.1 NDVI Maps for 2018, 2019, 2020, 2021 and 2022

Figure 4.1 shows detailed maps of the NDVI index over the five (5) year study period as calculated. The Range of NDVI as calculated in Google Earth Engine was set to 1 as the highest and -1 as the lowest. Natural Breaks (Jenks) method in ArcGIS Pro was utilized to separate the range into four (4) parts according to the classes and values. For the year 2018, values with a range of (-0.996 - -0.034) were classified as Low Concentration with red color on the maps, values with range of (-0.035 – 0.326) were classified as Moderate Concentration with grey color, similarly values with a range of (0.327 – 0.576) were classified as High Concentration in light green color while values with a range of (0.577-0.998) were classified as Very High Concentration with dark green color. The concentration intervals classified as Low, Moderate, High and Very High were used to distinguish and provide a clear visual distinction between different levels of vegetation density and health. Low Concentration represented areas with little or no vegetation and possible water bodies, Moderate Concentration was used to represent areas with some vegetation but not densely packed while High Concentration represented areas with a high density of vegetation in good health and Very High Concentration indicated areas with dense, health vegetation in really good health. Similarly, for 2019 the ranges were (-0.996 – 0.065) Low Concentration, (-0.066 – 0.334) Moderate Concentration, (0.335 – 0.592) High Concentration and (0.592 – 0.998) as Very High Concentration. 2020 had the following ranges (-0.998 – -0.097) Low Concentration, (-0.098 – 0.318) Moderate Concentration, (0.319 – 0.569) High Concentration and (0.570 – 0.999) as Very High Concentration. 2021 had (-0.997 – -0.159) Low Concentration, (-0.160 – 0.310) Moderate Concentration, (0.311 – 0.569) High Concentration and (0.570 – 0.999) as Very High Concentration. Lastly, 2022 had the ranges of (-0.382 – - 0.005) Low Concentration, (-0.005 – 0.299) Moderate Concentration, (0.300 – 0.456) High Concentration and (0.457 – 0.761) as Very High Concentration.

The Figures 4.2 to 4.6 represent the time series analysis chart NDVI mean values over each year from 2018 to 2022. A time series analysis chart is a graphical representation of the changes in an index over time for a given area or region. It can be used to compare the trends and patterns of an index across different regions or seasons, hence revealing interesting patterns and correlations that contribute to understanding of the dynamics. It can be used to detect anomalies or outliers that may affect actual results when conducting studies for a specified index. Depending on the program used, these indices are usually plotted over time and represented using a chart of the user’s choice. They aid in tracking changes in environmental conditions and land use essential for decision making, environmental conservation, agriculture and disaster monitoring. Understanding and quantifying changes in different environmental parameters is critical in providing insights and solutions for short period and long period usage of land.

The usage of an NDVI time series analysis chart in our case is multifaceted and significant in the monitoring of vegetation, crops and forests in the area over time. By tracking the changes in the NDVI, it is possible to observe the growth and productivity of these vegetation types. This can be particularly useful in agriculture, where it can help farmers or agriculturists to optimize their crop yields and detect any potential issues early or during the intended period of farming.

As observed further on the NDVI charts, mean values were taken throughout the year. Obtaining the mean values for the yearly time series analysis was crucial in providing a single representative value that captured the overall trend of the data over a specific period. Additionally, since the analysis was done on an image collection of different images for a particular period and sometimes multiple images on a single day obtaining the mean value was considered appropriate and less sensitive to extreme values or outliers in the data that tends to affect the overall results hence calculating the mean value helped reduce noise and smoothed out these variations. The mean value served as a condensed, interpretable metric for each time step, enhancing clarity in visualizations and analyses while also providing consistency for comparative assessments across the yearly period for the NDVI time series analysis.

The time series charts as depicted in Figure 4.2 to Figure 4.6 with the x-axis representing the number of days within the year and y-axis showing the actual NDVI values over the year. The chart was styled as a line chart from the excel graph interface with green color for the line and smaller points for each data point. It is noted to say that all the values that showed rapid changes over a short period of time were filtered out to obtain consistency in the estimated values. Figure 4.2 shows the chart of NDVI mean values for the year 2018 with all its values from interpreted in Table 4.1 including the maximum and minimum values. Mean values from day 9 to day 356 for the year 2018 were illustrated on both the time series chart and the table. Similarly, the same procedure was conducted for the years 2019 to 2022 for NDVI with highest values obtained in 2018 and lowest in 2022 as discussed further in this chapter.

However, the obtained mean NDVI values ought to be regarded as an estimation due to several underlining factors affecting actual results such as temporal fluctuations stemming from diverse weather conditions, seasonal changes, sensor discrepancies, uncertainties during data collection and processing and more importantly the complexity and heterogeneity inherent in the estimation of vegetation health using mean values over a period of time related to our focus of study.

Temporal fluctuations due to diverse weather conditions and seasonal changes can also significantly impact NDVI values. For instance, cloud cover can easily interfere with satellite imagery, leading to lower NDVI values. Similarly, seasonal changes in vegetation growth can cause NDVI values to fluctuate throughout the year. Therefore, it’s crucial to consider the timing of the satellite imagery when interpreting NDVI values as in our case the whole year was put into consideration to get an overall insight.

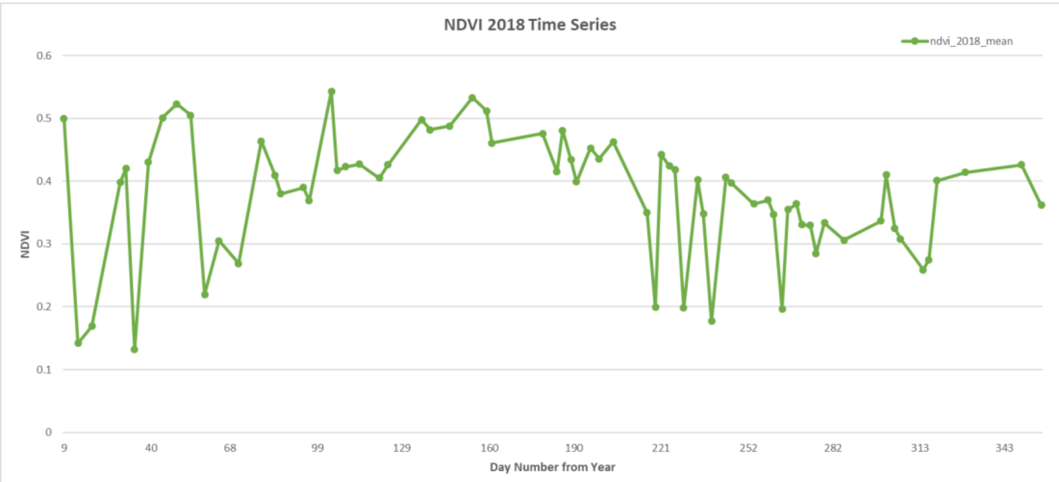

Figure 4.2 2018 NDVI Time Series

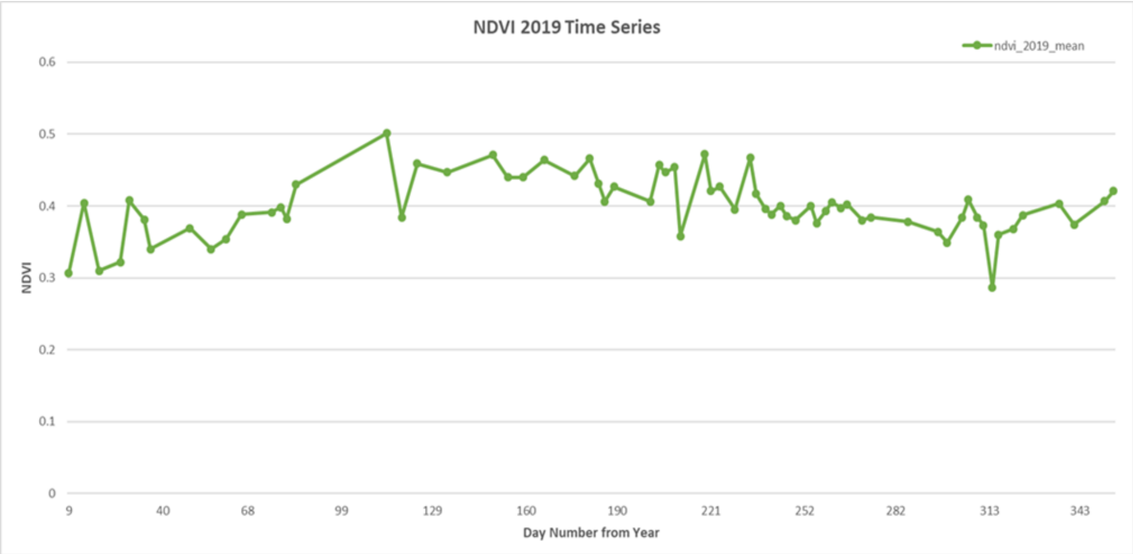

Figure 4.3 2019 NDVI Time Series

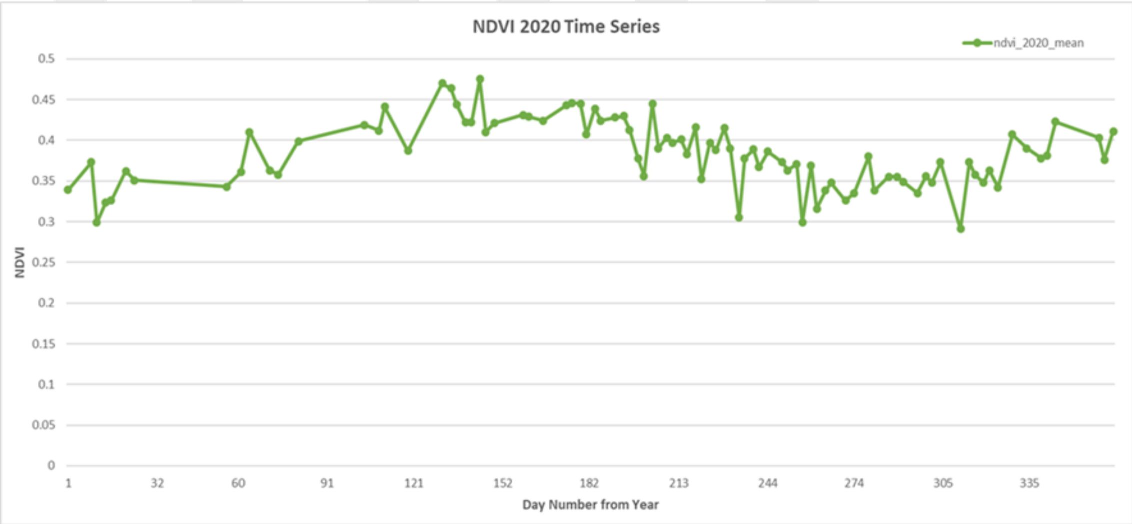

Figure 4.4 2020 NDVI Time Series

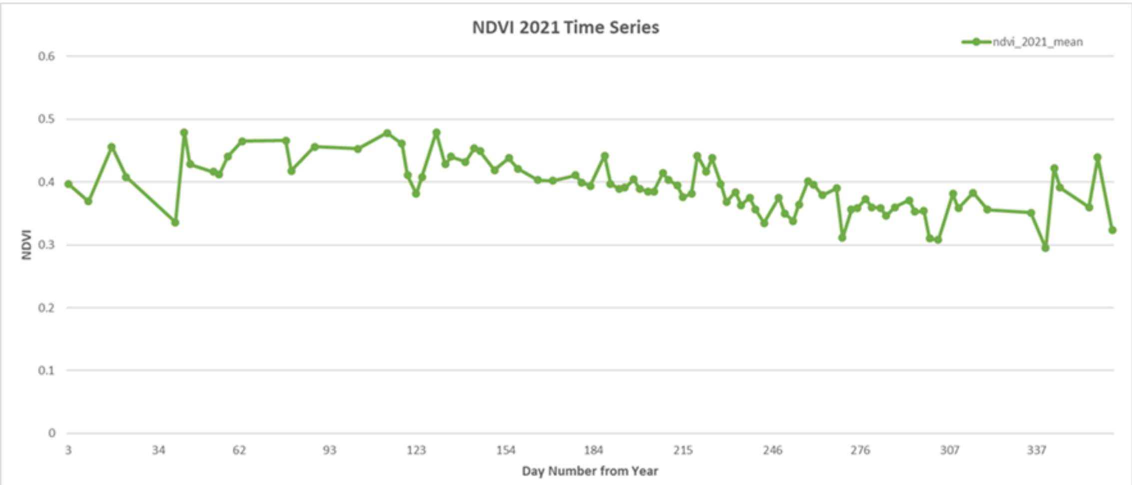

Figure 4.5 2021 NDVI Time Series

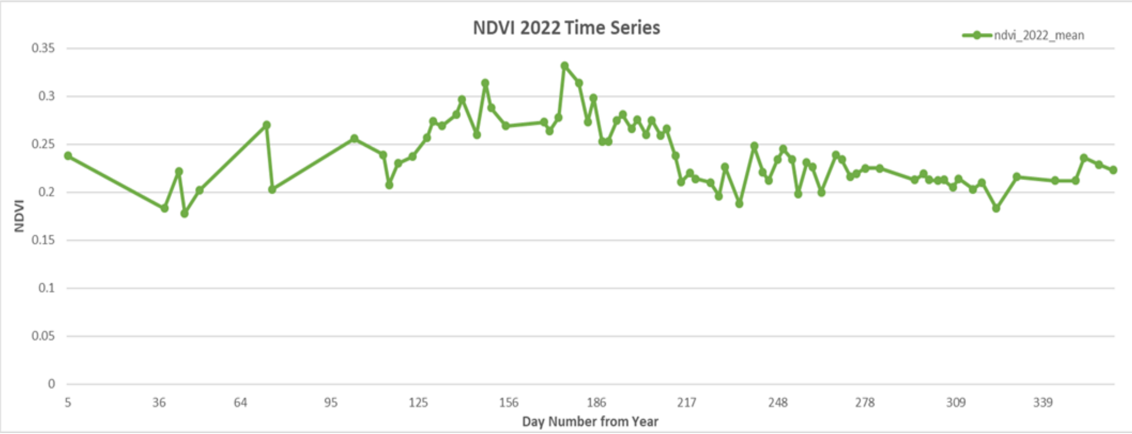

Figure 4.6 2022 NDVI Time Series

As can be shown in Table 4.1 and Table 4.2 below of the NDVI mean values, the highest recorded NDVI mean value for 2018 was 0.543 on day 104 corresponding to 14th April, 2018. On the other hand, the lowest recorded NDVI mean value was 0.132 on day 34 corresponding to 3rd February, 2018. Additionally, for 2019 the highest NDVI mean value recorded was 0.501 on day 114, 24th April, 2019 and the lowest was 0.286 on day 314, 10th November, 2019.

2020, 2021 and 2022 showed highest NDVI mean values of 0.475, 0.479 and 0.332 on days 144, 23rd May, 2020, same 2021 value for day 43, 12th February, 2021 and day 130, 10th May 2021 and lastly on day 175, 24th June, 2022 in sequence, respectively.

The lowest NDVI mean values obtained were 0.291 on day 311, 6th November, 2020, 0.295 on day 340, 6th December, 2021 and 0.178 on day 45, 14th February, 2022, respectively.

As illustrated the highest NDVI mean value obtained over the respective study period was in 2018 at 0.543 and lowest at 0.132. Areas with high NDVI values showcased a dense and healthy vegetation, such as forests and well-maintained agriculture fields while areas with low NDVI values showcased limited vegetation or non-vegetated surfaces such as rocks, sand or urban areas. Seasonal effects can be attributed as the major influencer of NDVI values and other various factors such as infrastructure and quality of imagery. As different types of vegetation have different growth patterns and responses to climate factors such as, in the growing season (spring and summer), plants need more water and nutrients to grow, so they reflect more red light and absorb more blue light. In the dormant season (autumn and winter), plants lose their leaves and reduce their photosynthesis, so they reflect less red light and absorb more blue light. Infrastructure and poor imagery can also be the main triggers of changes in NDVI in a given area.

Table 4.1 2018 and 2019 NDVI Mean Values

ACTUAL DAY OF THE YEAR	2018 NDVI MEAN VALUES	ACTUAL DAY OF THE YEAR	2018 NDVI MEAN VALUES	ACTUAL DAY OF THE YEAR	2019 NDVI MEAN VALUES	ACTUAL DAY OF THE YEAR	2019 NDVI MEAN VALUES
9	0.5	**199**	0.436	**9**	0.307	**221**	0.421
14	0.142	**204**	0.463	**14**	0.404	**224**	0.427
19	0.169	**216**	0.35	**19**	0.31	**229**	0.395
29	0.398	**219**	0.199	**26**	0.322	**234**	0.467
31	0.42	**221**	0.443	**29**	0.408	**236**	0.417
34	0.132	**224**	0.424	**34**	0.381	**239**	0.396
39	0.43	**226**	0.418	**36**	0.34	**241**	0.388
44	0.501	**229**	0.198	**49**	0.369	**244**	0.4
49	0.523	**234**	0.402	**56**	0.34	**246**	0.386
54	0.505	**236**	0.348	**61**	0.354	**249**	0.38
59	0.22	**239**	0.177	**66**	0.388	**254**	0.4
64	0.305	**244**	0.406	**76**	0.391	**256**	0.376
71	0.269	**246**	0.397	**79**	0.398	**259**	0.393
79	0.464	**254**	0.364	**81**	0.382	**261**	0.405
84	0.409	**259**	0.37	**84**	0.43	**264**	0.397
86	0.38	**261**	0.347	**114**	0.501	**266**	0.402
94	0.39	**264**	0.196	**119**	0.384	**271**	0.38
96	0.369	**266**	0.355	**124**	0.459	**274**	0.384
104	0.543	**269**	0.364	**134**	0.447	**286**	0.378
106	0.417	**271**	0.331	**149**	0.471	**296**	0.364
109	0.423	**274**	0.33	**154**	0.44	**299**	0.349
114	0.427	**276**	0.285	**159**	0.44	**304**	0.384
121	0.405	**279**	0.334	**166**	0.464	**306**	0.409
124	0.426	**286**	0.306	**176**	0.442	**309**	0.384
136	0.498	**299**	0.337	**181**	0.466	**311**	0.373
139	0.482	**301**	0.41	**184**	0.431	**314**	0.286
146	0.488	**304**	0.325	**186**	0.406	**316**	0.36
154	0.533	**306**	0.308	**189**	0.427	**321**	0.368
159	0.512	**314**	0.259	**201**	0.406	**324**	0.387
161	0.461	**316**	0.275	**204**	0.457	**336**	0.403
179	0.476	**319**	0.401	**206**	0.447	**341**	0.374
184	0.415	**329**	0.414	**209**	0.454	**351**	0.407
186	0.481	**349**	0.426	**211**	0.358	**354**	0.421
189	0.434	**356**	0.362	**219**	0.472		
191	0.399						
196	0.453						

Table 4.2 2020, 2021 and 2022 NDVI Mean Values

ACTUAL DAY OF THE YEAR	2020 NDVI MEAN VALUES	ACTUAL DAY OF THE YEAR	2020 NDVI MEAN VALUES	ACTUAL DAY OF THE YEAR	2021 NDVI MEAN VALUES	ACTUAL DAY OF THE YEAR	2021 NDVI MEAN VALUES	ACTUAL DAY OF THE YEAR	2022 NDVI MEAN VALUES	ACTUAL DAY OF THE YEAR	2022 NDVI MEAN VALUES
1	0.339	219	0.416	3	0.397	215	0.376	5	0.238	218	0.22
9	0.373	221	0.352	10	0.369	218	0.382	38	0.183	220	0.214
11	0.299	224	0.397	18	0.456	220	0.442	43	0.222	225	0.21
14	0.324	226	0.388	23	0.408	223	0.416	45	0.178	228	0.196
16	0.326	229	0.415	40	0.336	225	0.438	50	0.202	230	0.226
21	0.362	231	0.39	43	0.479	228	0.397	73	0.27	235	0.188
24	0.351	234	0.305	45	0.428	230	0.368	75	0.203	240	0.248
56	0.343	236	0.378	53	0.416	233	0.384	103	0.256	243	0.221
61	0.361	239	0.389	55	0.412	235	0.363	113	0.239	245	0.212
64	0.41	241	0.367	58	0.44	238	0.375	115	0.208	248	0.234
71	0.363	244	0.386	63	0.465	240	0.356	118	0.23	250	0.245
74	0.358	249	0.373	78	0.466	243	0.335	123	0.237	253	0.234
81	0.399	251	0.363	80	0.418	248	0.375	128	0.257	255	0.198
104	0.419	254	0.371	88	0.456	250	0.35	130	0.274	258	0.231
109	0.412	256	0.299	103	0.453	253	0.338	133	0.269	260	0.226
111	0.441	259	0.369	113	0.478	255	0.364	138	0.281	263	0.2
119	0.387	261	0.316	118	0.461	258	0.401	140	0.297	268	0.239
131	0.47	264	0.338	120	0.411	260	0.396	145	0.26	270	0.234
134	0.464	266	0.348	123	0.381	263	0.379	148	0.314	273	0.216
136	0.444	271	0.326	125	0.408	268	0.39	150	0.288	275	0.219
139	0.422	274	0.335	130	0.479	270	0.311	155	0.269	278	0.225
141	0.422	279	0.38	133	0.428	273	0.356	168	0.273	283	0.225
144	0.475	281	0.338	135	0.44	275	0.358	170	0.264	295	0.213
146	0.41	286	0.355	140	0.432	278	0.373	173	0.278	298	0.219
149	0.421	289	0.355	143	0.454	280	0.36	175	0.332	300	0.213
159	0.431	291	0.349	145	0.449	283	0.359	180	0.314	303	0.212
161	0.429	296	0.335	150	0.419	285	0.346	183	0.273	305	0.213
166	0.424	299	0.356	155	0.438	288	0.36	185	0.298	308	0.205
174	0.443	301	0.348	158	0.421	293	0.371	188	0.253	310	0.214
176	0.446	304	0.373	165	0.403	295	0.353	190	0.253	315	0.203
179	0.445	311	0.291	170	0.402	298	0.354	193	0.275	318	0.21
181	0.407	314	0.373	178	0.411	300	0.31	195	0.281	323	0.183
184	0.439	316	0.358	180	0.399	303	0.308	198	0.266	330	0.216
186	0.424	319	0.348	183	0.394	308	0.381	200	0.276	343	0.212
191	0.428	321	0.363	188	0.442	310	0.358	203	0.26	350	0.212
194	0.43	324	0.342	190	0.397	315	0.383	205	0.275	353	0.236
196	0.413	329	0.407	193	0.389	320	0.356	208	0.259	358	0.229
199	0.378	334	0.39	195	0.391	335	0.351	210	0.266	363	0.223
201	0.356	339	0.378	198	0.404	340	0.295	213	0.238		
204	0.445	341	0.381	200	0.389	343	0.422	215	0.211		
206	0.39	344	0.423	203	0.385	345	0.391				
209	0.403	359	0.403	205	0.385	355	0.36				
211	0.397	361	0.376	208	0.414	358	0.439				
214	0.401	364	0.411	210	0.403	363	0.323				
216	0.383			213	0.395						

4.1.2. NDWI Index

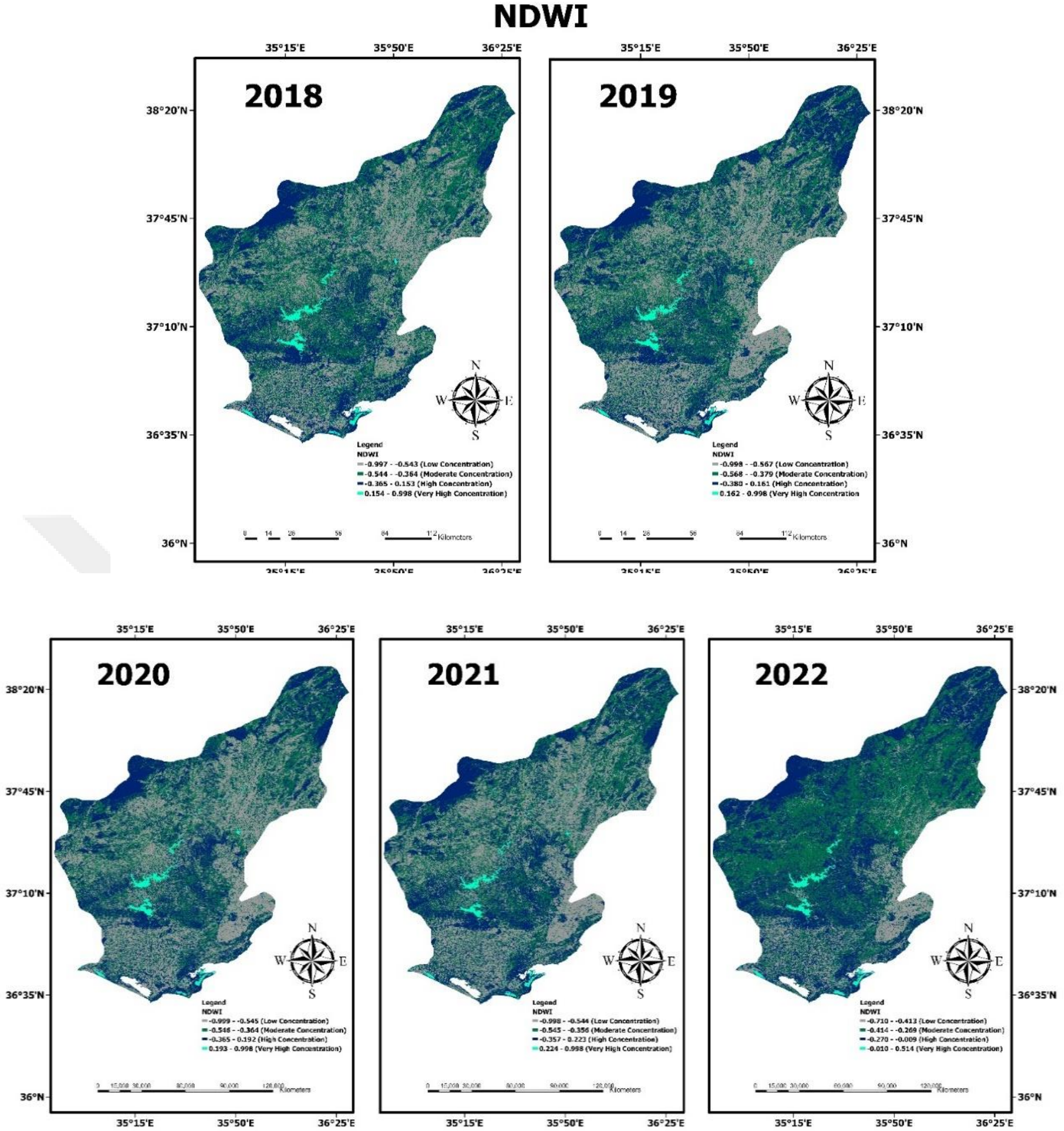

Figure 4.7 NDWI Maps for 2018, 2019, 2020, 2021 and 2022

The ranges of NDWI were also classified in ArcGIS Pro with the help of Natural Breaks (Jenks) method as can be visually observed in Figure 4.7. 2018 had the range values of (-0.997 - -0.543) Low Concentration with grey color, the range (-0.544 - -0.364) depicted Moderate Concentration with dark green color, while (-0.365 – 0.153) was for High Concentration with a dark blue color and (0.154 – 0.998) represented Very High Concentration with light blue color. In comparison to NDVI, the concentration intervals of Low, Moderate, High and Very High were used to help in visualization and understanding the concentration of water in the study area. Low Concentration was used to depict areas with little to no water and moisture content. Moderate Concentration depicted areas with a little water and moisture content while High Concentration represented areas with a high concentration of water and moisture content. Finally, Very High

Concentration depicted areas with very high water and moisture content levels such as water bodies in the area.

2019 produced ranges of (-0.998 - -0.567) Low Concentration, (-0.568 - -0.379) Moderate Concentration, (-0.380 – 0.161) High Concentration and (0.162 – 0.998) as Very High Concentration. Furthermore, 2020 had ranges of (-0.999 - -0.545) Low Concentration, (-0.546 - -0.364) Moderate Concentration, (-0.365 – 0.192) High Concentration and (0.193 – 0.998) as Very High Concentration. 2021 had range results of (-0.998 - -0.544) Low Concentration, (-0.545 - -0.356) Moderate Concentration, (-0.357 – 0.223) High Concentration and (0.224 – 0.998) as Very High Concentration. Lastly, Low Concentration range for 2022 was (-0.710 - -0.413), Moderate Concentration (-0.414 - -0.269), High Concentration of (-0.270 - -0.009) and Very High Concentration of (-0.010 -0.514).

As contrasted from the time series analysis for NDVI, the same similar procedure was applied to the analysis of NDWI for Figure 4.8 to Figure 4.12 shown below. Mean values for a yearly period from 2018 to 2022 were obtained from the satellite image collections and values that showed rapid changes over a short period of time were filtered out as they would have been affected by variations. The x axis represented the number of days within the year and the y axis represented the actual NDWI values over the year. A line chart from the excel graph was also utilized from the Excel interface with blue color and smaller points for each data point as shown in the Figures below. All values obtained for the study period from the yearly time series were illustrated in the Table 4.3 and Table 4.4. The year 2019 had mean values from day 14 to day 356, while 2019 had values from day 9 to day 354 and 2020, 2021 and 2022 had values from day 1 to day 364, day 3 to day 363 and day 3 to day 363, respectively, provided in a sequence. The lowest mean value was observed in 2018 and highest in 2022. As the thresholds for the values were set in the range of -1 to 1, it was evident that the time series showed more mean negative values which suggested that the area is primarily made of soil and terrestrial vegetation with little to no water content and moisture in those areas. Rapid land use, climate change or several variations could also have caused the decrease in the values. Additionally, as the area was obtained from each image collection, collections that had more negative values out shadowed the less positive values because of the mean calculation hence portraying all values as negative on the time series chart. The case however, was different when analyzed from the NDWI maps with the interval Very High Concentration depicted in light blue color with the intervals crossing from negative to positive values, it was clear that all water bodies and areas with high moisture encompassed this interval. The figures below showcase the time series analysis for a yearly period from 2018 to 2022.

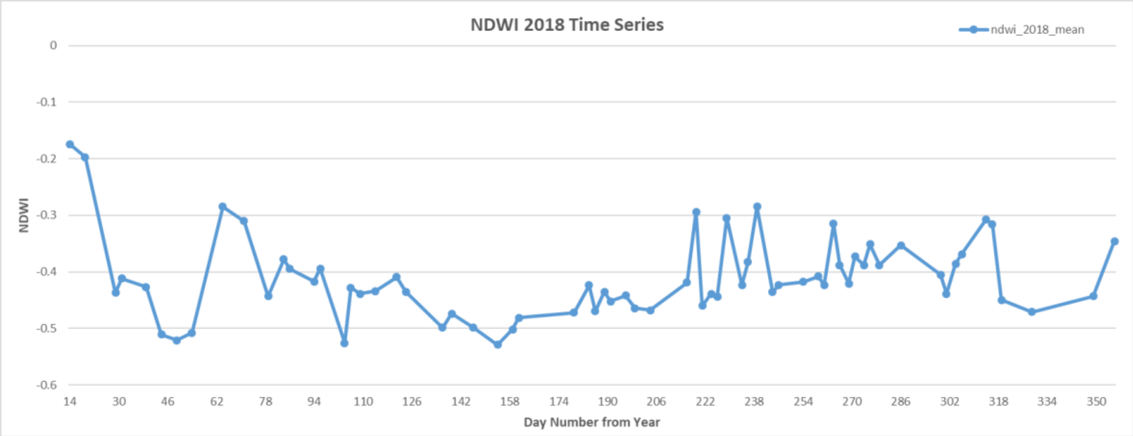

Figure 4.8 2018 NDWI Time Series

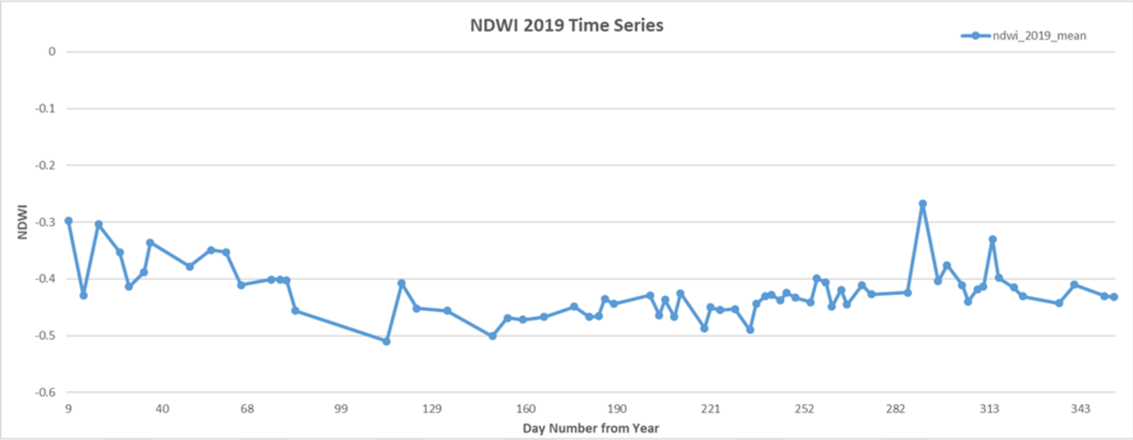

Figure 4.9 2019 NDWI Time Series

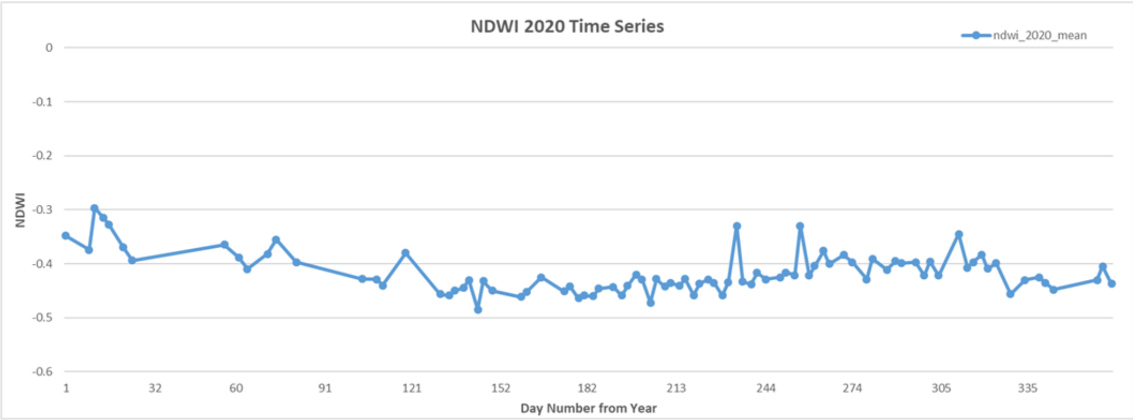

Figure 4.10 2020 NDWI Time Series

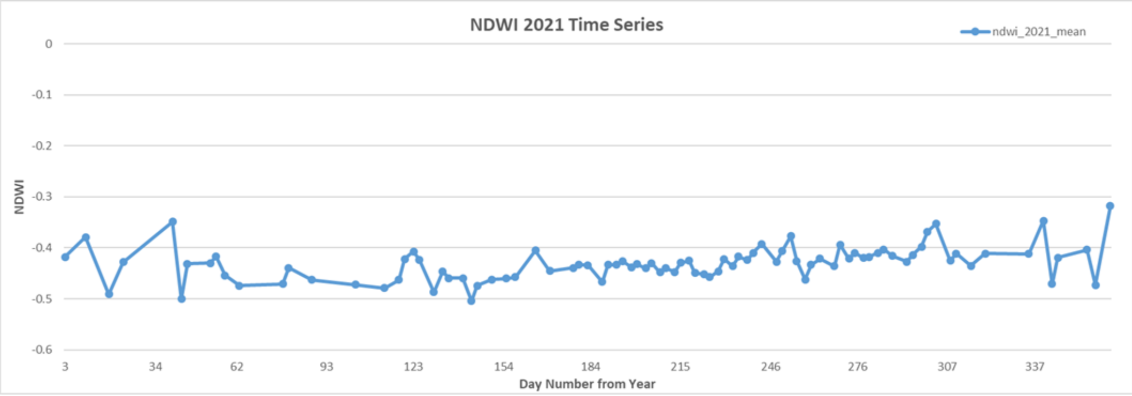

Figure 4.11 2021 NDWI Time Series

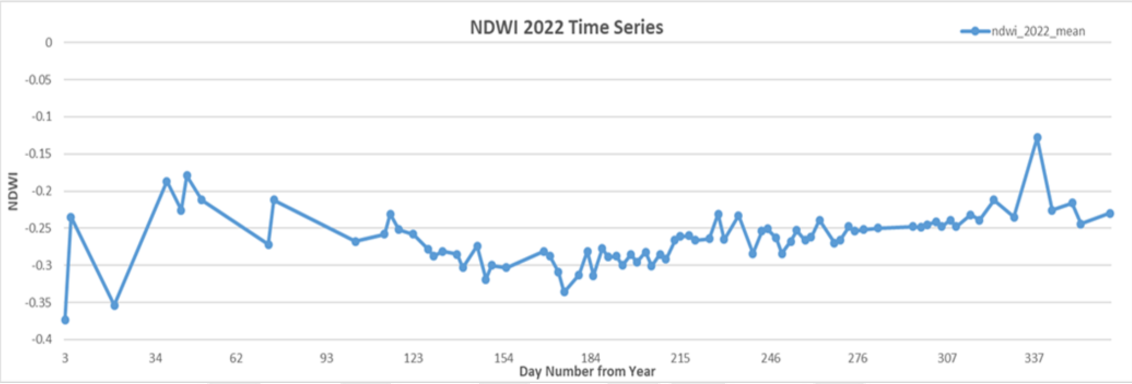

Figure 4.12 2022 NDWI Time Series

As can be observed on Figure 4.8, 2018 Time Series showed a stepper change in NDWI in the negative direction in the first two months of the year compared to other months which had fairly constant changing values. July to November also had gradual changes both towards the positive and negative direction. 2019, 2020 and 2021 however showcased a better trend with minimal rapid changes over short periods of time thereby giving a better insight of the changes over time. Like 2018, 2022 also showed rapid changes in the first 3 months of the year then later deteriorated to fairly constant values till the last two months of the year. However, because of the challenges and limitations associated with rapidly changing values on an index time series chart over a short period, the obtained results may not be accurately displayed or may be affected by outliers or noise in the data, which tends to distort the trend signal thereby affecting the accuracy and reliability of trend estimates that can be used to capture seasonal or annual variability in the indices.

Table 4.3 2018 and 2019 NDWI Mean Values

ACTUAL DAY OF THE YEAR	2018 NDWI MEAN VALUES	ACTUAL DAY OF THE YEAR	2018 NDWI MEAN VALUES	ACTUAL DAY OF THE YEAR	2019 NDWI MEAN VALUES	ACTUAL DAY OF THE YEAR	2019 NDWI MEAN VALUES
14	-0.174	**204**	-0.468	9	-0.297	224	-0.455
19	-0.197	**216**	-0.419	14	-0.429	229	-0.453
29	-0.437	**219**	-0.294	19	-0.304	234	-0.49
31	-0.412	**221**	-0.46	26	-0.353	236	-0.444
39	-0.427	**224**	-0.439	29	-0.414	239	-0.431
44	-0.511	**226**	-0.444	34	-0.388	241	-0.428
49	-0.521	**229**	-0.305	36	-0.336	244	-0.438
54	-0.508	**234**	-0.423	49	-0.378	246	-0.424
64	-0.285	**236**	-0.383	56	-0.349	249	-0.433
71	-0.31	**239**	-0.285	61	-0.353	254	-0.441
79	-0.443	**244**	-0.436	66	-0.411	256	-0.399
84	-0.378	**246**	-0.423	76	-0.401	259	-0.406
86	-0.395	**254**	-0.418	79	-0.401	261	-0.449
94	-0.417	**259**	-0.408	81	-0.403	264	-0.419
96	-0.394	**261**	-0.424	84	-0.456	266	-0.445
104	-0.526	**264**	-0.315	114	-0.51	271	-0.411
106	-0.428	**266**	-0.388	119	-0.408	274	-0.427
109	-0.439	**269**	-0.421	124	-0.452	286	-0.424
114	-0.434	**271**	-0.373	134	-0.456	291	-0.267
121	-0.409	**274**	-0.388	149	-0.501	296	-0.404
124	-0.435	**276**	-0.351	154	-0.469	299	-0.376
136	-0.499	**279**	-0.388	159	-0.472	304	-0.411
139	-0.474	**286**	-0.353	166	-0.467	306	-0.44
146	-0.498	**299**	-0.405	176	-0.449	309	-0.418
154	-0.529	**301**	-0.439	181	-0.467	311	-0.414
159	-0.502	**304**	-0.386	184	-0.466	314	-0.33
161	-0.481	**306**	-0.369	186	-0.435	316	-0.398
179	-0.472	**314**	-0.307	189	-0.444	321	-0.415
184	-0.424	**316**	-0.316	201	-0.429	324	-0.431
186	-0.47	**319**	-0.45	204	-0.464	336	-0.443
189	-0.435	**329**	-0.471	206	-0.437	341	-0.41
191	-0.452	**349**	-0.443	209	-0.467	351	-0.43
196	-0.442	**356**	-0.346	211	-0.425	354	-0.432
199	-0.464			219	-0.487		
				221	-0.45		

Table 4.4 2020, 2021 and 2022 NDWI Mean Values

ACTUAL DAY OF THE YEAR	2020 NDWI MEAN VALUES	ACTUAL DAY OF THE YEAR	2020 NDWI MEAN VALUES	ACTUAL DAY OF THE YEAR	2021 NDWI MEAN VALUES	ACTUAL DAY OF THE YEAR	2021 NDWI MEAN VALUES	ACTUAL DAY OF THE YEAR	2022 NDWI MEAN VALUES	ACTUAL DAY OF THE YEAR	2022 NDWI MEAN VALUES
1	-0.348	**219**	-0.458	**3**	-0.418	**215**	-0.429	**3**	-0.374	**213**	-0.266
9	-0.374	**221**	-0.437	**10**	-0.379	**218**	-0.425	**5**	-0.235	**215**	-0.261
11	-0.297	**224**	-0.429	**18**	-0.491	**220**	-0.449	**20**	-0.354	**218**	-0.26
14	-0.315	**226**	-0.435	**23**	-0.428	**223**	-0.451	**38**	-0.187	**220**	-0.266
16	-0.328	**229**	-0.459	**40**	-0.349	**225**	-0.457	**43**	-0.226	**225**	-0.264
21	-0.37	**231**	-0.434	**43**	-0.5	**228**	-0.446	**45**	-0.179	**228**	-0.231
24	-0.394	**234**	-0.33	**45**	-0.431	**230**	-0.422	**50**	-0.212	**230**	-0.265
56	-0.365	**236**	-0.433	**53**	-0.43	**233**	-0.436	**73**	-0.272	**235**	-0.233
61	-0.388	**239**	-0.438	**55**	-0.417	**235**	-0.417	**75**	-0.212	**240**	-0.284
64	-0.41	**241**	-0.417	**58**	-0.454	**238**	-0.424	**103**	-0.268	**243**	-0.254
71	-0.382	**244**	-0.429	**63**	-0.474	**240**	-0.41	**113**	-0.258	**245**	-0.251
74	-0.355	**249**	-0.425	**78**	-0.471	**243**	-0.392	**115**	-0.231	**248**	-0.263
81	-0.397	**251**	-0.416	**80**	-0.439	**248**	-0.427	**118**	-0.252	**250**	-0.284
104	-0.428	**254**	-0.421	**88**	-0.463	**250**	-0.406	**123**	-0.258	**253**	-0.268
109	-0.429	**256**	-0.33	**103**	-0.472	**253**	-0.377	**128**	-0.278	**255**	-0.253
111	-0.44	**259**	-0.422	**113**	-0.479	**255**	-0.426	**130**	-0.288	**258**	-0.266
119	-0.38	**261**	-0.404	**118**	-0.463	**258**	-0.462	**133**	-0.281	**260**	-0.262
131	-0.456	**264**	-0.376	**120**	-0.422	**260**	-0.433	**138**	-0.285	**263**	-0.239
134	-0.459	**266**	-0.4	**123**	-0.407	**263**	-0.421	**140**	-0.303	**268**	-0.27
136	-0.45	**271**	-0.384	**125**	-0.424	**268**	-0.436	**145**	-0.274	**270**	-0.266
139	-0.445	**274**	-0.397	**130**	-0.487	**270**	-0.394	**148**	-0.319	**273**	-0.248
141	-0.43	**279**	-0.429	**133**	-0.446	**273**	-0.421	**150**	-0.3	**275**	-0.254
144	-0.485	**281**	-0.391	**135**	-0.459	**275**	-0.41	**155**	-0.303	**278**	-0.252
146	-0.432	**286**	-0.411	**140**	-0.459	**278**	-0.42	**168**	-0.281	**283**	-0.25
149	-0.45	**289**	-0.395	**143**	-0.504	**280**	-0.418	**170**	-0.287	**295**	-0.248
159	-0.461	**291**	-0.399	**145**	-0.474	**283**	-0.41	**173**	-0.309	**298**	-0.249
161	-0.452	**296**	-0.397	**150**	-0.462	**285**	-0.403	**175**	-0.336	**300**	-0.246
166	-0.425	**299**	-0.422	**155**	-0.46	**288**	-0.416	**180**	-0.313	**303**	-0.241
174	-0.451	**301**	-0.396	**158**	-0.457	**293**	-0.427	**183**	-0.281	**305**	-0.248
176	-0.442	**304**	-0.422	**165**	-0.405	**295**	-0.414	**185**	-0.314	**308**	-0.239
179	-0.464	**311**	-0.345	**170**	-0.445	**298**	-0.398	**188**	-0.277	**310**	-0.248
181	-0.459	**314**	-0.407	**178**	-0.439	**300**	-0.368	**190**	-0.289	**315**	-0.232
184	-0.46	**316**	-0.397	**180**	-0.433	**303**	-0.353	**193**	-0.288	**318**	-0.239
186	-0.446	**319**	-0.383	**183**	-0.434	**308**	-0.425	**195**	-0.3	**323**	-0.212
191	-0.443	**321**	-0.409	**188**	-0.467	**310**	-0.411	**198**	-0.285	**330**	-0.235
194	-0.459	**324**	-0.399	**190**	-0.433	**315**	-0.435	**200**	-0.296	**338**	-0.128
196	-0.441	**329**	-0.456	**193**	-0.433	**320**	-0.411	**203**	-0.282	**343**	-0.226
199	-0.42	**334**	-0.43	**195**	-0.426	**335**	-0.412	**205**	-0.301	**350**	-0.216
201	-0.429	**339**	-0.425	**198**	-0.438	**340**	-0.347	**208**	-0.285	**353**	-0.244
204	-0.472	**341**	-0.435	**200**	-0.432	**343**	-0.471	**210**	-0.292	**363**	-0.23
206	-0.428	**344**	-0.448	**203**	-0.44	**345**	-0.419				
209	-0.442	**359**	-0.43	**205**	-0.43	**355**	-0.404				
211	-0.435	**361**	-0.405	**208**	-0.448	**358**	-0.473				
214	-0.441	**364**	-0.437	**210**	-0.44	**363**	-0.318				
216	-0.428			**213**	-0.447						

As illustrated in the time series chart for Table 4.3 and Table 4.4, the highest recorded NDWI mean value for 2018 was -0.174 on day 14, 14th January, 2018 and the lowest recorded NDWI mean value was -0.526 on day 104, 14th April, 2018. In contrast, the highest value for 2019 was -0.267 on day 291, 18th October, 2019 and lowest as -0.510 on day 114, 24th April, 2019. The year 2020 had a highest NDWI mean value of -0.297 on day 11, 11th January, 2020 and lowest value of -0.485 on day 144, 23rd May, 2020 while 2021 and 2022 had -0.318 on day 363, 29th December, 2021 and -0.128 on day 338, 4th December, 2022 as highest, respectively. In addition, the lowest obtained values were -0.504 on day 143, 23rd May, 2021 and -0.374 on day 3, 3rd January, 2022.

In summary, the highest NDWI mean value was obtained in 2022 as -0.128 and lowest mean value in 2018 as -0.526 over the study period. The areas with high NDWI values represented abundant water resources, such as lakes and rivers while low NDWI values represented areas with less or minimal water content such as bare land, rocks and soil.

4.1.3. NDSI Index

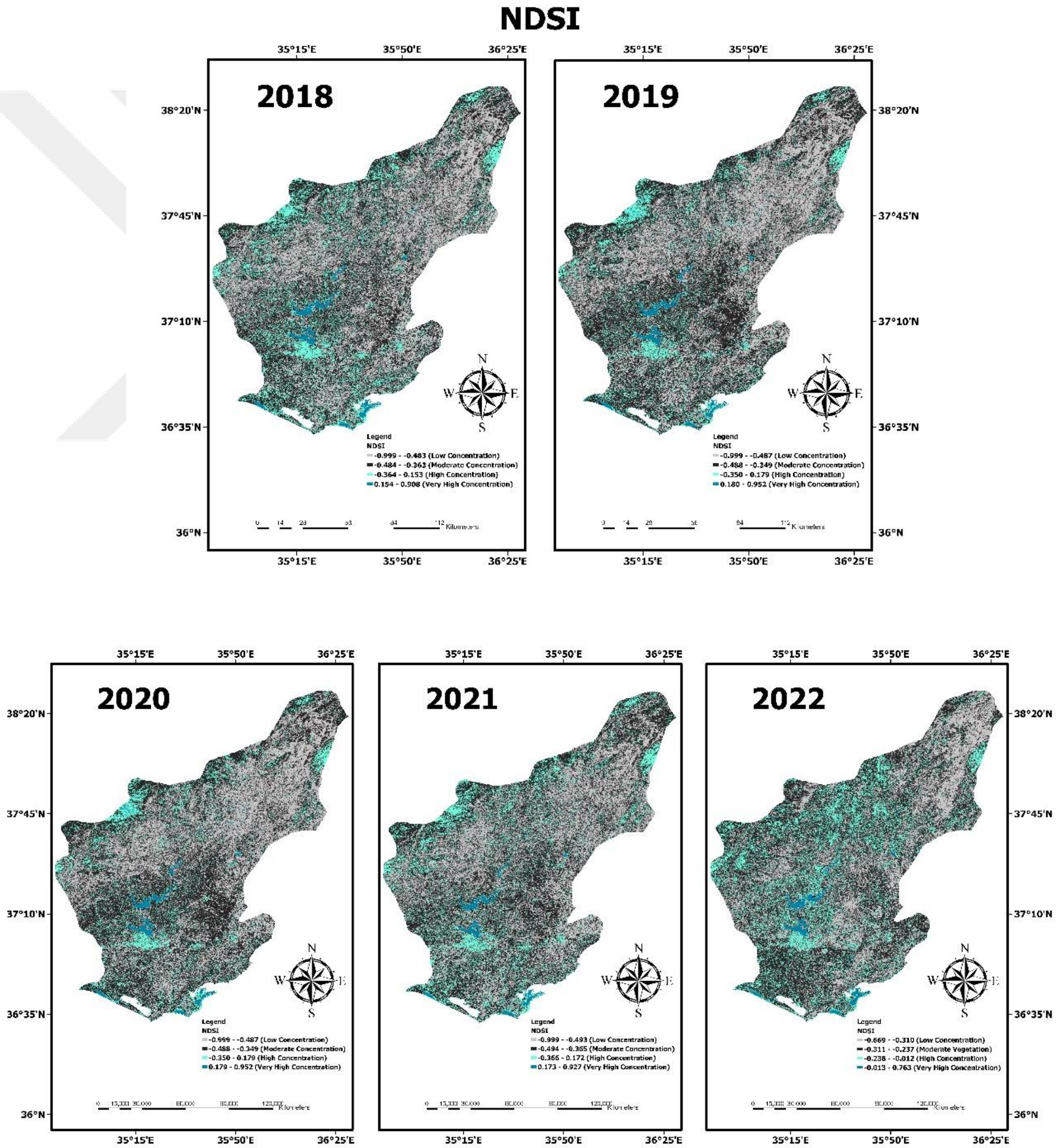

Figure 4.13 NDSI Maps for 2018, 2019, 2020, 2021 and 2022

In comparison to NDVI and NDWI, four ranges were set for NDSI as Low Concentration with the grey color, Medium Concentration with black color, High Concentration with light blue color and Very High Concentration with dark blue color. 2018 had a range of (-0.999 – -0.483) as Low Concentration and (-0.484 – - 0.363) as Moderate Concentration, (-0.364 – 0.153) as High Concentration and (0.154 – 0.908) as Very High Concentration. 2019 had ranges of (-0.999 – 0.487) as Low Concentration and (-0.488 – -0.349) as Moderate Concentration, (-0.350 – 0.179) as High Concentration and (0.180 – 0.952) as Very High Concentration. Furthermore, 2020 and 2021 had a value range of (-0.999 – -0.487) and (-0.999 – -0.493) as Low Concentration and (- 0.488 – -0.349) and (-0.494 – -0.365) as Moderate Concentration, similarly (-0.350 – 0.179) and (-0.366 – 0.172) as High Concentration and finally (0.179 – 0.952) and (0.173 – 0.927) as Very High Concentration. The last was 2022 with (-0.669 – -0.310) as Low Concentration, (-0.311 – -0.237) as Moderate Concentration, (-0.238 – -0.012) as High Concentration and lastly (-0.013 – 0.763) as Very High Concentration.

However, as closely observed on the NDSI maps on Figure 4.13, a high concentration of NDSI was observed in water bodies, built areas and mountainous regions sitting on high altitudes which can lead to potential misleading interpretations. It is clear that the mentioned areas had spectral properties similar to areas prone with snow or ice upon calculation. As Adana is not a region prone to snow cover, using NDSI to solely detect snow cover might not yield accurate results due to index's sensitivity to both snow/ice and water bodies which arise from the sensitivity from similar spectral properties of snow/ice and water as it is calculated by leveraging the differences in reflectance between visible and near infrared. Snow and ice exhibits high reflectance in the visible spectrum and low reflectance in the near-infrared spectrum. Conversely, water bodies can also generate relatively high NDSI values due to their reflective properties in these spectral bands, which can lead to false positives in snow detection, especially in areas were snow cover is minimal like our study area.

To map NDSI for representation in ArcGIS Pro, the interval was set from -1 to 1 with the majority results being negative as shown in Table 4.5 and Table 4.6 which had 0.099 as the highest NDSI mean value obtained indicating less snow cover or a false positive from the water bodies or less areas associated with snow. As similar to the calculation of other indices which involved the utilization of a collection of images to extract the index. Each image had a different index mean value that was obtained for the study period to give a clear distinction of the changes in the trend.

Considering the limitations of NDSI in areas with infrequent snow cover, exploring alternative remote sensing techniques or models designed specifically for snow detection in varying climatic conditions could offer more reliable results for analyzing snow. Utilizing additional data sources such as thermal bands or historical snow cover data could also improve the precision of snow identification. Other vital useful methods such as conducting the study over a longer period to capture seasonal changes and variations in snow cover and implementing advanced machine learning algorithms as models trained on diverse datasets that learn complex patterns beyond simple spectral indices and factors influencing snow detection would also be a better way to fully analyze snow cover for the intended study.

However, to give an understanding of the obtained results in relation to NDSI for the interval of 2018 to 2022, the 2018 map as shown on Figure 4.13, had areas such as the Lower Southern Central parts with a High Concentration of NDSI, water bodies depicted a Very High Concentration while mountainous regions in the Western and Northern parts also showed High Concentration of NDSI, Areas such as Croplands and Trees were in the Lowest and Medium category as observed hence validating the true results for an NDSI index in a given area of study, Furthermore, 2019, 2020 and 2021 also depicted similar visual properties as 2018 but with more areas of Very High Concentration in dark blue as compared to 2018. In 2022, however, saw an increase in regions with High Concentration in Light Blue color in Northern and Western parts of the study area. Additionally, more Low Concentration areas visualized in grey color were also observed in the Northern and Eastern regions of the map.

Figure 4.14 to Figure 4.18 below show the time series analysis charts from the period of 2018 to 2022. Most values showed negative values with minimal positive values showing on months related with winter in the study area. Figure 4.14 shows the NDSI Time Series Chart in 2018, it was observed that high values of NDSI in the first three months with multiple fluctuations both in the positive and negative direction were present. However, after the third month a steady trend in the values was observed with lower values towards the months associated with summer. In 2019, as shown in Figure 4.15, also showed higher values in the first two months with a steep and drastic change in the first month. The first month showed the highest values as shown in Table 4.5 while months associated with summer also showed lower values during that period with lowest values recorded in August. 2020, like 2018 and 2019 also showed higher values in the first two months with the highest as shown on Figure 4.16 been in January while a steady trend was also observed in the months associated with summer with the lowest values as shown in Table 4.6. Finally, 2021 and 2022 showed a similar time series chart. The months from January to March showed a higher peak value of NDSI with multiple fluctuations both in the Negative and Positive direction as shown on Figure 4.17 and Figure 4.18. Furthermore, May to November showed a steady trend in low values of NDSI, hence validating the information that states lower values are obtained during the summer periods as discussed earlier.

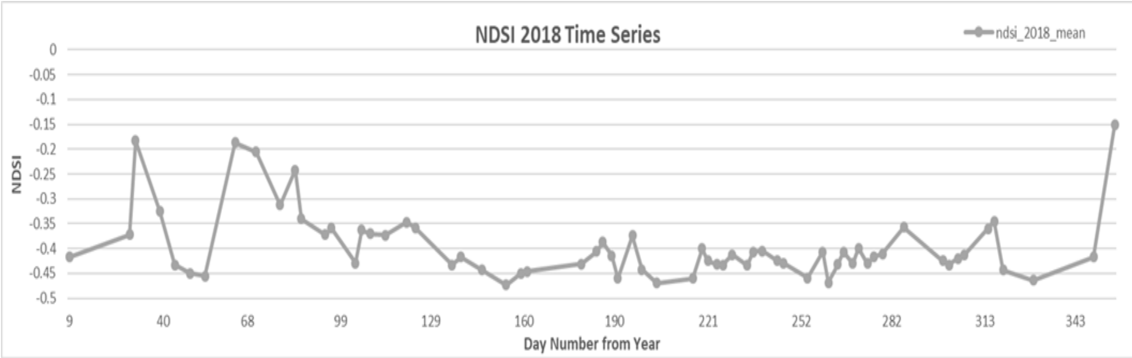

Figure 4.14 2018 NDSI Time Series

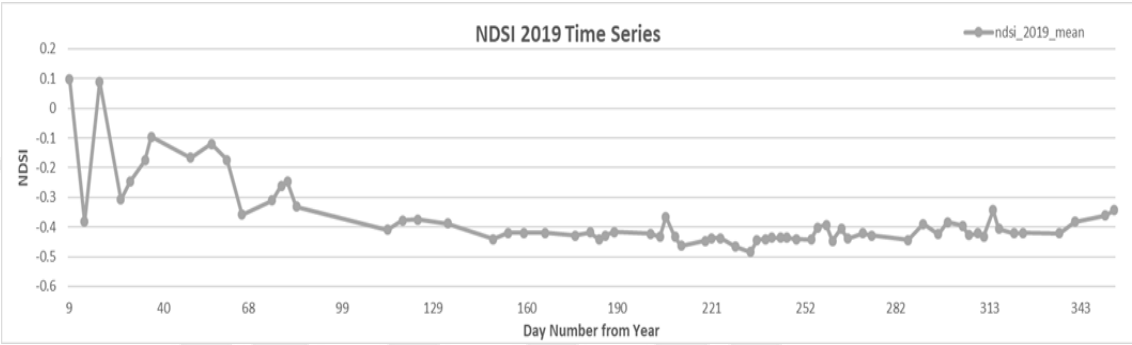

Figure 4.15 2019 NDSI Time Series

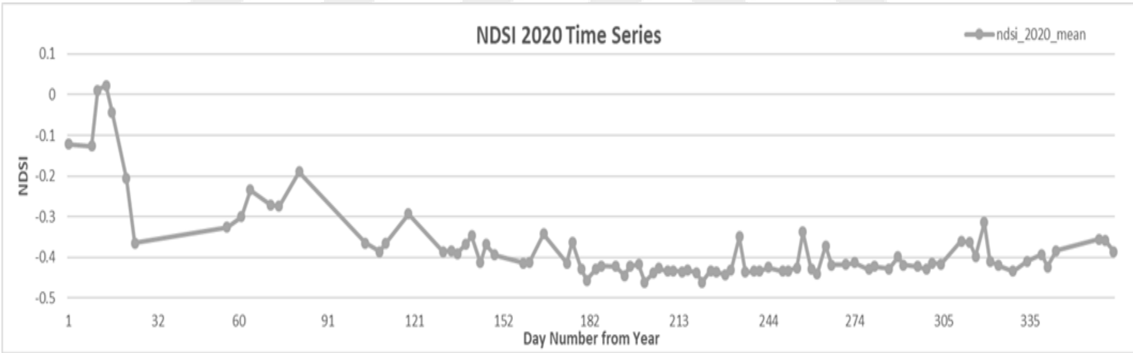

Figure 4.16 2020 NDSI Time Series

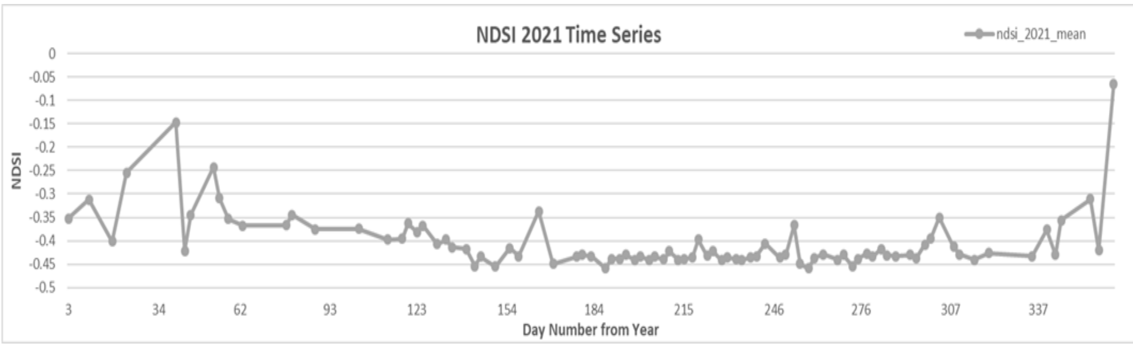

Figure 4.17 2021 NDSI Time Series

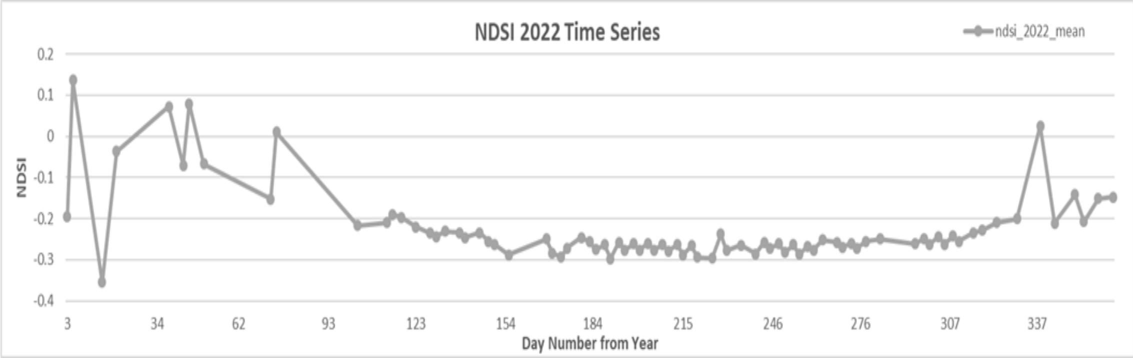

Figure 4.18 2022 NDSI Time Series

In line with NDVI and NDWI information, the highest recorded NDSI mean value in 2018 was -0.151 on day 356, 22nd December, 2018 and lowest was -0.473 on day 154, 23rd, June, 2018. 2019 had recorded values of 0.099 on day 9, 9th January, 2019 as highest and -0.484 on day 234, 22nd August, 2019 as the lowest in Table 4.5 as illustrated while 2020 had 0.023 on day 14, 14th January, 2020 as the highest and -0.462 on day 221, 8th August, 2020 as the lowest. Contrary, 2021 had high values of -0.065 on day 363, 29th December, 2021 and low value of -0.459 on two respective days 188 and 258, July 7th and September 9th, 2021. Lastly, 2022 recorded NDSI mean values of 0.137 on 5th January, 2022 as highest and -0.355 as lowest on day 15 in Table 4.6 as shown.

The highest values obtained over the study period was in 2019 as 0.099 and lowest as -0.484 in 2019, respectively. As the study region is not really prone to high snow fall, areas that showed high values in NDSI represented mountainous regions and high attitude areas. Conversely, areas that showed low NDSI values represented minimal or no snow cover as stipulated in the study region.

Table 4.5 2018 and 2019 NDSI Mean Values

ACTUAL DAY OF THE YEAR	2018 NDSI MEAN VALUES	ACTUAL DAY OF THE YEAR	2018 NDSI MEAN VALUES	ACTUAL DAY OF THE YEAR	2019 NDSI MEAN VALUES	ACTUAL DAY OF THE YEAR	2019 NDSI MEAN VALUES
9	-0.417	**204**	-0.469	**9**	0.099	**224**	-0.438
29	-0.372	**216**	-0.46	**14**	-0.382	**229**	-0.466
31	-0.183	**219**	-0.4	**19**	0.089	**234**	-0.484
39	-0.324	**221**	-0.424	**26**	-0.308	**236**	-0.443
44	-0.433	**224**	-0.432	**29**	-0.248	**239**	-0.441
49	-0.45	**226**	-0.433	**34**	-0.175	**241**	-0.436
54	-0.455	**229**	-0.412	**36**	-0.096	**244**	-0.436
64	-0.187	**234**	-0.434	**49**	-0.166	**246**	-0.436
71	-0.205	**236**	-0.407	**56**	-0.121	**249**	-0.441
79	-0.312	**239**	-0.405	**61**	-0.174	**254**	-0.442
84	-0.242	**244**	-0.424	**66**	-0.359	**256**	-0.402
86	-0.34	**246**	-0.429	**76**	-0.31	**259**	-0.393
94	-0.372	**254**	-0.459	**79**	-0.261	**261**	-0.446
96	-0.359	**259**	-0.407	**81**	-0.248	**264**	-0.405
104	-0.429	**261**	-0.468	**84**	-0.331	**266**	-0.439
106	-0.363	**264**	-0.432	**114**	-0.409	**271**	-0.421
109	-0.37	**266**	-0.407	**119**	-0.378	**274**	-0.429
114	-0.373	**269**	-0.43	**124**	-0.375	**286**	-0.443
121	-0.347	**271**	-0.399	**134**	-0.389	**291**	-0.39
124	-0.359	**274**	-0.43	**149**	-0.44	**296**	-0.424
136	-0.433	**276**	-0.417	**154**	-0.42	**299**	-0.384
139	-0.417	**279**	-0.41	**159**	-0.42	**304**	-0.396
146	-0.443	**286**	-0.357	**166**	-0.42	**306**	-0.427
154	-0.473	**299**	-0.424	**176**	-0.428	**309**	-0.422
159	-0.45	**301**	-0.433	**181**	-0.419	**311**	-0.431
161	-0.446	**304**	-0.42	**184**	-0.442	**314**	-0.344
179	-0.431	**306**	-0.413	**186**	-0.428	**316**	-0.406
184	-0.406	**314**	-0.36	**189**	-0.417	**321**	-0.421
186	-0.387	**316**	-0.345	**201**	-0.423	**324**	-0.42
189	-0.414	**319**	-0.443	**204**	-0.433	**336**	-0.421
191	-0.46	**329**	-0.464	**206**	-0.366	**341**	-0.382
196	-0.374	**349**	-0.417	**209**	-0.433	**351**	-0.362
199	-0.442	**356**	-0.151	**211**	-0.463	**354**	-0.344
				219	-0.446		
				221	-0.438		

Table 4.6 2020, 2021 and 2022 NDSI Mean Values

ACTUAL DAY OF THE YEAR	2020 NDSI MEAN VALUES	ACTUAL DAY OF THE YEAR	2020 NDSI MEAN VALUES	ACTUAL DAY OF THE YEAR	2021 NDSI MEAN VALUES	ACTUAL DAY OF THE YEAR	2021 NDSI MEAN VALUES	ACTUAL DAY OF THE YEAR	2022 NDSI MEAN VALUES	ACTUAL DAY OF THE YEAR	2022 NDSI MEAN VALUES
1	-0.122	**219**	-0.438	**3**	-0.352	**215**	-0.44	**3**	-0.196	**213**	-0.264
9	-0.126	**221**	-0.462	**10**	-0.312	**218**	-0.435	**5**	0.137	**215**	-0.288
11	0.011	**224**	-0.433	**18**	-0.401	**220**	-0.397	**15**	-0.355	**218**	-0.266
14	0.023	**226**	-0.437	**23**	-0.255	**223**	-0.432	**20**	-0.037	**220**	-0.294
16	-0.043	**229**	-0.443	**40**	-0.147	**225**	-0.422	**38**	0.072	**225**	-0.296
21	-0.206	**231**	-0.432	**43**	-0.421	**228**	-0.442	**43**	-0.071	**228**	-0.238
24	-0.365	**234**	-0.35	**45**	-0.345	**230**	-0.436	**45**	0.079	**230**	-0.278
56	-0.326	**236**	-0.437	**53**	-0.243	**233**	-0.439	**50**	-0.067	**235**	-0.265
61	-0.301	**239**	-0.435	**55**	-0.309	**235**	-0.442	**73**	-0.152	**240**	-0.286
64	-0.235	**241**	-0.434	**58**	-0.353	**238**	-0.435	**75**	0.01	**243**	-0.258
71	-0.271	**244**	-0.425	**63**	-0.368	**240**	-0.433	**103**	-0.217	**245**	-0.272
74	-0.275	**249**	-0.434	**78**	-0.367	**243**	-0.406	**113**	-0.21	**248**	-0.261
81	-0.19	**251**	-0.433	**80**	-0.345	**248**	-0.436	**115**	-0.19	**250**	-0.282
104	-0.365	**254**	-0.426	**88**	-0.375	**250**	-0.43	**118**	-0.197	**253**	-0.264
109	-0.386	**256**	-0.338	**103**	-0.374	**253**	-0.367	**123**	-0.22	**255**	-0.287
111	-0.366	**259**	-0.43	**113**	-0.397	**255**	-0.449	**128**	-0.235	**258**	-0.267
119	-0.294	**261**	-0.44	**118**	-0.396	**258**	-0.459	**130**	-0.244	**260**	-0.277
131	-0.386	**264**	-0.372	**120**	-0.363	**260**	-0.437	**133**	-0.231	**263**	-0.252
134	-0.384	**266**	-0.419	**123**	-0.381	**263**	-0.429	**138**	-0.234	**268**	-0.258
136	-0.391	**271**	-0.418	**125**	-0.368	**268**	-0.441	**140**	-0.246	**270**	-0.269
139	-0.368	**274**	-0.413	**130**	-0.407	**270**	-0.43	**145**	-0.234	**273**	-0.26
141	-0.348	**279**	-0.43	**133**	-0.397	**273**	-0.454	**148**	-0.256	**275**	-0.272
144	-0.413	**281**	-0.423	**135**	-0.414	**275**	-0.439	**150**	-0.263	**278**	-0.255
146	-0.369	**286**	-0.429	**140**	-0.418	**278**	-0.427	**155**	-0.288	**283**	-0.25
149	-0.394	**289**	-0.399	**143**	-0.454	**280**	-0.434	**168**	-0.25	**295**	-0.261
159	-0.415	**291**	-0.419	**145**	-0.434	**283**	-0.418	**170**	-0.283	**298**	-0.248
161	-0.413	**296**	-0.423	**150**	-0.455	**285**	-0.431	**173**	-0.294	**300**	-0.263
166	-0.343	**299**	-0.43	**155**	-0.416	**288**	-0.433	**175**	-0.272	**303**	-0.244
174	-0.415	**301**	-0.415	**158**	-0.433	**293**	-0.43	**180**	-0.246	**305**	-0.262
176	-0.363	**304**	-0.417	**165**	-0.337	**295**	-0.438	**183**	-0.257	**308**	-0.243
179	-0.429	**311**	-0.361	**170**	-0.449	**298**	-0.408	**185**	-0.275	**310**	-0.256
181	-0.457	**314**	-0.364	**178**	-0.434	**300**	-0.395	**188**	-0.264	**315**	-0.234
184	-0.43	**316**	-0.398	**180**	-0.43	**303**	-0.35	**190**	-0.298	**318**	-0.229
186	-0.421	**319**	-0.314	**183**	-0.433	**308**	-0.413	**193**	-0.258	**323**	-0.21
191	-0.423	**321**	-0.41	**188**	-0.459	**310**	-0.429	**195**	-0.277	**330**	-0.201
194	-0.445	**324**	-0.42	**190**	-0.439	**315**	-0.441	**198**	-0.261	**338**	0.025
196	-0.421	**329**	-0.435	**193**	-0.439	**320**	-0.426	**200**	-0.276	**343**	-0.211
199	-0.418	**334**	-0.41	**195**	-0.43	**335**	-0.433	**203**	-0.26	**350**	-0.142
201	-0.461	**339**	-0.393	**198**	-0.441	**340**	-0.376	**205**	-0.276	**353**	-0.208
204	-0.439	**341**	-0.424	**200**	-0.433	**343**	-0.43	**208**	-0.264	**358**	-0.151
206	-0.428	**344**	-0.384	**203**	-0.442	**345**	-0.356	**210**	-0.279	**363**	-0.148
209	-0.434	**359**	-0.356	**205**	-0.434	**355**	-0.311				
211	-0.433	**361**	-0.358	**208**	-0.44	**358**	-0.42				
214	-0.436	**364**	-0.386	**210**	-0.422	**363**	-0.065				
216	-0.432			**213**	-0.441						

4.1.4. NDBI Index

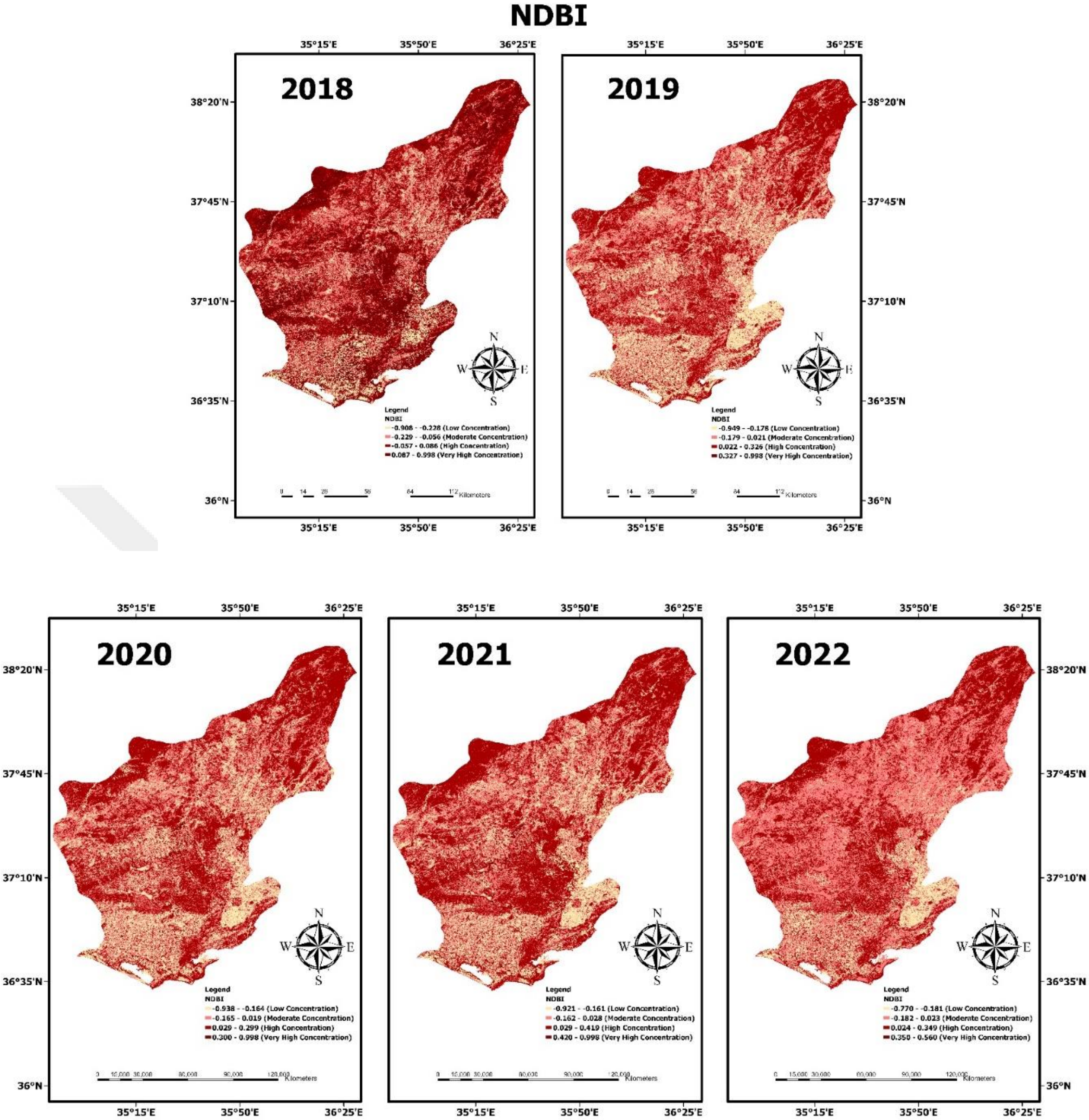

Figure 4.19 NDBI Maps for 2018, 2019, 2020, 2021 and 2022

In conclusion, the last obtained value ranges are shown in Figure 4.19 for NDBI over the 5-year study period. The intervals were set as Low Concentration shown in white color, Moderate Concentration shown in light pink, High Concentration illustrated as red color and Very High Concentration shown as dark red color. 2018 recorded a range value of (-0.908 - -0.228) Low Concentration, (-0.229 – -0.056) Moderate Concentration, (-0.057 – 0.086) High Concentration and lastly (0.087 – 0.998) as Very High Concentration. 2019 had a value range of (-0.949 - -0.178) Low Concentration, (-0.179 – 0.021) Moderate Concentration, (0.022 – 0.326) as High Concentration and (0.327 – 0.998) as Very High Concentration. 2020 had a range value of (-0.938 - -0.164) Low Concentration, (-0.165 – 0.019) Moderate Concentration, (0.029 – 0.299) High Concentration and

(0.300 – 0.998) as Very High Concentration. 2021 had a range value of (-0.921 - -0.161) Low Concentration, (-0.162 - 0.028) Moderate Concentration, (0.029 – 0.419) High Concentration and (0.420 – 0.998) as Very High Concentration. To sum it up, the last recorded range values for NDBI in 2022 were (-0.770 - -0.181) Low Concentration, (-0.182 - 0.023) Moderate Concentration, (0.024 – 0.349) High Concentration and (0.350 – 0.560) as Very High Concentration.

However, as can be closely observed in the NDBI maps above in Figure 4.19 and in comparison, to ground truth data which can be referenced for 2022 in Figure 4.43, it clearly illustrates that most of the lower middle part of the study area to have a high density of built-up areas hence the high NDBI values as depicted in red color. However, other regions such as Rangelands also depicted a high value of NDBI as can be seen in the Northern and Western parts of the Maps shown in Figure 4.19 causing a slight visual confusion. Reasons were attributed to factors such as exhibiting spectral properties similar to built-up or urban areas that occur if certain features within the related areas, such as bare soil patches, infrastructure or land and structures related to agriculture or livestock and even temporary settlements show spectral properties similar to urban surfaces as can be observed on the referenced ground truth data imagery. If the classes show the same visual details and pixels as in our case the algorithm classifies them as Built Area. Furthermore, index sensitivity may also have affected land cover features or conditions that lead to higher values in non-urban areas.

As can be observed from NDBI time series charts from Figure 4.20 to Figure 4.24 peak values are seen during the summer period of June to October indicating a high density of built up structures, such as buildings and roads. This is logical in the essence that most of the urban activities, construction projects or expansion tend to occur during the summer periods hence illustrating higher NDBI values. Additionally, summer periods have reduced vegetation cover which tends to highlight the built-up areas dominance in the landscape as can be seen in environments during summer. Changes in vegetation and water bodies might reduce too due to higher temperatures and less rainfall, thereby exposing more built-up surfaces. This decrease can also lead to higher NDBI values as built areas become more prominent compared to vegetation. Furthermore, the changes in sunlight angles and shadows during summer can also influence the spectral response of built-up areas and cause variations in NDBI values too. In addition, as our study imagery was obtained in summer to get a clear visualization of the area with no to less clouds, bare ground, mountainous regions and rangeland were easily reflected by sunlight and showed similar visual properties with the actual built areas as also seen on Figure 4.43 hence causing a confusion in NDBI.

Figure 4.20 shows the NDBI Time Series Chart for 2018, the time series was conducted over a yearly period as the other indices. The lowest NDBI values were recorded in months associated with winter in the study area and the highest values in summer as shown on the Figure. Table 4.7, highlights the values obtained and gives more detailed information about the change in index value. Furthermore, to obtain a clear smooth time series chart, all the outliers and values that showed abnormal figures were filtered out as they could have been affected by discrepancies discussed earlier in the other indices.

The 2019 NDBI Time Series as shown in Figure 4.21, showed a similar trend and pattern over the year as compared to 2018. The lowest values as seen on the chart were also observed in months associated with winter such as January and December, while the highest was observed in October a month also associated with summer. Table 4.7, explains in details the values obtained including the highest and lowest.

Furthermore, the 2020 NDBI Time Series as observed on Figure 4.22 showed a slightly different trend in the first quarter of the year from showing the lowest values to portraying the highest over a short period of time. A constant range was also observed in the months of February till March. In addition, like 2018 and 2019 the peak values were also observed towards months associated with summer as shown in Table 4.8.

When compared to 2020, 2021 as shown in Figure 4.23 showed a more stepper change towards the negative in the first month associated with winter hence showcasing lower values of NDBI. The lowest value was obtained in February as shown in Table 4.8 while the highest values were observed in months associated with summer such as September. The trend however was fairly constant from June till September indicating high values of NDBI.

To summarize it, the last obtained time series chart was for 2022 shown in Figure 4.24 which also saw similar changes in the first quarter of the year in months associated with winter. The NDBI values dropped drastically from mid-January towards early February and saw an increase from February towards the summer months of the study area. A steady trend was later observed during months associated with summer including the highest NDBI values obtained.

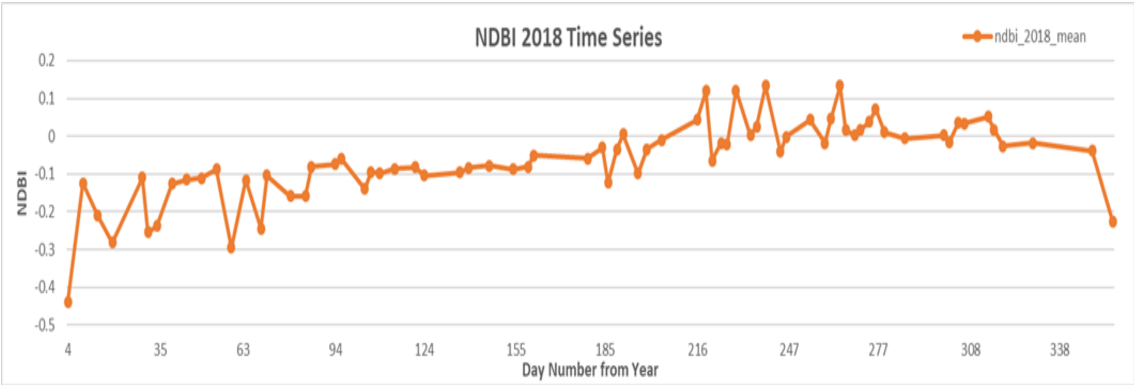

Figure 4.20 2018 NDBI Time Series

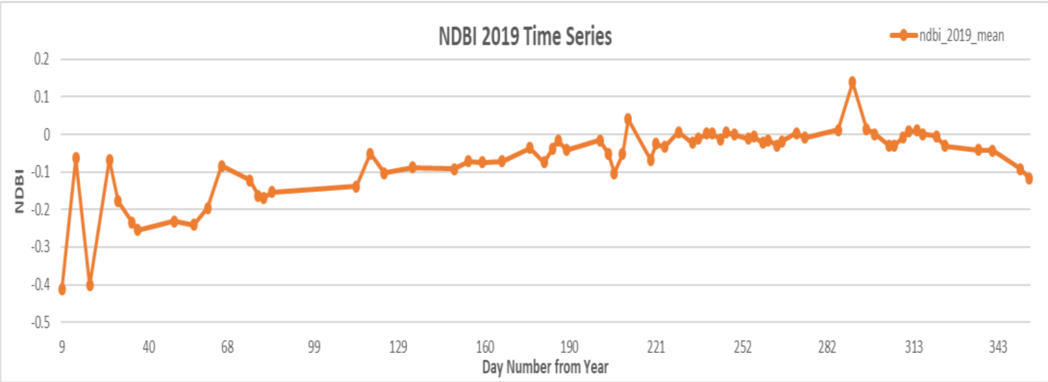

Figure 4.21 2019 NDBI Time Series

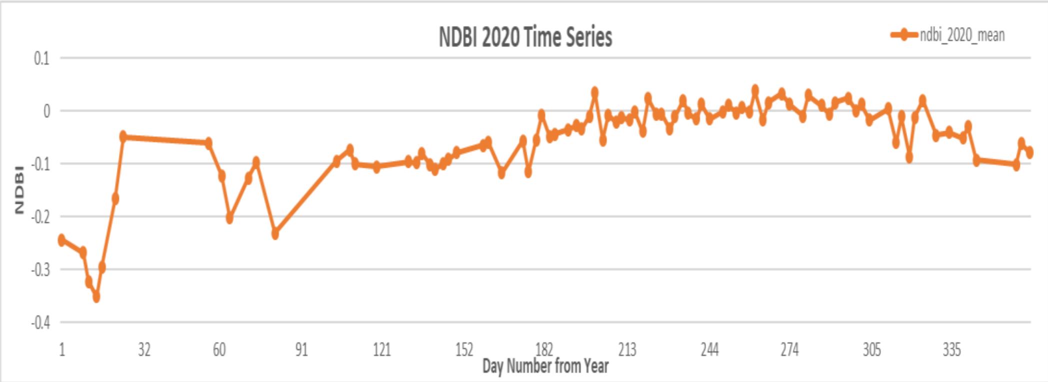

Figure 4.22 2020 NDBI Time Series

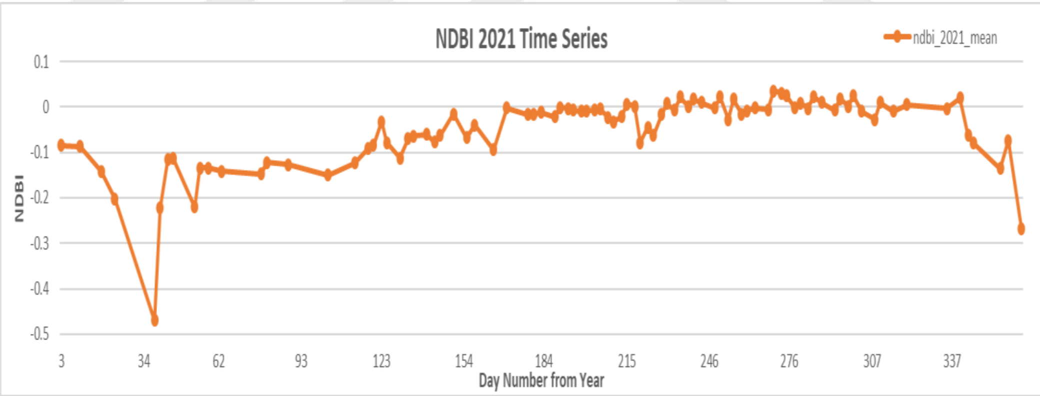

Figure 4.23 2021 NDBI Time Series

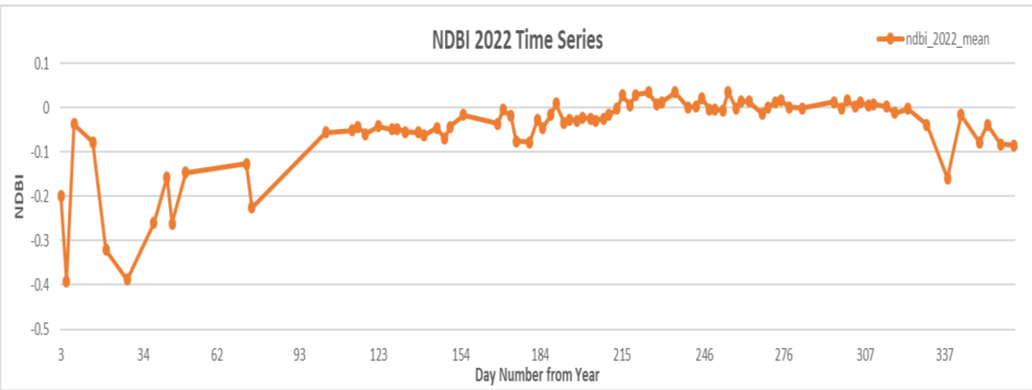

Figure 4.24 2022 NDBI Time Series

Table 4.7 2018 and 2019 NDBI Mean Values

ACTUAL DAY OF THE YEAR	2018 NDBI MEAN VALUES	ACTUAL DAY OF THE YEAR	2018 NDBI MEAN VALUES	ACTUAL DAY OF THE YEAR	2019 NDBI MEAN VALUES	ACTUAL DAY OF THE YEAR	2019 NDBI MEAN VALUES
4	-0.438	**196**	-0.098	**9**	-0.413	**221**	-0.025
9	-0.124	**199**	-0.035	**14**	-0.063	**224**	-0.034
14	-0.211	**204**	-0.01	**19**	-0.402	**229**	0.006
19	-0.281	**216**	0.044	**26**	-0.067	**234**	-0.022
29	-0.11	**219**	0.12	**29**	-0.178	**236**	-0.011
31	-0.254	**221**	-0.065	**34**	-0.234	**239**	0.002
34	-0.238	**224**	-0.018	**36**	-0.255	**241**	0.002
39	-0.126	**226**	-0.022	**49**	-0.231	**244**	-0.013
44	-0.115	**229**	0.121	**56**	-0.241	**246**	0.005
49	-0.111	**234**	0.003	**61**	-0.196	**249**	-0.001
54	-0.087	**236**	0.026	**66**	-0.084	**254**	-0.011
59	-0.295	**239**	0.134	**76**	-0.122	**256**	-0.006
64	-0.116	**244**	-0.041	**79**	-0.163	**259**	-0.023
69	-0.245	**246**	-0.002	**81**	-0.169	**261**	-0.015
71	-0.104	**254**	0.043	**84**	-0.154	**264**	-0.03
79	-0.158	**259**	-0.018	**114**	-0.139	**266**	-0.018
84	-0.159	**261**	0.047	**119**	-0.051	**271**	0.003
86	-0.081	**264**	0.134	**124**	-0.103	**274**	-0.009
94	-0.074	**266**	0.018	**134**	-0.088	**286**	0.011
96	-0.059	**269**	0.003	**149**	-0.092	**291**	0.138
104	-0.14	**271**	0.018	**154**	-0.072	**296**	0.014
106	-0.095	**274**	0.038	**159**	-0.074	**299**	0.001
109	-0.098	**276**	0.072	**166**	-0.071	**304**	-0.03
114	-0.086	**279**	0.011	**176**	-0.036	**306**	-0.03
121	-0.082	**286**	-0.006	**181**	-0.075	**309**	-0.009
124	-0.104	**299**	0.002	**184**	-0.039	**311**	0.007
136	-0.096	**301**	-0.016	**186**	-0.016	**314**	0.01
139	-0.083	**304**	0.036	**189**	-0.042	**316**	0.001
146	-0.078	**306**	0.034	**201**	-0.016	**321**	-0.005
154	-0.088	**314**	0.052	**204**	-0.053	**324**	-0.031
159	-0.081	**316**	0.018	**206**	-0.103	**336**	-0.042
161	-0.051	**319**	-0.026	**209**	-0.053	**341**	-0.043
179	-0.059	**329**	-0.018	**211**	0.04	**351**	-0.092
184	-0.03	**349**	-0.039	**219**	-0.068	**354**	-0.117
186	-0.123	**356**	-0.226				
189	-0.034						
191	0.005						

Table 4.8 2020, 2021 and 2022 NDBI Mean Values

ACTUAL DAY OF THE YEAR	2020 NDBI MEAN VALUES	ACTUAL DAY OF THE YEAR	2020 NDBI MEAN VALUES	ACTUAL DAY OF THE YEAR	2021 NDBI MEAN VALUES	ACTUAL DAY OF THE YEAR	2021 NDBI MEAN VALUES	ACTUAL DAY OF THE YEAR	2022 NDBI MEAN VALUES	ACTUAL DAY OF THE YEAR	2022 NDBI MEAN VALUES
1	-0.244	**219**	-0.038	**3**	-0.084	**215**	0.006	**3**	-0.2	**213**	-0.003
9	-0.268	**221**	0.023	**10**	-0.087	**218**	0.002	**5**	-0.391	**215**	0.028
11	-0.323	**224**	-0.006	**18**	-0.141	**220**	-0.078	**8**	-0.037	**218**	0.005
14	-0.352	**226**	-0.005	**23**	-0.202	**223**	-0.044	**15**	-0.078	**220**	0.029
16	-0.295	**229**	-0.034	**38**	-0.469	**225**	-0.063	**20**	-0.32	**225**	0.034
21	-0.166	**231**	-0.011	**40**	-0.222	**228**	-0.017	**28**	-0.388	**228**	0.008
24	-0.049	**234**	0.02	**43**	-0.116	**230**	0.008	**38**	-0.26	**230**	0.012
56	-0.061	**236**	-0.004	**45**	-0.113	**233**	-0.007	**43**	-0.157	**235**	0.034
61	-0.123	**239**	-0.015	**53**	-0.22	**235**	0.022	**45**	-0.261	**243**	0.003
64	-0.202	**241**	0.013	**55**	-0.134	**238**	0.001	**50**	-0.147	**245**	0.022
71	-0.127	**244**	-0.015	**58**	-0.134	**240**	0.017	**73**	-0.127	**248**	-0.004
74	-0.097	**249**	-0.001	**63**	-0.142	**243**	0.01	**75**	-0.225	**250**	-0.005
81	-0.231	**251**	0.011	**78**	-0.148	**248**	-0.002	**103**	-0.056	**253**	-0.006
104	-0.095	**254**	-0.003	**80**	-0.122	**250**	0.022	**113**	-0.051	**255**	0.036
109	-0.074	**256**	0.007	**88**	-0.127	**253**	-0.027	**115**	-0.043	**258**	-0.001
111	-0.1	**259**	-0.002	**103**	-0.15	**255**	0.017	**118**	-0.06	**260**	0.015
119	-0.106	**261**	0.038	**113**	-0.123	**258**	-0.016	**123**	-0.042	**263**	0.014
131	-0.096	**264**	-0.017	**118**	-0.092	**260**	-0.008	**128**	-0.049	**268**	-0.014
134	-0.098	**266**	0.016	**120**	-0.084	**263**	-0.002	**130**	-0.048	**270**	0.001
136	-0.08	**271**	0.033	**123**	-0.033	**268**	-0.006	**133**	-0.055	**273**	0.011
139	-0.101	**274**	0.013	**125**	-0.079	**270**	0.035	**138**	-0.056	**275**	0.017
141	-0.11	**279**	-0.01	**130**	-0.112	**273**	0.03	**140**	-0.063	**278**	0.001
144	-0.1	**281**	0.03	**133**	-0.07	**275**	0.024	**145**	-0.046	**283**	-0.001
146	-0.092	**286**	0.011	**135**	-0.064	**278**	-0.002	**148**	-0.07	**295**	0.013
149	-0.079	**289**	-0.006	**140**	-0.06	**280**	0.009	**150**	-0.043	**298**	-0.003
159	-0.065	**291**	0.016	**143**	-0.077	**283**	-0.003	**155**	-0.017	**300**	0.017
161	-0.06	**296**	0.024	**145**	-0.063	**285**	0.023	**168**	-0.036	**303**	0.002
166	-0.117	**301**	0.013	**150**	-0.016	**288**	0.01	**170**	-0.005	**305**	0.013
174	-0.056	**304**	-0.017	**155**	-0.068	**293**	-0.007	**173**	-0.019	**308**	0.004
176	-0.115	**311**	0.004	**158**	-0.04	**295**	0.018	**175**	-0.076	**310**	0.008
179	-0.054	**314**	-0.06	**165**	-0.094	**298**	0.001	**180**	-0.078	**315**	0.002
181	-0.008	**316**	-0.011	**170**	-0.002	**300**	0.024	**183**	-0.028	**318**	-0.012
184	-0.048	**319**	-0.086	**178**	-0.017	**303**	-0.009	**185**	-0.046	**323**	-0.003
186	-0.044	**321**	-0.012	**180**	-0.015	**308**	-0.028	**188**	-0.016	**330**	-0.039
191	-0.035	**324**	0.02	**183**	-0.012	**310**	0.01	**190**	0.009	**338**	-0.159
194	-0.028	**329**	-0.046	**188**	-0.022	**315**	-0.009	**193**	-0.034	**343**	-0.017
196	-0.034	**334**	-0.041	**190**	-0.001	**320**	0.005	**195**	-0.028	**350**	-0.078
199	-0.01	**339**	-0.051	**193**	-0.003	**335**	-0.003	**198**	-0.029	**353**	-0.039
201	0.034	**341**	-0.03	**195**	-0.007	**340**	0.02	**200**	-0.024	**358**	-0.083
204	-0.054	**344**	-0.093	**198**	-0.009	**343**	-0.063	**203**	-0.025	**363**	-0.085
206	-0.008	**359**	-0.101	**200**	-0.008	**345**	-0.08	**205**	-0.029		
209	-0.021	**361**	-0.061	**203**	-0.007	**355**	-0.135	**208**	-0.025		
211	-0.012	**364**	-0.079	**205**	-0.005	**358**	-0.073	**210**	-0.017		
214	-0.017			**208**	-0.023	**363**	-0.268				
216	-0.002			**210**	-0.032						
				213	-0.021						

Furthermore, the highest NDBI value for 2018 was 0.134 recorded on two separate days on day 239 and day 264 as 27th August and 21st September, 2018 and lowest as -0.438 on day 4, 4th January, 2018. 2019 had values of 0.138 on day 291, 18th October, 2019 as highest and -0.413 on day 9 as the lowest. 2020 had highest values of 0.034 on day 201, July 19th, 2020 and 0.035 on day 270, 27th September, 2021, respectively. The lowest values recorded were -0.352 on day 14, 14th January, 2021 and -0.469 on day 38, 7th February, 2021. Additionally, 2022 had 0.036 on day 255, 12th September, 2022 as the highest and -0.391 on day 5, 5th January, 2022 as the lowest.

The highest value obtained for the study period as shown in Table 4.7 was in 2019 as 0.138 and lowest in 2021 as -0.469. Areas with high values of NDBI represented densely urbanized or developed areas while areas with low NDBI values represented minimal or no built-up structures.

4.2. LULC Maps

In this chapter, we present the LULC maps for the years 2018, 2019, 2020, 2021, and 2022 for the study area. The maps showcase the distribution and extent of different land cover classes within the study area. The classification process involved identifying and categorizing seven distinct major classes, namely Water, Trees, Flooded Vegetation, Crops, Built Area, Bare Ground, and Rangeland.

To carry out the classification and analysis, the powerful capabilities of the Google Earth Engine platform were leveraged. This platform provided the necessary tools and resources to process and analyze the huge volumes of satellite imagery and geospatial data required for the classification task. The classification algorithm used in the analysis was implemented within the Google Earth Engine environment, allowing for efficient and scalable processing.

Once the classification was performed, the resulting LULC maps were further refined and visualized using ArcGIS Pro. ArcGIS Pro served as a valuable tool for mapping and projecting the acquired data in a presentable format, such as images or PDF documents. With its advanced mapping and visualization capabilities, ArcGIS Pro allowed us to create high-quality maps that effectively conveyed the spatial distribution and patterns of the different land cover classes. Each year was closely monitored to assess the changes and trends in land cover dynamics. By comparing the LULC maps for consecutive years, temporal variations in the extent and composition of different land cover classes were identified. This temporal analysis provided valuable insights into the evolving patterns of LULC within the study area. The combination of Google Earth Engine and ArcGIS Pro proved to be a powerful and effective approach for studying and monitoring land cover dynamics over time.

Figure 4.25 shows the LULC Map of Adana in 2018, a total of 7 seven classes Water, Trees, Flooded Vegetation, Crops, Built Area, Bare Ground and Rangeland were classified in GEE. The Esri 2020 Global Map being of the best maps in terms of visualization for LULC changes was referenced for color codes which were generated into a palette for usage in the code editor as explained in the Chapter 3.2 of the study. With an overall accuracy of 85%, the total area classified was 15749.65 square kilometers with Water encompassing 103.35 square kilometers, Flooded Vegetation with 131.35 square kilometers, Crops with 4055.67 square kilometers, Built Area with 105.87, Bare Ground with 26.67 square kilometers and Rangeland with 8112.73 square kilometers.

To fully understand the accuracy of results and validate them, Google Earth Pro was used as a reference for the true RGB image utilized as Ground Truth Data due to lack of resources for actual field surveys of the area. It was observed that classes such as Water, Crops, Trees, Flooded Vegetation and Rangeland were quite correctly classified by the algorithm with manual re-classification applied in some instances. Classes such as Built Area and Bare Ground can exhibit spectral heterogeneity, mixed signatures and complexities in feature extraction making more challenging to classify while classes such as Water and Crops possess distinct and consistent spectral signatures and patterns making it easier to classify.

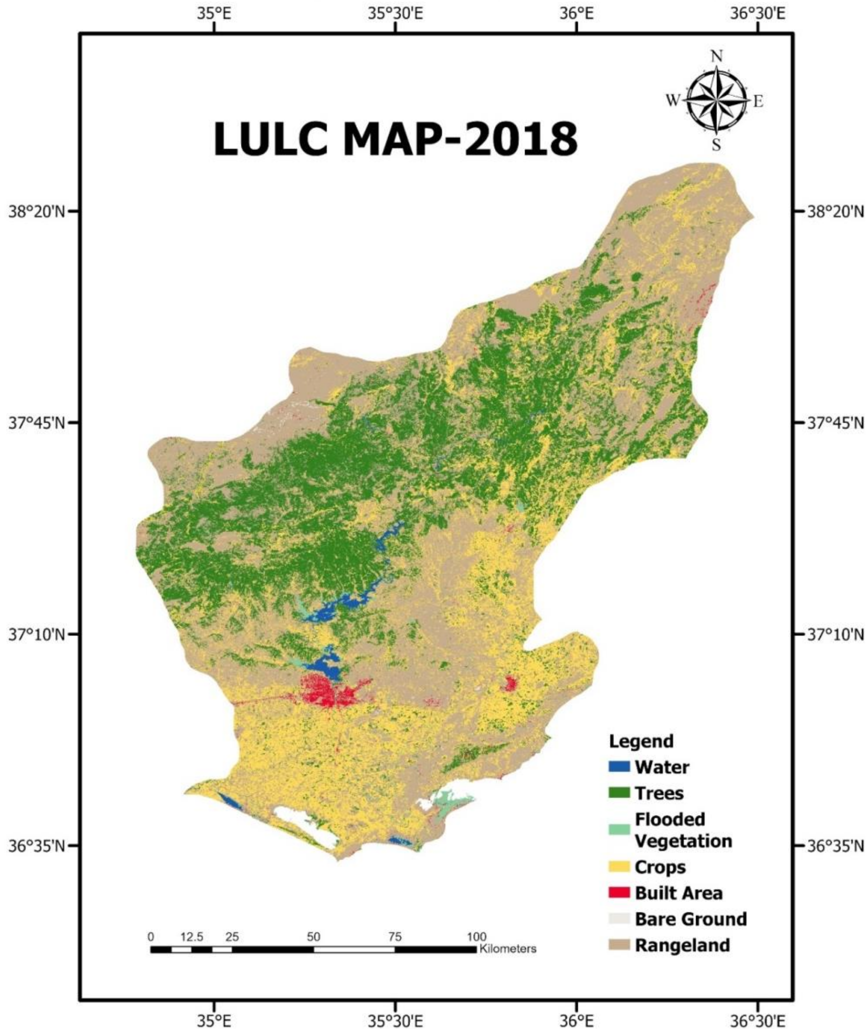

Figure 4.25 Land Use and Land Cover (LULC) Map of Adana Province in 2018

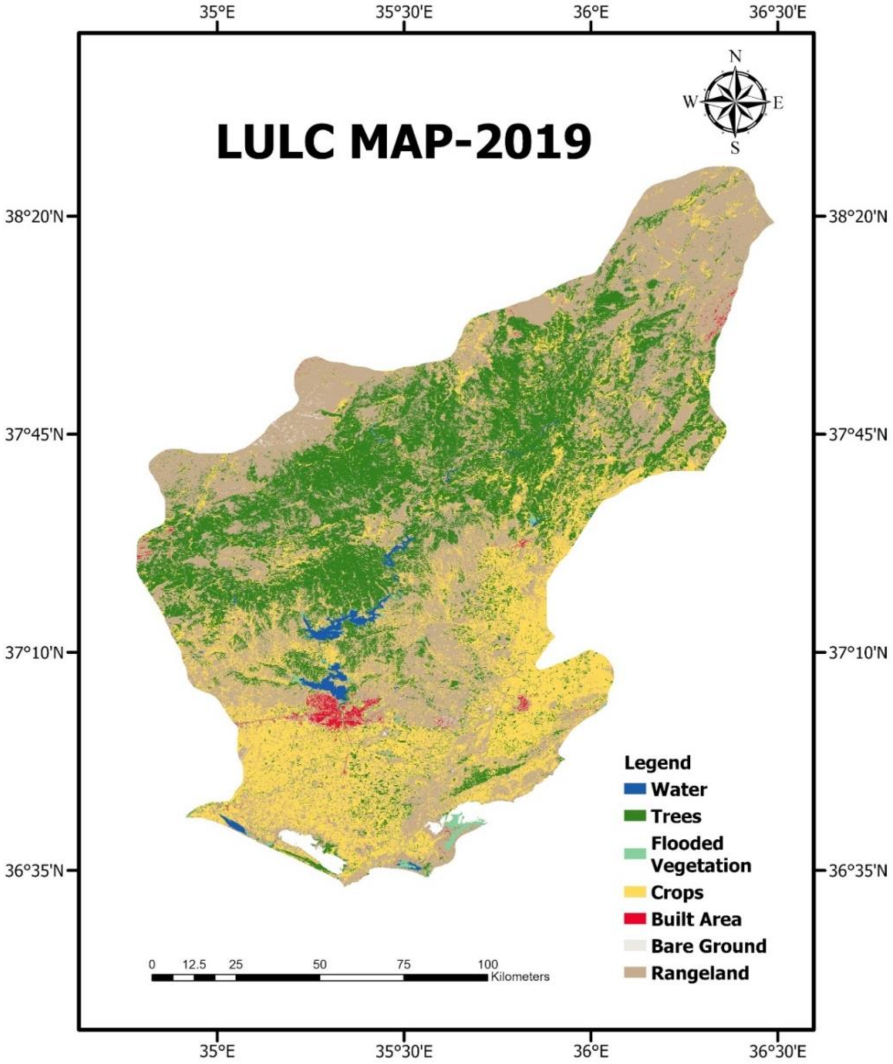

Figure 4.26 Land Use and Land Cover (LULC) Map of Adana Province in 2019

As a comparison to the LULC Map of 2018 in Figure 4.25, the LULC Map of 2019 in Figure 4.26 above had similar features with changes in areas of the classified classes. A total area of 15627.68 square kilometers was classified, a slight reduction as compared to 2018. Water had 137.38 square kilometers, Trees 4591.36 square kilometers, Flooded Vegetation 123.38 square kilometers, Crops a total of 4092.53 square kilometers, Built Area with 107.48 square kilometers, Bare Ground 30.57 square kilometers and finally Rangeland with 6589.98 square kilometers as shown in Table 4.12. With visual validation in relation to the ground truth data referenced from Google Earth Pro and comparison to the previous year, classes such as Trees and Water bodies showed slight increase compared to the previous year as obtained. The flooded vegetation areas in the central parts of the map also portrayed a decrease in area indicating a reduction for 2019. Other classes, though difficult to visualize and contradict with the previous also showed correct classified classes when validated with ground truth data referenced.

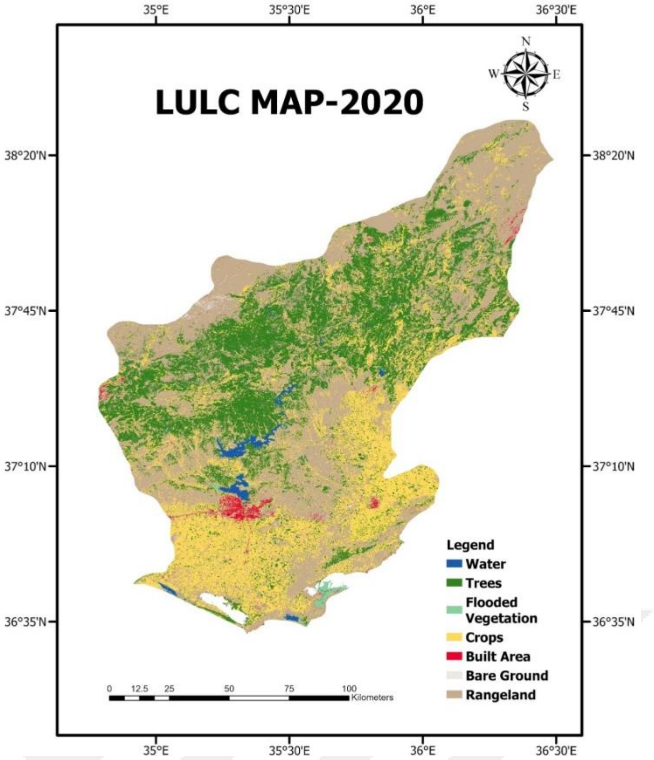

Figure 4.27 Land Use and Land Cover (LULC) Map of Adana Province in 2020

Furthermore, 2020 had a total area of 15836.54 square kilometers classified showing an increase from both 2018 and 2019. The increase was attributed to growth in areas such as Built Area. Built Area recorded an area of 127.9 square kilometers, higher than 2018 and 2019 as shown in Table 4.12. Despite other classes not been greater than the previous years the consistency and trend was observed in the estimated area values in the table. Water had 136.25 square kilometers, Trees had 4366.98 square kilometers, Flooded Vegetation 91.47 square kilometers, Crops with 4010.47 square kilometers, Bare Ground 27.66 square kilometers and Rangeland as 7075.79 square kilometers. The area with Flooded Vegetation East of the map showed a decrease indicating a reduction from the previous year 2019 as can be seen on Figure 4.27 above. Furthermore, a sprout in Built Area was observed across the map with and in more distinct areas such as West, North East and Central parts of the map. The other areas were also validated with Google Earth Pro and manual reclassifications applied in area showing false pixels.

2021 as shown in Figure 4.28 below, however showed a reduction in the total classified area as compared to 2020. A total area of 15760.59 square kilometers was classified with rapid increases in classes such as crops and built area. Crops recorded an area of 4557.79 square kilometers as shown in Table 4.12. The increase in Crop Area in 2021 from 4055.67 in 2018, 4092.53 in 2019. 4010.47 in 2020 was influenced by factors such as improved agricultural productivity, favorable weather conditions with optimal rainfall patterns and temperature, expansion in cultivation areas, new crop plantations, mechanized and modern ways of farming, enhanced irrigation methods or introduction of high yield crops. As these were positive assumptions, negative assumptions related to the drastic increase in crop land would have been related to misplaced pixels or low quality of imagery in the designated areas for the algorithm to capture the precise details of crop related classes. Additionally, Built Area also increased steadily from 127.9 square kilometers in 2020 to 128.33 square kilometers in 2021 also attributed to continuous developmental factors in the area.

Areas such as Rangeland, Trees and Water with 6974.23, 3857.12 and 118.31 square kilometers also saw a decrease compared to the previous year. The decrease was attributed to factors such as the creation of more Built Areas and cultivating of Rangelands for agriculture activities. Furthermore, Bare Ground and Flooded Vegetation also showed consistent values of 23.4 and 101.2 square kilometers as the previous year’s shown in Table 4.12.

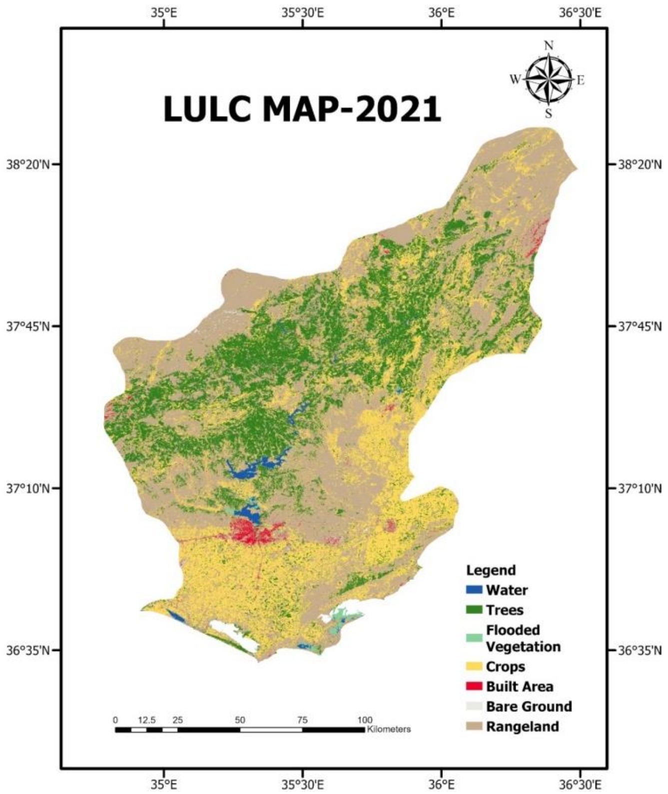

Figure 4.28 Land Use and Land Cover (LULC) Map of Adana Province in 2021

Finally, 2022 had a total area of 15834.87 square kilometers showing an increase from 2021. Areas such as Crops saw a drastic change from all the previous years with influencing factors discussed in this chapter. Built Areas also continued to increase steadily showing the advancement and developmental changes in the area over a five year period. The area of Bare Ground however, decreased gradually from 23.54 in 2021 to 15.29 in 2022 as shown in Table 4.12 influenced by factors such as urbanization and increase in agriculture production. Water areas also saw a steady increase influenced by factors such as advancement in irrigation and good water management in the area.

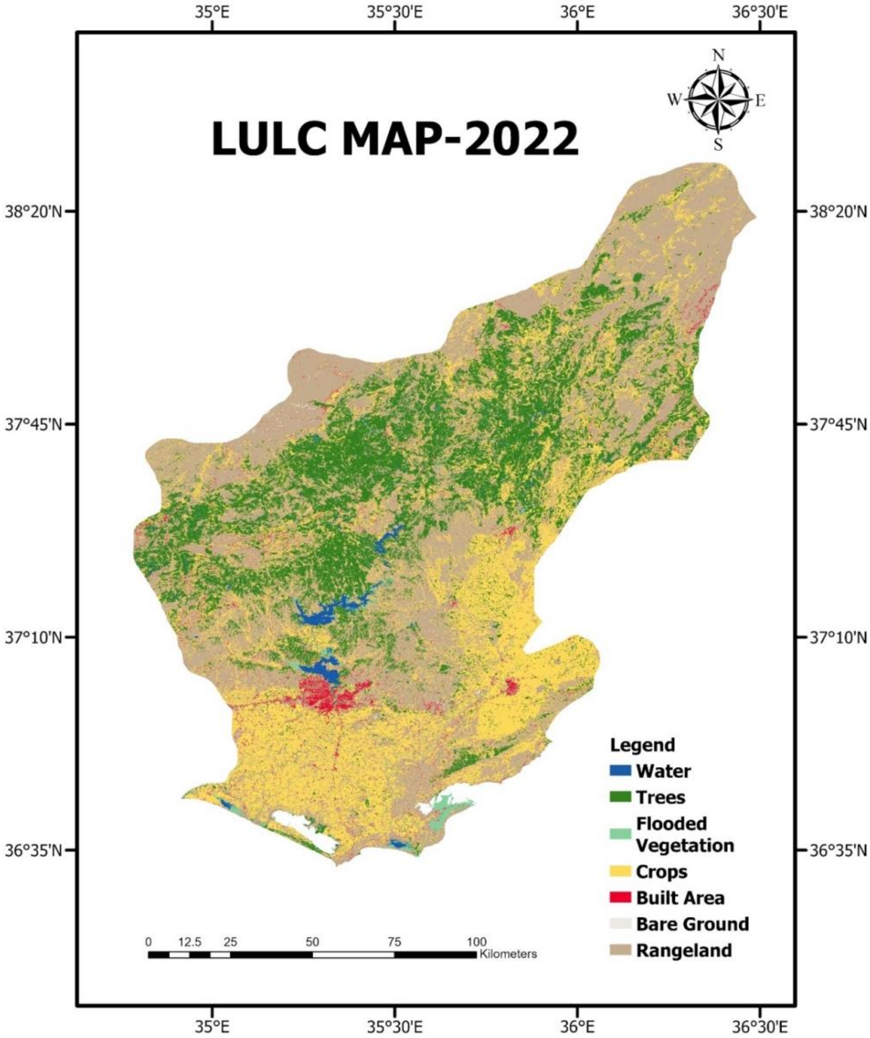

Figure 4.29 Land Use and Land Cover (LULC) Map of Adana Province in 2022

To perfectly distinguish the differences in the classified classes. A code snippet was also used in the Earth Engine to extract each class as a Map layer and classify the rest as other classes for visual representations of different classes derived from the classified images from 2018 to 2022. Different classes were also defined based on their respective indices and assigned a binary image layer. All classes involved such as Water, Trees, Flooded Vegetation, Crops, Built Area, Bare Ground and Rangeland were distinctively isolated and mapped for each year. This type of methodology helped in understanding the trend in specific land cover classes, spatial distribution and relationship between land cover types over the study period.

Figure 4.30 below shows the Water (LULC) Maps of Adana for the year 2018 to 2022. Areas with water were classified with Blue and other classes with dark grey as represented on the Legend. The year 2018 had 103.35 square kilometers of water, 2019 had 137.38 square kilometers, 2020 with 136.25 square kilometers, 2021 with 118.31 square kilometers and 2022 with 129.86 square kilometers. It was observed that the year 2019 had the most area classified for water and 2021 had the least. As it was practically impossible to clearly visualize the difference in the changes, it was observed that Map 2019 and 2020 had broader water areas classified and distributed further North and East as compared to the other maps shown. After careful observation and visualization from ground truth data referenced from Google Earth Pro, it was evident that the area had more water bodies in the central parts of the region as shown in the classified maps.

The fluctuating water coverage depicted in Figure 4.30 below signifies vital hydrological changes within the Adana region. The surge in water areas observed in 2019, followed by subsequent fluctuations, may denote variations in rainfall patterns, river flow dynamics, or agricultural practices. The pronounced decrease in water coverage in 2022 could indicate alterations in hydrological cycles, potentially influenced by changes in precipitation or land-use practices. Such fluctuations hold implications for ecosystem health, agricultural productivity, and water resource management strategies.

Climate change is a significant factor that can influence hydrological cycles. Global warming can lead to increased evaporation rates, altering the amount of water available in a region. It’s crucial to investigate the potential impact of climate change on the observed fluctuations in water coverage. This could involve analyzing long-term climate data and correlating it with the changes observed in Figure 4.30 for advanced water studies.

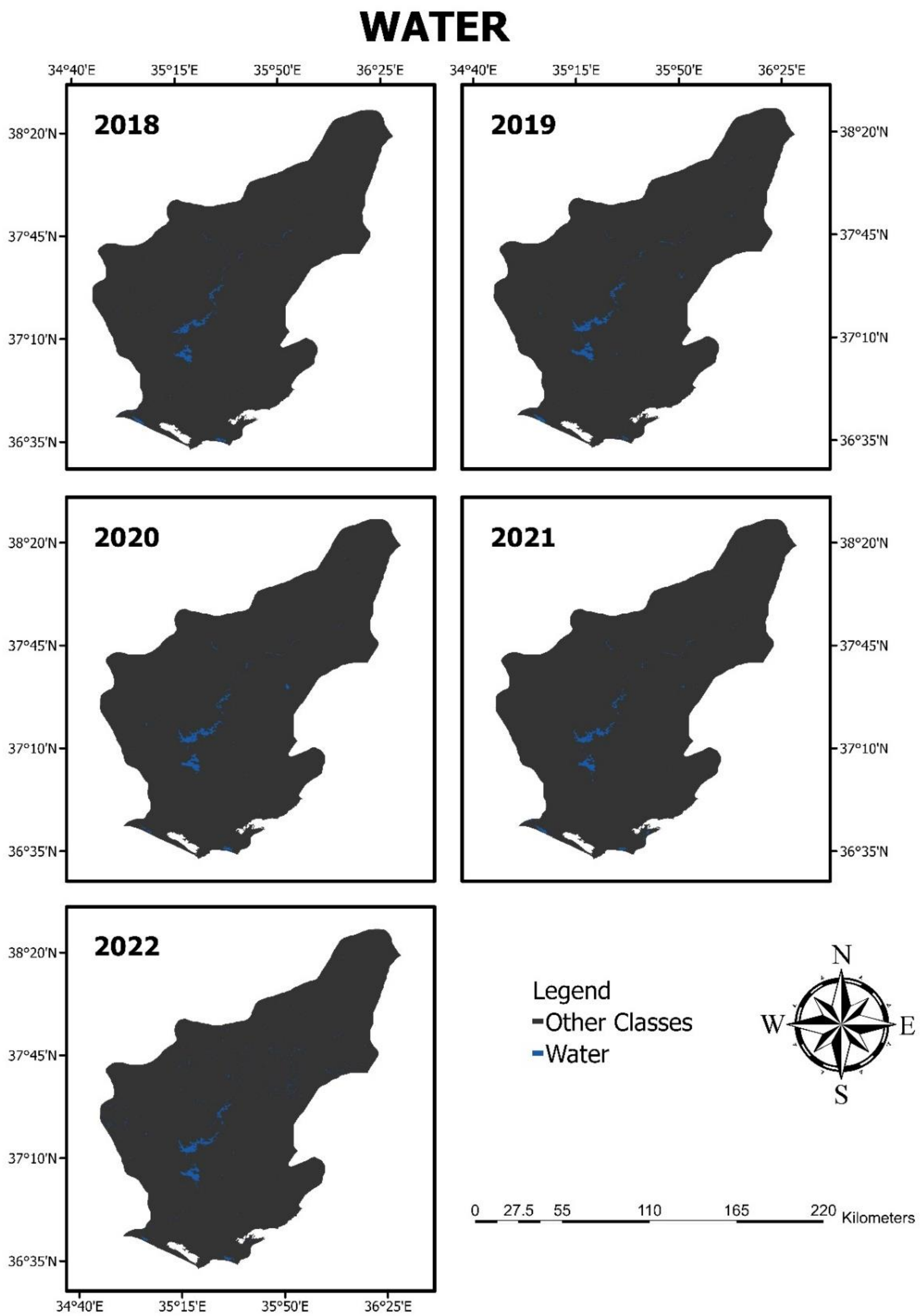

Figure 4.30 Water (LULC) Maps of Adana Province

As a comparison to the isolation of Water classes, the same methodology was also used for tree areas. Areas representing Trees were shown in green while area representing other classes in dark grey as shown in Figure 4.31. The area covered by trees in 2018 was 3214.01 square kilometers, in 2019 was 4591.36 square kilometers, decreased to 4366.98 square kilometers in 2020, while 2021 showcased an area of 3857.12 square kilometers and finally 2022 had 2862.93 square kilometers as shown in Table 4.12. The year 2019 had the most area covered by trees while

2018 had the least areas. Upon visual inspection of the maps, it was observed that map 2019, 2020 and 2021 had more areas of trees shown compared to 2018 and 2022 which saw a reduction in the South West regions validating the information obtained.

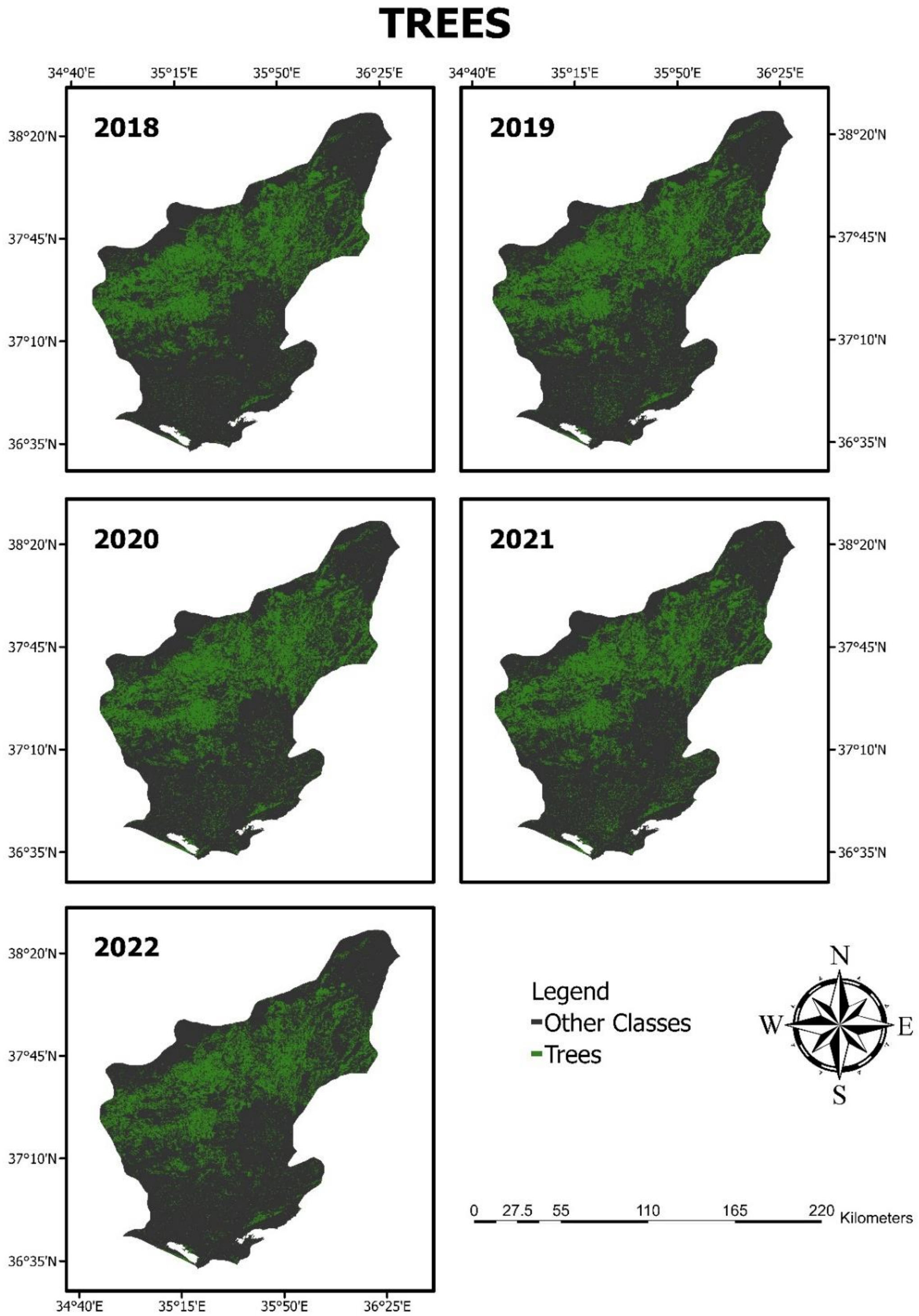

Figure 4. 31 Tree (LULC) Maps of Adana Province

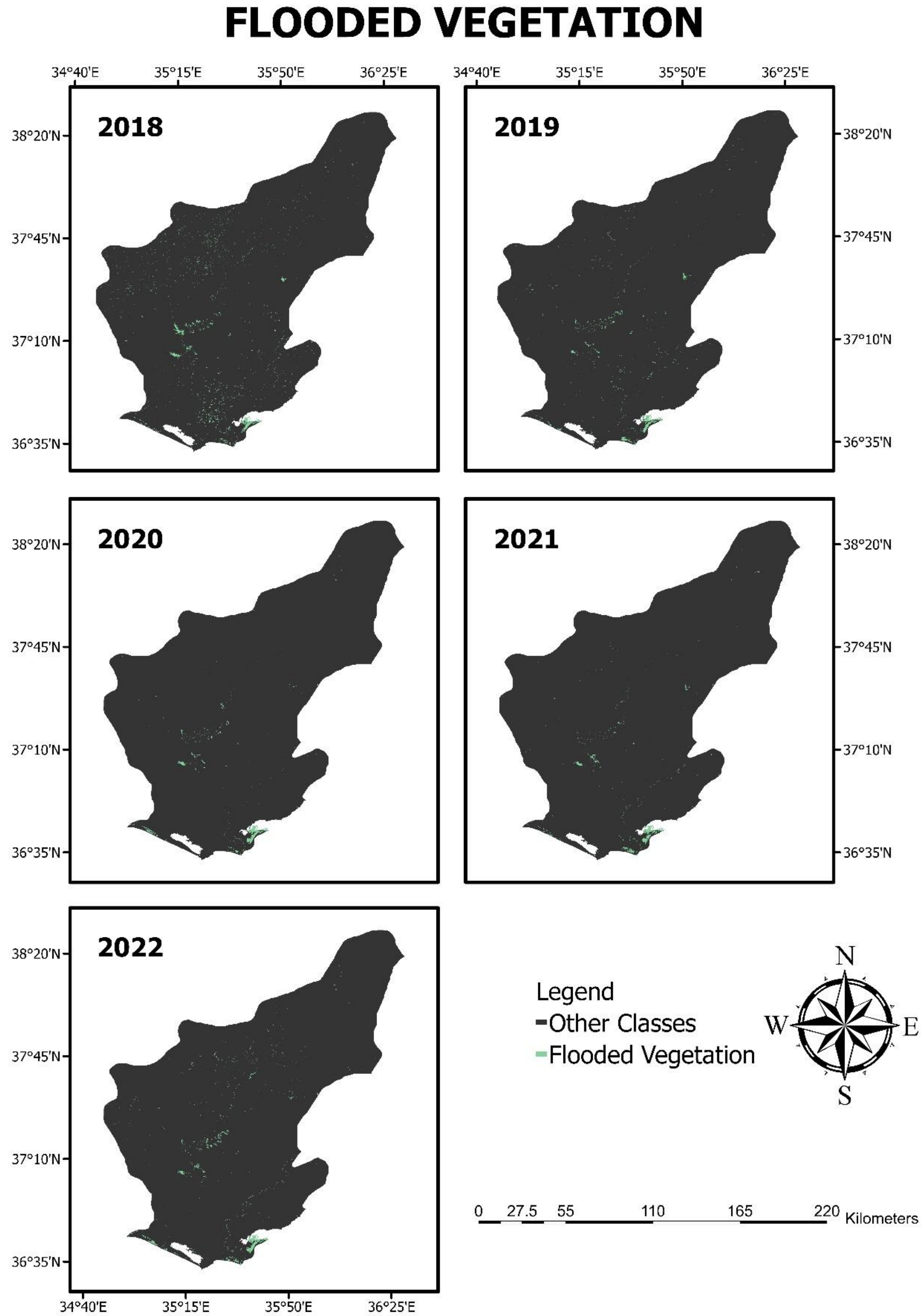

Figure 4.32 Flooded Vegetation (LULC) Maps of Adana Province

Flooded Vegetation however, as shown in Figure 4.32 above was easier to visualize the changes on the maps for the study interval. Light blue represented areas with flooded vegetation while dark grey represented other classes. Notably, as seen on the maps 2018, 2019 and 2022 demonstrated larger flooded vegetation areas sprouted over the region as compared to subsequent years. 2020 and 2021 showed a reduction in the flooded vegetation in the Northern and Southern parts as visually observed. 2018 had an area value of 131.35 square kilometers, 2019 a value of 123.38 square kilometers, 2020 a value of 91.49 square kilometers, while 2021 showcased an area of 101.27 square kilometers and 2022 had 126.62 square kilometers.

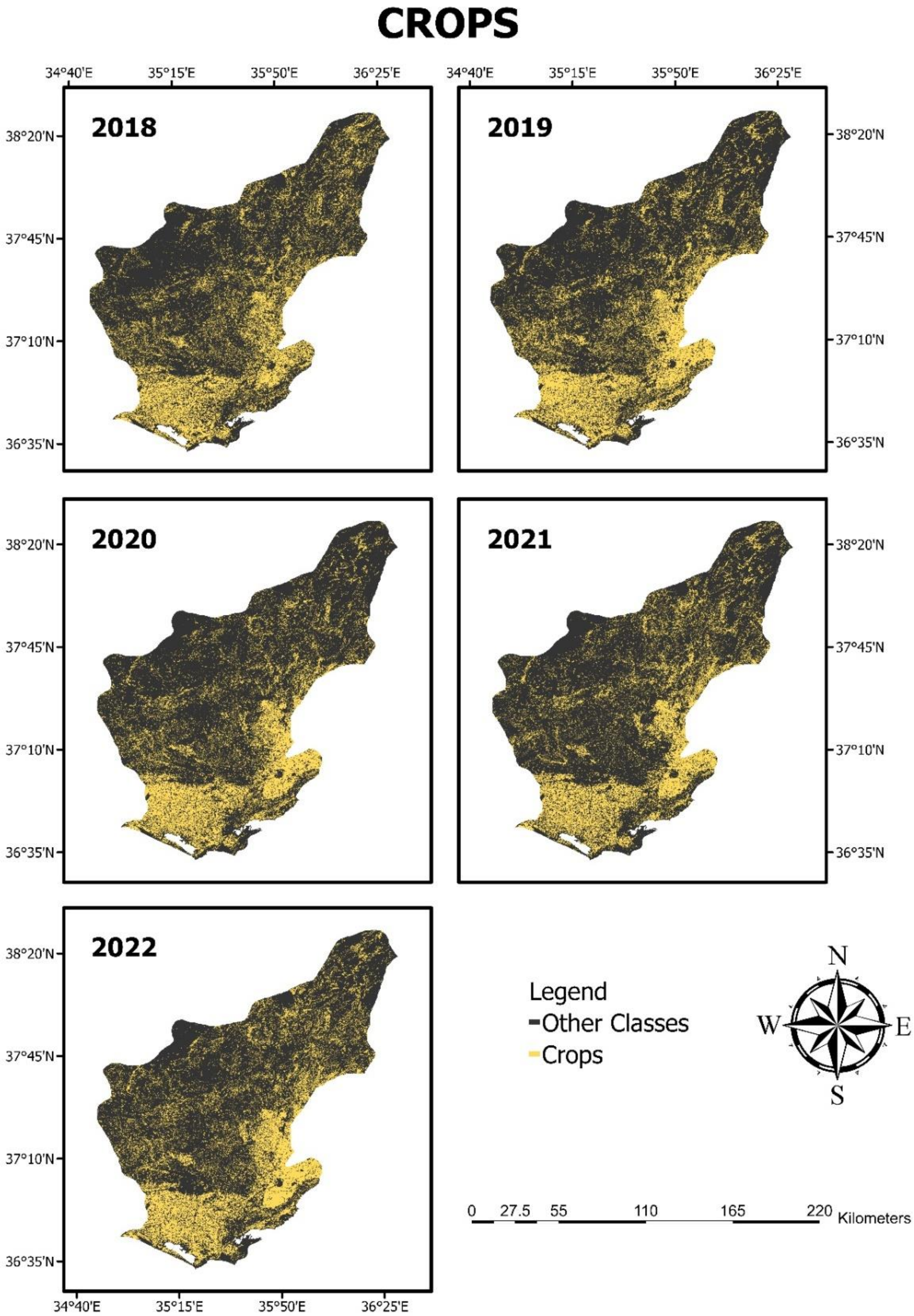

Figure 4.33 Crops (LULC) Maps of Adana Province

The area covered by crops was 4055.67 square kilometers in 2018, 4092.53 square kilometers in 2019, while 2020 saw an area of 4010.47 square kilometers and 2021 with 4557.79

square kilometers. Finally, the highest recorded was 4897.43 square kilometers in 2022. As shown on Figure 4.33 above yellow was used to represent areas with crops while dark grey was used to represent other areas. As it was tougher to perfectly see the changes on the maps, the most extensive and broadly spread areas appeared in 2022, 2021 and 2019 with also slightly similar classified areas in 2018 and 2020 but with less condensed areas in the Western regions. Upon validation with Ground truth data it was observed that parts in the Southern region were denser in Crops compared to the rest as also correctly classified on the maps shown.

Built Area however, of all the classes involved was the most complex and difficult to classify. Manual reclassification had to be done in areas were mixed pixels or false values were obtained. As validated from the ground truth data obtained from Google Earth Pro, Central parts on the region contained more areas with Built Area representing the economic zone of the study area Adana as visually observed. Furthermore, as shown in Figure 4.34 below red was used to represent Built Area while dark grey was used to represent other classes. In 2018, Built Area had an area value of 105.87 square kilometers, while 2019 had 107.48 square kilometers, 2020 however, recorded 127.9 square kilometers and 2021 had 128.33 square kilometers. The highest recorded was in 2022 with 130.19 square kilometers depicting the gradual change in settlements and industrialization in the area. Furthermore, as obtained in Figure 4.34, 2022 had more scattered areas classified as Built Areas compared to the previous 4 years.

As compared to Built Area, classifying Bare Ground also pertained to be challenging due to mixed pixels and low-resolution imagery for the study. As it was difficult to properly assign training samples to this class because of the confusion with Rangeland only distinct areas that showed actual signs of Bare Ground were put into consideration. As also shown in Figure 4.35 below, areas with white were classified as Bare Ground while areas with dark grey were classified as other classes. As the areas with the lowest classified class, 2018 had an area value of 26.67 square kilometers, 2019 with 30.67 square kilometers, 2020 with 27.66 square kilometers, while 2021 had 23.54 square kilometers and finally 15.29 square kilometers for 2022 as shown in Table 4.12. The drastic change in Bare Ground for 2021 and 2022 could be attributed to robust developmental activities and agriculture. As usually observed Southern and Western parts portrayed more areas with Bare Ground compared to the other regions on the maps.

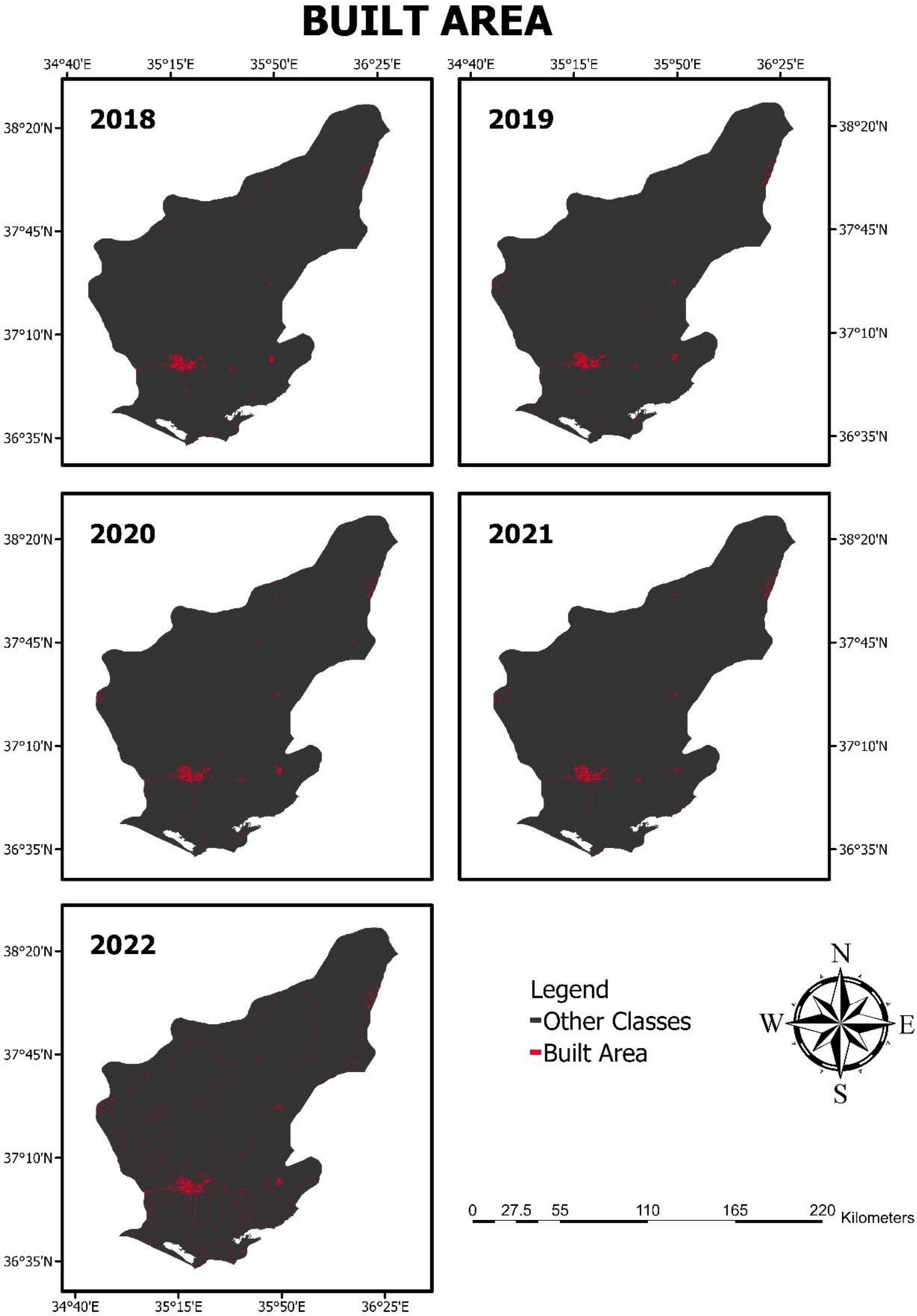

Figure 4.34 Built Area (LULC) Maps of Adana Province

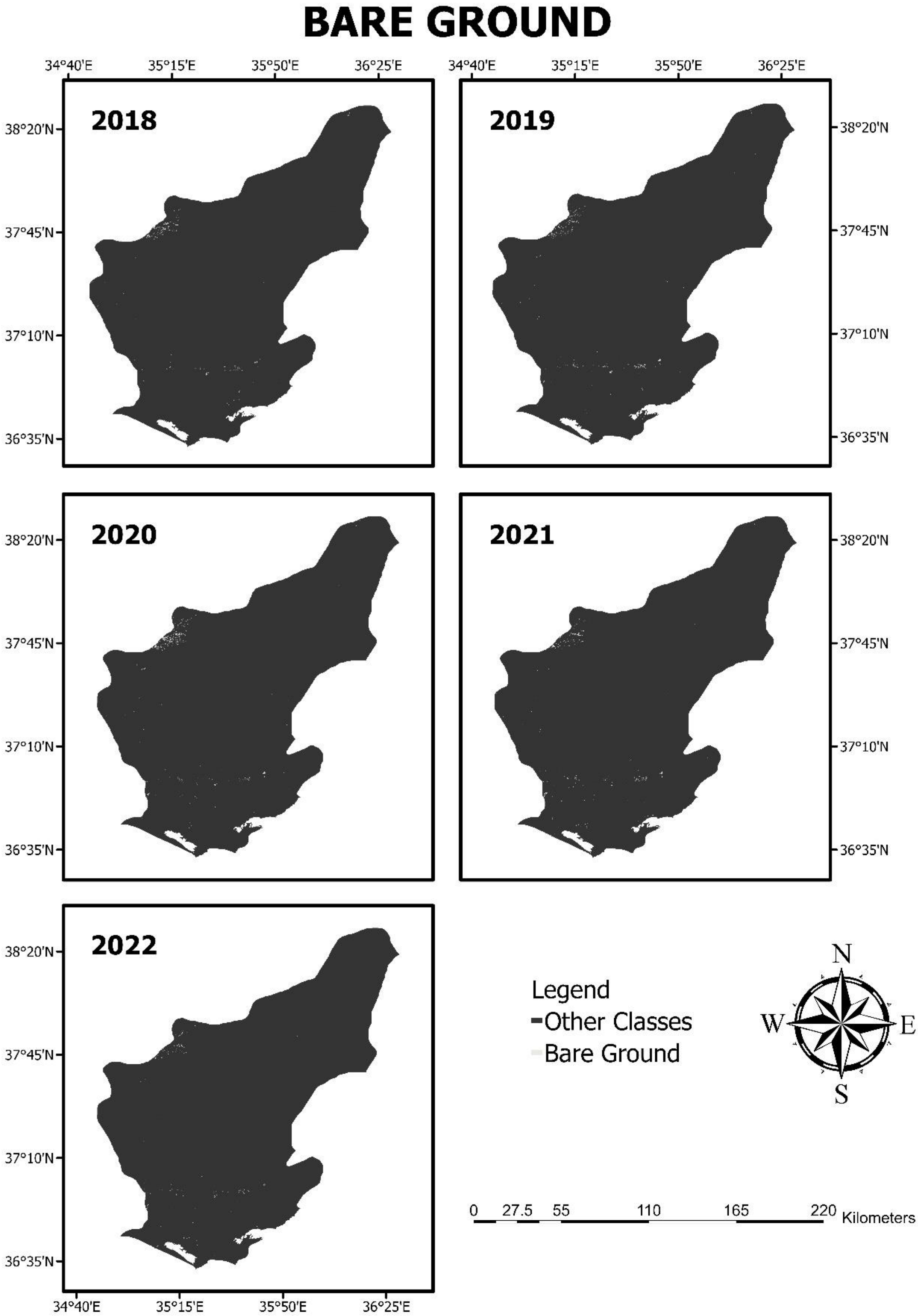

Figure 4.35 Bare Ground (LULC) Maps of Adana Province

Finally, Rangeland was the area with the highest value of classified pixels. Grasslands, Shrublands, Woodlands and Wetlands were all put in this class with distinct training samples collected from the imagery. Figure 4.36, shows the maps of Rangeland from the period of 2018 to 2022. Areas with light brown were classified as Rangeland while areas with dark grey as other classes. The total area of Rangeland classified in 2018 was 8112.73 square kilometers, in 2019 6589.98 square kilometers, 7075.79 square kilometers in 2020, while 2021 had 6974.23 square kilometers and 2022 with 6674.55 square kilometers. As visually observed and referenced from ground truth data, Northern, Western and Central parts showed more areas covered by Rangeland with 2018 and 2020 showing the highest values.

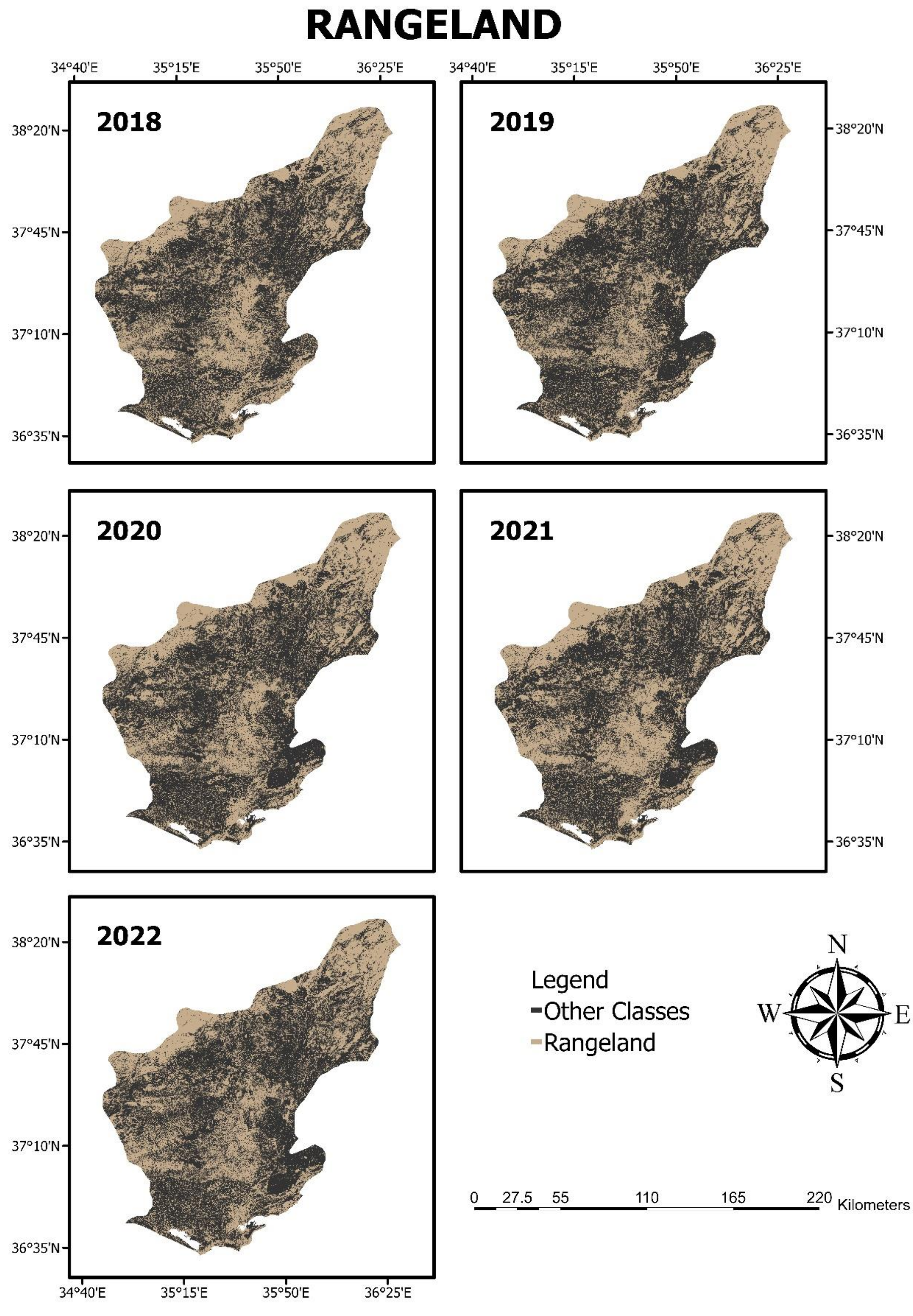

Figure 4.36 Rangeland (LULC) Maps of Adana Province

Table 4.9 Consumer's Accuracy values for 2018, 2019, 2020, 2021 and 2022

CONSUMER'S ACCURACY					
CLASS	**2018**	**2019**	**2020**	**2021**	**2022**
Water	1	1	1	1	1
Trees	0.889	0.875	0.938	0.913	1
Flooded Vegetation	1	1	1	1	0.905
Crops	0.750	0.792	0.963	0.875	0.815
Built Area	0.944	0.857	0.800	0.767	0.750
Bare Ground	0.667	1	0.778	0.667	0.714
Rangeland	0.827	0.870	0.875	0.873	0.916

There are different accuracy metrics to demonstrate the quality of the classification results. Table 4.9 provides the Consumer's Accuracy values for different land cover classes shown for the respective years. The results represent correctly classified pixels for each class, indicating the reliability of the classification results. A breakdown of the results showed that they were a 100% accuracy in Water, meaning all water pixels were correctly classified as water from 2018 to 2022. For tree classification, an accuracy of 88.9% was achieved in 2018, meaning that 88.9% of tree pixels were correctly classified as trees. The accuracy slightly decreased to 87.5% in 2019 but improved to 93.8% in 2020. In 2021, the accuracy was 91.3%, and in 2022, all tree pixels were correctly classified as trees, resulting in 100% accuracy.

The classification of flooded vegetation showed 100% accuracy in 2018, 2019, 2020, and 2021, indicating precise identification of flooded vegetation pixels. However, in 2022, the accuracy decreased to 90.5%, with 90.5% of flooded vegetation pixels correctly classified. In 2018, 75% of crop pixels were accurately classified as crops, resulting in 75% accuracy. The accuracy improved to 79.2% in 2019 and further increased to 96.3% in 2020. In 2021, the accuracy was 87.5%, and in 2022, it slightly decreased to 81.5%.

For the classification of built areas, an accuracy of 94.4% was achieved in 2018, indicating that 94.4% of built area pixels were correctly classified. The accuracy decreased to 85.7% in 2019 and further dropped to 80% in 2020. In 2021, the accuracy was 76.7%, and in 2022, it decreased to 75%. In 2018, the accuracy for bare ground classification was 66.7%, meaning that 66.7% of bare ground pixels were correctly classified. The accuracy improved to 100% in 2019 but decreased to 77.8% in 2020. In 2021, the accuracy was 66.7%, and in 2022, it slightly increased to 71.4%. The classification of rangeland achieved an accuracy of 82.7% in 2018, indicating that 82.7% of rangeland pixels were correctly classified. The accuracy increased to 87% in 2019 and remained consistent at 87.5% in 2020. In 2021, the accuracy was 87.3%, and in 2022, it further improved to 91.6%.

Table 4.10 Producer’s Accuracy values for 2018, 2019, 2020, 2021 and 2022

PRODUCER'S ACCURACY					
CLASS	**2018**	**2019**	**2020**	**2021**	**2022**
Water	1	1	1	1	1
Trees	0.813	0.944	0.882	0.913	0.875
Flooded	1	1	1	1	1
Crops	0.742	0.800	0.765	0.700	0.957
Built Area	0.645	0.660	0.800	0.639	0.724
Bare Ground	0.333	0.200	0.778	0.667	0.714
Rangeland	0.932	0.940	0.933	0.944	0.902

However, the Producer's Accuracy for Water class was consistently 100% for all the years (2018, 2019, 2020, 2021, and 2022) as shown in Table 4.10. This indicates that all the water pixels in the study area were correctly classified as water throughout the entire period. For the Trees class, the Producer's Accuracy varied across the years. In 2018, 81.3% of tree pixels were correctly classified as trees. The accuracy improved in 2019 with 94.4%, followed by 88.2% in 2020 and 91.3% in 2021. In 2022, the accuracy slightly decreased to 87.5%, but still maintained a high level of correct classification for tree pixels.

The Producer's Accuracy for the Flooded Vegetation class was consistently 100% for all the years, indicating that all the pixels representing flooded vegetation were accurately classified as such throughout the study period. The accuracy of classifying the Crops class varied across the years. In 2018, 74.2% of crop pixels were correctly classified as crops. The accuracy improved to 80% in 2019 but slightly decreased to 76.5% in 2020. In 2021, the accuracy further decreased to 70%. However, in 2022, the classification accuracy significantly improved to 95.7%, indicating a high level of correct identification of crop pixels. The accuracy of classifying the Built Area class showed some variation over the years. In 2018, 64.5% of built area pixels were correctly classified. The accuracy slightly increased to 66% in 2019 and further improved to 80% in 2020. However, in 2021, the accuracy decreased to 63.9%. In 2022, the accuracy slightly improved to 72.4%, but there was still some inconsistency in the classification of built area pixels.

For the Bare Ground class, the Producer's Accuracy varied across the years. In 2018, only 33.3% of bare ground pixels were correctly classified. The accuracy decreased in 2019 with 20%, followed by a significant improvement to 77.8% in 2020. However, in 2021, the accuracy decreased to 66.7%. In 2022, the accuracy slightly improved to 71.4%, like Built Areas, there was still some inconsistency in correctly classifying bare ground pixels.

The Producer's Accuracy for the Rangeland class was consistently high across the years. In 2018, 93.2% of rangeland pixels were correctly classified. The accuracy remained high in 2019 with 94%, and slightly decreased to 93.3% in 2020. In 2021, the accuracy improved to 94.4%. In 2022, the accuracy decreased slightly to 90.2%, but overall, the classification of rangeland pixels showed a high level of accuracy.

Table 4.11 Overall Accuracy and Kappa Statistics values for 2018, 2019, 2020, 2021 and 2022

Year	OVERALL ACCURACY (%)	KAPPA STATISTIC (%)
2018	0.85	0.86
2019	0.86	0.81
2020	0.90	0.85
2021	0.85	0.83
2022	0.89	0.83

In 2018, the overall accuracy of the classification results was 85%, indicating that 85% of the pixels were correctly classified. The kappa statistic, which is defined to measure the similarity between the classification and reference data beyond what would be expected by chance, was 0.86. Thereby, indicating that the classification results for that year were reasonably accurate and reliable. Moving on to 2019, the overall accuracy slightly increased to 86%, indicating an improvement in the classification performance compared to the previous year. The kappa statistic was 0.81, indicating an agreement between the classification and reference data. These results suggest that the classification for 2019 was also consistent and reliable.

In 2020, the overall accuracy increased to 90%, compared to the previous year. The kappa statistic also increased to 0.85 indicating a substantial adjustment and showing consistency in the classification performance. However, in 2021, there was a slight decrease in the overall accuracy, which dropped to 85%. This decrease suggests that the classification results for that year were less accurate compared to the previous years. The kappa statistic also decreased to 0.83, indicating a substantial but slightly lower agreement between the classification and reference information. This decline may be attributed to various factors; such as changes in land cover patterns or classification errors.

Lastly, in the final year, 2022, the overall accuracy showed an improvement, reaching 89% indicating a higher level of accuracy in the classification results for that year. The kappa statistic remained the same as 2021 at 0.83, showcasing an improved performance compared to 2021. Overall, the classification accuracy fluctuated slightly across the years, with the highest overall accuracy and kappa statistic observed in 2020 at 90% and in 2018 0.86 hence summarized as shown in the above Table 4.11.

Table 4.12. shows the areas values in square kilometers for 2018, 2019, 2020, 2021 and 2022 for the selected classes.

Table 4.12 Areas values in square kilometers for 2018, 2019, 2020, 2021 and 2022

AREA (SQKM)					
CLASS	**2018**	**2019**	**2020**	**2021**	**2022**
Water	103.35	137.38	136.25	118.31	129.86
Trees	3214.01	4591.36	4366.98	3857.12	3862.93
Flooded	131.35	123.38	91.49	101.27	126.62
Crops	4055.67	4092.53	4010.47	4557.79	4897.43
Built Area	105.87	107.48	127.9	128.33	130.19
Bare Ground	26.67	30.57	27.66	23.54	15.29
Rangeland	8112.73	6589.98	7075.79	6974.23	6672.55

The total area covered by water was 103.35 square kilometers in 2018. The area of trees was third highest covering 3214.01 square kilometers, and crops second with an area of 4055.67 square kilometers. Flooded vegetation covered 131.35 square kilometers and built area had a total area of 105.87 square kilometers, while bare ground covered 26.67 square kilometers. The highest area obtained was for Rangeland with 8112.73 square kilometers.

Moving on to 2019, the area of water increased to 137.38 square kilometers, indicating a larger water coverage compared to the previous year. The area of trees also increased to 4591.36 square kilometers. Rangeland continuing to be dominant covered an area of 6589.98 square kilometers with a decrease compared to 2018, while crops covered 4092.53 square kilometers. Flooded vegetation decreased slightly to 123.38 square kilometers, and the built area remained relatively stable at 107.48 square kilometers. Bare ground increased to 30.57 square kilometers.

The areas of water, trees, and crops in 2020, remained similar to the previous years. Crops covered an area of 4010.47 square kilometers, indicating a slight decrease compared to 2019. Flooded vegetation decreased further to 91.49 square kilometers, while the built area expanded to 127.9 square kilometers. The area of bare ground was 27.66 square kilometers while water, trees and crops were 136.25, 4366.98 and 4010.47, respectively.

Additionally, in 2021 the area of water decreased to 118.31 square kilometers, while trees covered 3857.12 square kilometers. Crops expanded to 4557.79 square kilometers, indicating a significant increase compared to the previous years. The area of flooded vegetation increased slightly to 101.27 square kilometers. The built area covered 128.33 square kilometers, and bare ground decreased to 23.54 square kilometers. Rangeland covered 6974.23 square kilometers also showing a decrease compared to 2020.

Finally, in 2022 Table 4.12, the area of water increased again to 129.86 square kilometers, while trees covered 3862.93 square kilometers. Crops had the second highest area, covering 4897.43 square kilometers. Flooded vegetation covered 126.62 square kilometers. The built area increased slightly to 130.19 square kilometers, while bare ground decreased to 15.29 square kilometers. Rangeland again showed a slight decrease compared to the two previous years covering 6672.55 square kilometers.

4.3. Factors Influencing Accuracy Metrics in Land Cover Classification

The low and inconsistency in Consumer's (User's) and Producers Accuracy in classes such as Built Area, Bare Ground and Crops can be attributed to several factors known to inhibit classification. The major factor is misclassification which saw the classification algorithm having difficulty in accurately distinguishing between Built Area, Crops and Bare Ground classes due to their spectral similarities or compiled land cover patterns and lead to potential misclassification errors, where pixels or objects were incorrectly assigned to the classes. The other major factor was mixed pixels which meant that such classes contained a variety of different land cover types within a single pixel hence making it very challenging for the classification algorithm to accurately assign a single class label to these mixed pixels, resulting in lower accuracy.

Furthermore, the spatial resolution of the imagery used for classification might have had also impacted the accuracy of identifying such classes in the sense that if the resolution is relatively coarse, finer details and nuances of land cover types may not be easily captured leading to a lower accuracy. Data limitations and variability are also major factors that can contribute to lower accuracy and classification results. Temporal and seasonal variations in spectral reflectance properties can be exhibited in land cover classes making more difficult to accurately classify. Additionally, the quality and availability of data used for classification also greatly hinders results.

The discrepancies and inconsistency in overall accuracy and area over the five years was also attributed to several factors as observed with the consumer's accuracy and producer's accuracy. The variations in land cover pattern over time might have influenced the changes. Natural processes such as water flow, vegetation growth and land use practices can lead to fluctuations in land cover patterns hence impacting the accuracy of classification algorithms resulting in inconsistent values across different years. The variation of environmental factors such as weather patterns, cloud cover and natural disaster can affect the quality of satellite imagery used for classification leading to inconsistencies in accuracy. Additionally, change in land management practices or policies can greatly produce uncertainties in the classification results.

However, to address these challenges faced in the final results of the classification, understanding and choosing the most appropriate methods is important. Several researchers faced similar problems and methods have been suggested depending on what works best for the end user. One of the key suggestions was carefully selecting and preprocessing the input data and optimizing the classification algorithm and parameters which had been put in usage for our study. In addition, regular monitoring and validation of land cover maps is also essential to track changes and identify potential sources of inconsistency.

High resolution satellite imagery usage is essential in classification but however, due to limitations in obtaining high quality satellite data which is usually for commercial usage and sale, the study focused on using open source imagery with the highest resolution of 10m. Classes with complex pixels such as Built Areas, Bare Ground and Crops needed imagery that captures all or more details of spatial information allowing for better discrimination and identification of land cover features. Higher resolution imagery also reduces the ambiguity and subjectivity associated with classification as it enhances the reliability and accuracy for classes that might have distinct visual characteristics. Improved mapping of boundaries and detection of small-scale features is also greatly associated with high resolution imagery.

4.4. Subset Implementation

As it was difficult to acquire high resolution imagery for our study, other methods that could increase the accuracy of results and lessen the discrepancies in the area values had to be explored. The most convenient and easiest method was obtaining a subset from the region of interest which involved greatly focusing on key areas such as the built-up area or city center. Obtaining the subset helped to reduce the difference and variability of land cover classes and impact of heterogeneous regions on the classification process. In addition, improved data quality and visualization was also observed in the subset imagery essential for reducing uncertainties in the land cover maps. Consistency in the subset analysis was also key in maintaining temporal changes and trends associated in analyzing the area over multiple years. By keeping the consistency, it was easier to mitigate some of the challenges associated with rapid land cover changes or spatial variations in a large area. Overall, the subset from the study area helped to simplify the analysis, improve data quality, show consistency in area values and validate the accuracy attained over the study period.

4.4.1. Subset Region

The main focus of the subset was the area associated with the built up region in the study area. The subset was perfectly placed to show all details of the city center and key surrounding region of Adana province. The city center of Adana is in the heart of the province and surrounded by notable geographical aspects such as the Seyhan river which flows through the city dividing it into two parts. As it is the longest in Turkey’s Mediterranean region and houses Lake Seyhan as shown in Figure 4.37 below and also plays a really significant role in the city’s landscape. Additionally, the city center is located in the fertile Cukurova plain which is very essential for Turkey’s agriculture needs due to its renowned rich soil and favorable climate to grow vast amounts of crops.

Furthermore, it surrounded by Taurus Mountains, Lakes and Reservoirs such as the Lake Seyhan and Seven Lakes locally called the Yedigöller that also provides unique geographical features to the region.

To perfectly capture the city center and other key geographical features in the region as a subset in Google Earth Engine the polygon features with four (4) vertices was selected with initial coordinates precisely captured for the key interested area. The subset region from the main study area was then classified with the same methodology as the official study area. Manual reclassification was also reapplied but, in less instances, as compared to the previous methodology. Figure 4.37 below shows the subset as the main area of interest.

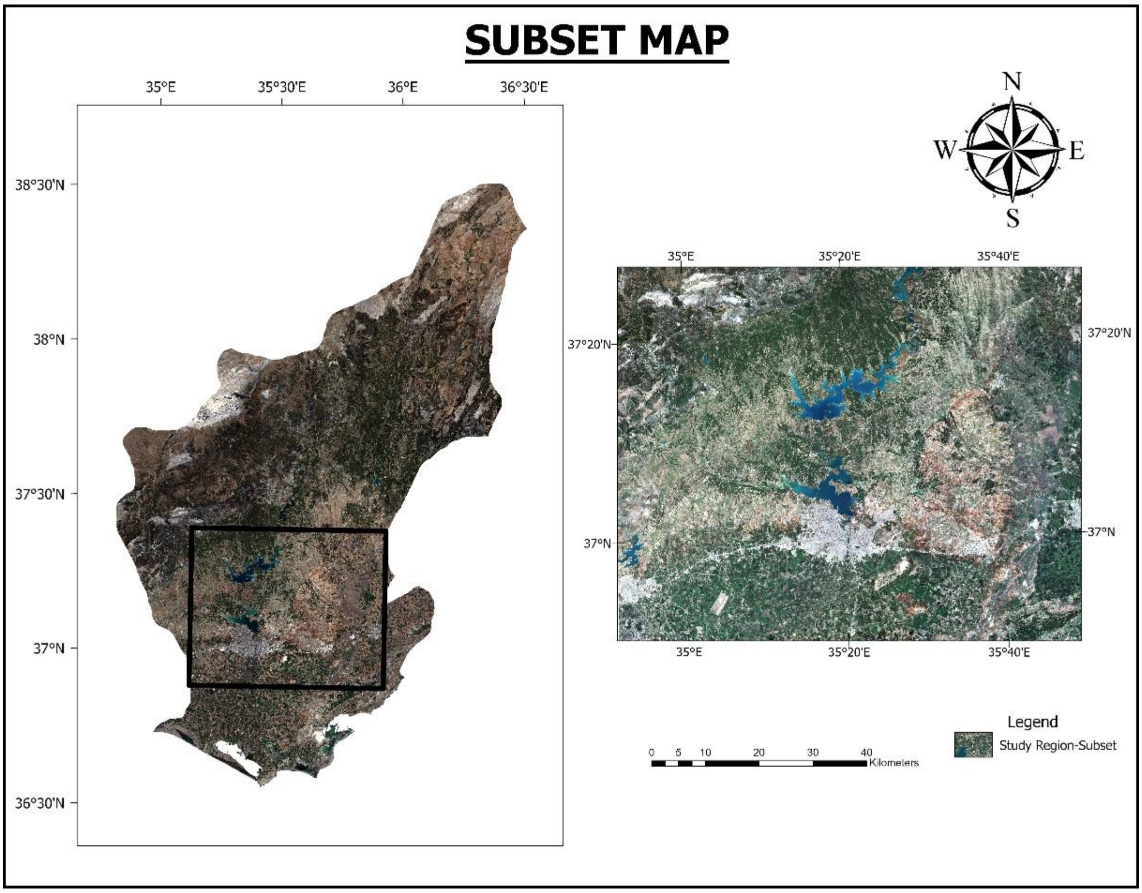

Figure 4.37 Subset Map from Study Area

The same classes were put into consideration as from the previous methodology as Water, Trees, Flooded-Vegetation, Crops, Built Area, Bare Ground and Rangeland. The subset for each year was later classified in Google Earth Engine with the same algorithm and exported to ArcGIS Pro as a tiff file for visual representation.

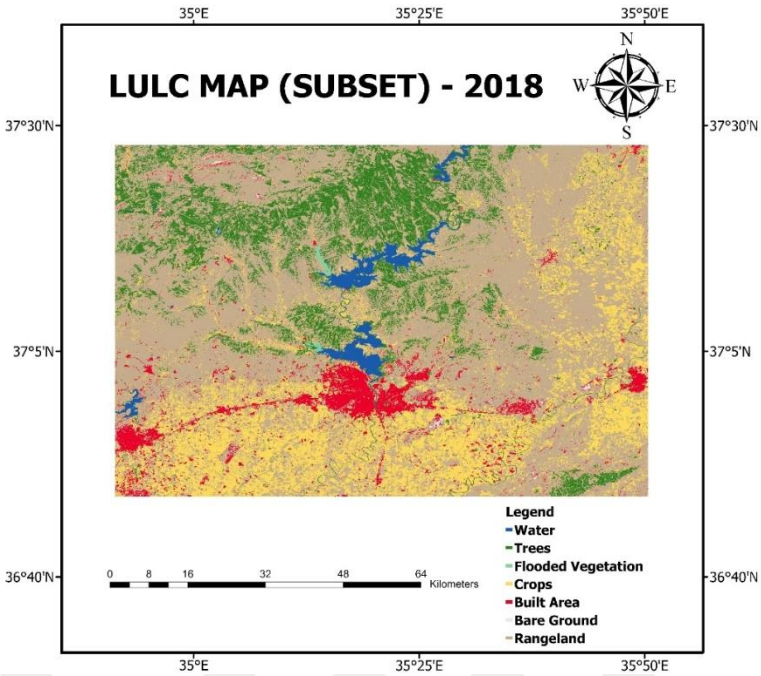

Figure 4.38 LULC Map (Subset) of Adana Province in 2018

Figure 4.38, above shows the LULC Map (Subset) of Adana in 2018. A total of 120.18 square kilometers was classified for Water, 746.20 square kilometers for Trees, 15.51 square kilometers for Flooded Vegetation, 1217.22 square kilometers for Crops, 325.28 square kilometers for Built Area, 14.47 square kilometers for Bare Ground and 3862.99 square kilometers for Rangeland. As observed on the maps it was easier to visualize the different land classes. Built Area been the key focus showed clear distinct classified areas as shown on the map and in relation to the referenced ground data obtained from Google Earth Pro.

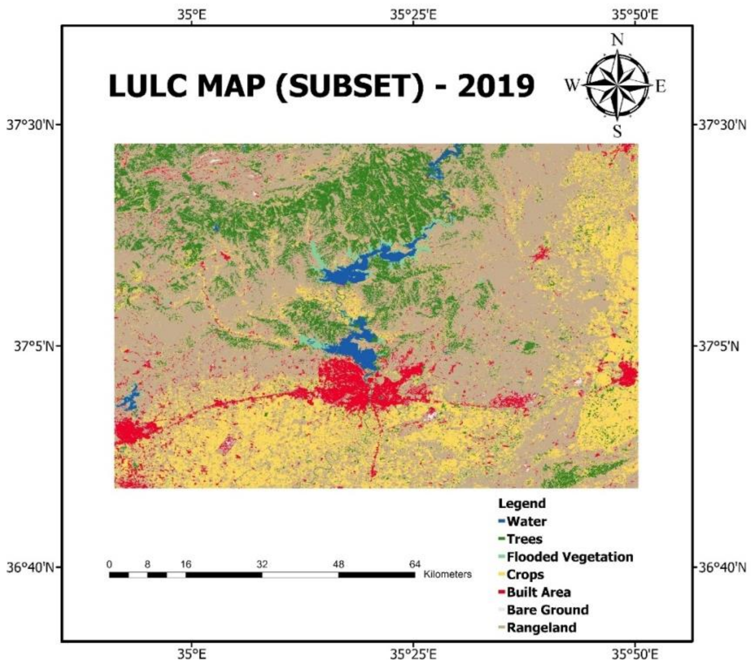

Figure 4.39 LULC Map (Subset) of Adana Province in 2019

Similarly, as 2018, Figure 4.39 shows the LULC map subset of Adana for 2019. Water had an area of 103.89 square kilometers, Trees an area of 721.47 square kilometers, Flooded Vegetation with 65.91 square kilometers, Crops recorded an area of 1357.45 square kilometers, Built Area an area of 331.62 square kilometers, Bare Ground an area of 13.51 square kilometers and finally Rangeland with 3709.03 square kilometers. As evidently observed on the map, in comparison to 2018, classes such as Flooded Vegetation showed a drastic increase in the central parts of the water bodies. Additionally, more sprouts were observed in the Northern and Western parts while the other classes showed a consistency and steady change.

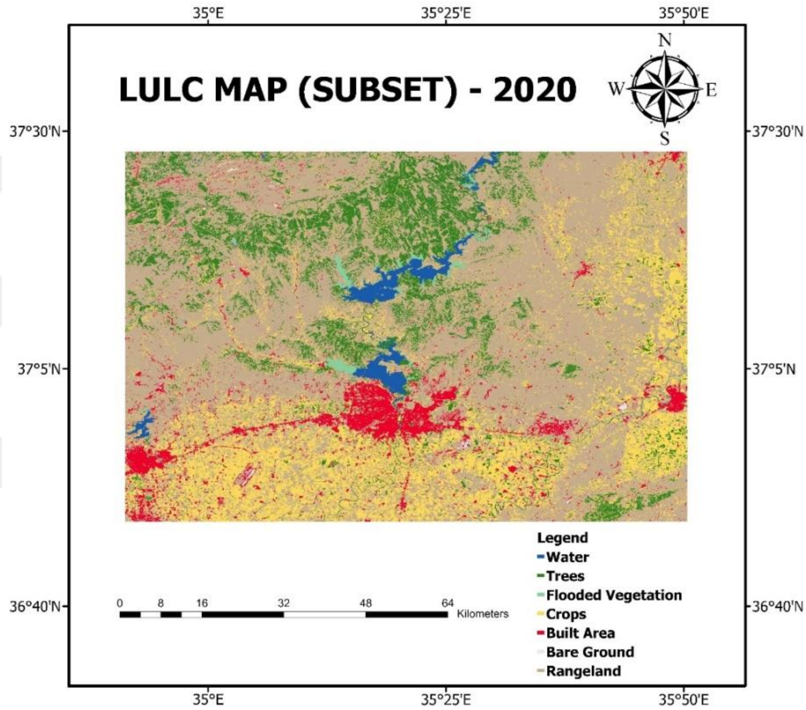

Figure 4.40 LULC Map (Subset) of Adana Province in 2020

In 2020, however, when compared to 2018 and 2019 also saw similar changes in the land cover classes. Water had an area of 104.88 square kilometers, Trees an area of 641.92 square kilometers, Flooded Vegetation an area of 40 square kilometers, Crops with an area of 1167.95 square kilometers, Built Area an area of 353.93 square kilometers, while Bare Ground had 12.83 square kilometers and Rangeland with 3974.93 square kilometers. In addition, it was visually challenging comparing the maps with classes such as Trees which saw a gradual reduction in the Northern and Western regions as shown on Figure 4.40. Additionally, the same was also observed for Crops in the Eastern and Southern regions as compared to the two previous years.

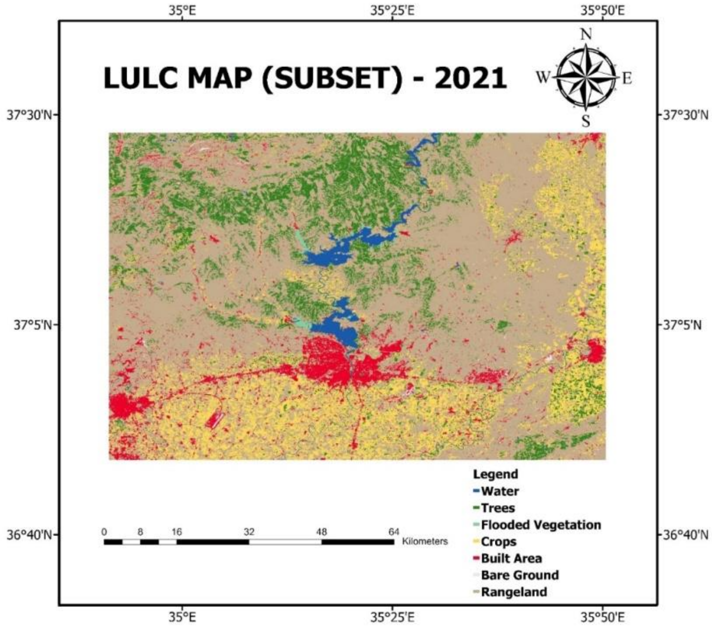

Figure 4.41 LULC Map (Subset) of Adana Province in 2021

2021, had more intriguing visual changes compared to 2020. Flooded Vegetation greatly reduced in the central water bodies as shown in Figure 4.41. Additionally, areas such as Crops also continued reducing in number from the Southern and Eastern parts when compared to the previous years. Water had an area of 109.09 square kilometers, Trees an area of 676.42 square kilometers, Flooded Vegetation an area of 19.98 square kilometers, Crops with an area of 1024.59 square kilometers, Built Area an area of 362.28 square kilometers, Bare Ground an area of 15.02 square kilometers and Rangeland with 4095.32 square kilometers. The other classes showed a consistent change over the period of time to give an insight in the LULC over time.

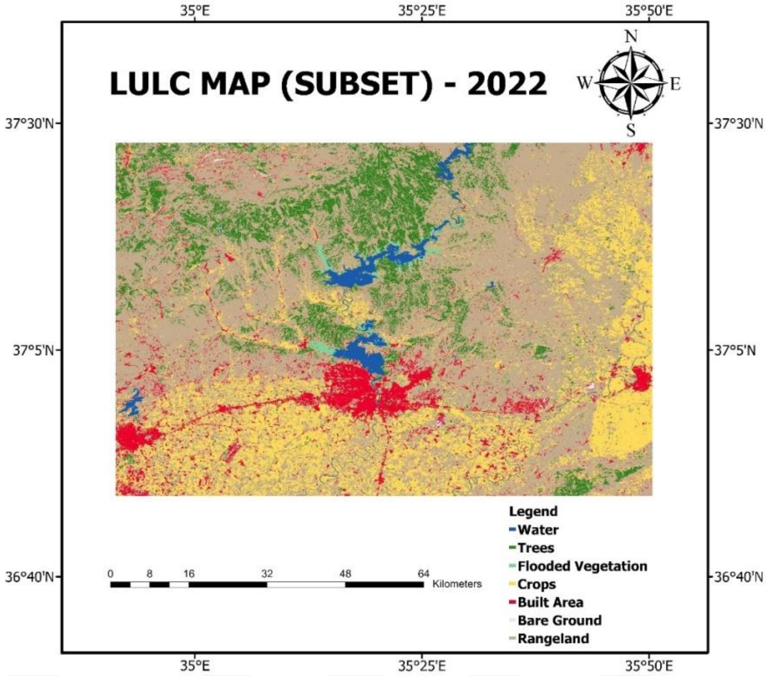

Figure 4.42 LULC Map (Subset) of Adana Province in 2022

Finally, 2022 as shown in Figure 4.42 saw changes in the distribution of trees in the central parts as compared to 2021 representing a reduction. Furthermore, more Built Areas were sprouted in the Southern region combined with Croplands as visually seen on the map. The eastern parts also saw an increase in Crops compared to the previous year of 2021. The other classes however, continued portraying a consistency in the change of classes as also verified in the area values given in Table 4.16. Water had an area value of 105.70 square kilometers, Trees an area value of 669.36 square kilometers, Flooded Vegetation recorded 43.16 square kilometers, Crops also a value of 1165.77 square kilometers, while Built Area had a value of 382.60 square kilometers, Bare Ground a value of 15.81 square kilometers and Rangeland a value of 3935.04 square kilometers.

Table 4.13 Subset Consumer's Accuracy values for 2018, 2019, 2020, 2021 and 2022

CONSUMER'S ACCURACY (SUBSET)					
CLASS	**2018**	**2019**	**2020**	**2021**	**2022**
Water	1	1	1	1	1
Trees	0.969	0.853	0.941	0.944	0.724
Flooded	1	1	1	1	1
Crops	0.917	0.679	0.933	0.963	0.893
Built Area	0.960	0.909	0.918	0.909	0.914
Bare Ground	0.625	1	0.333	0.857	1
Rangeland	0.882	0.909	0.842	0.842	0.793

The consumer accuracy values for the subset were compared to the values of the main study area to analyze the change in accuracy. It was noted that most classes of the subset showed higher values in Table 4.13 compared to Table 4.9 of the main study area. Classes easy to classify such as Water maintained an accuracy value of 100% in all the years on both the subset and main study area. Trees in 2018 for the subset increased to 96.9% from the previous 88.9% of the main study area in the same year. 2019 and 2022 however, showed a decrease in consumer accuracy in the subset with values of 85.3% and 72.45 compared to 87.55 and 100% in 2022 for the main study area. Overall other years such as 2020 and 2021 showed an increase in the values from 93.8% and 91.3% to 94.1% and 94.4% showcasing an improvement in the obtained results.

Flooded Vegetation like Water also showed a consistency in accuracy as the main study area with an accuracy of 100% over the five-year period, indicating a precise identification of the pixels. Furthermore, Crops also showed a tremendous improvement in the consumer accuracy in the years 2018, 2021 and 2022 when compared to the main study area in Table 4.9. 91.7% was recorded from the initial 75% in 2018, while 2021 had 96.3% from 87.5%. Additionally, 2022 also recorded an increase from 81.5% to 89.5% while 2019 and 2020 showed lower values of 67.9% and 93.3% when compared to the main study area.

Built Area however, been the main focus showed an increase in all the five-year period validating the need to obtain a subset for classes with pixels difficult to classify. The year 2018 had 96% from 94.4% from the main study area, while 2019 had 90.9% from 85.7%, furthermore 2020 recorded a consumer accuracy of 91.8% from 80%, 2021 had a value of 90.9% from 76.7% and finally 2022 recorded 91.45 from 75% indicating an improvement in identification of built area pixels.

Bare Ground also showed a similar trend in the consumer accuracy values when compared to the main study area in Table 4.9. However, years such as 2018 and 2020 showed a decrease from 66.7% and 77.8% to 62.5% and 33.3% while 2021 and 2022 showed an increase of 85.7% and 100% from the same 66.7% and 71.4%. 2019 maintained the same consumer accuracy of 100% for both the subset and the main study area. Finally, Rangeland also produced similar accuracy results for all the years as shown in Table 4.13 and when compared to Table 4.9 of the main study area. 2018 had 88.2% a decrease from 82.7%, 2019 had 90.9% from 87%, while 2020 recorded 84.2% from 87.5% and 2021 with 84.2% as a consumer accuracy from 87.3%. The last obtained value was 79.3% a sharp decrease from 91.6% when compared to the main study area in Table 4.9.

Table 4.14 Subset Producer’s Accuracy values for 2018, 2019, 2020, 2021 and 2022

PRODUCER'S ACCURACY (SUBSET)					
CLASS	**2**	**2**	**2**	**2**	**2**
Water	1	1	1	1	1
Trees	0	0	0	0	0
Flooded Vegetation	1	1	1	0	1
Crops	0	0	0	0	0
Built Area	0	0	0	0	0
Bare Ground	0	0	0	0	0
Rangeland	0	0	0	0	0

As also compared to the Producer's Accuracy of the main study area, the class of Water maintained a 100% accuracy for all the years as shown in Table 4.14 indicating a high level of correct classification of water pixels. Trees in 2018 recorded 86.5% from 81.3% while 2019 recorded 85.3% a decrease from 94.4%. 2020 and 2021 also recorded producer accuracy values of 80% and 82.9% from 88.2% and 91.3%. 2022 however, showed a sharp decrease from 87.5% from the main study area to 60% for the subset. Additionally, Flooded Vegetation also followed a similar trend of a 100% accuracy with only changes in the year 2021 for the subset which saw a decrease to 78.6% from 100%.

Crops however, also had similar values as the main study area. 2018 and 2019 had values of 71% and 73.1% a decrease from 74.2% and 80%. Similarly, 2020 and 2021 recorded 82.4% and 76.5% an increase from 76.5% and 70% from the main study area. Finally, 2022 recorded 75.8% a decrease compared to 95.7% as shown in Table 4.10. Built Area also showcased an increase in the producer accuracy values for all the years as compared to the main study area in Table 4.10. 2018 and 2019 recorded the highest with 94.1% and 96.2%, respectively, from 64.5% and 66%. 2020 recorded the least with 84.9% from 80% while 2021 had 89.3% from 63.9%. Finally, 2022 recorded a producer accuracy of 86.9% a tremendous increase from 72.4% when compared to the main study area.

In addition, Bare Ground also saw similar changes in the Producer Accuracy values, 2018 recorded 83.3% an increase from 33.3%, 2019 had 66.7% an increase also from 20%. 2020 however, recorded a sharp decrease of 33.3% from 77.8% as shown in Table 4.14. Lastly, 2021 and 2022 recorded values of 75% and 60% as compared to 66.7% and 71.4% of the main study area. Rangeland however, as also compared to values in Table 4.10 remained consistent with values over 90% showcasing a high level of correct classification of pixels.

2018 had a value of 95.7% compared to 93.2%, 2019 recorded 91% a decrease from 94% from the main study area. 2020 and 2021 however, both recorded an increase in values with 94.1% and 95.9% from 93.3% and 94.4%, respectively, while 2022 had a value of 91.5% compared to 90.2% of the main study area.

Table 4.15 Subset Overall Accuracy and Kappa Static values for 2018, 2019, 2020, 2021 and 2022

Year	OVERALL ACCURACY (%)	KAPPA STATISTIC (%)
2018	0.91	0.88
2019	0.88	0.85
2020	0.90	0.84
2021	0.89	0.86
2022	0.85	0.80

When compared to the Overall Accuracy and Kappa Statistic of the main study area in Table 4.11, it was observed that a similar trend in values was obtained for the subset with minor differences in some years indicating the accuracy and truthfulness of the classification for the main study area and subset. 2018 had an overall accuracy of 91% and Kappa Statistic of 88% as shown in Table 4.15 when compared to 85% and 86% of Table 4.11. Similarly, 2019 recorded 88% as the overall accuracy and 85% as the Kappa Statistic while the main study area had 86% and 81%, respectively. Furthermore, 2020 recorded the same overall accuracy value of 90% for both the subset and main study area with a difference in the Kappa Statistic from 85% in Table 4.11 to 84% in Table 4.15 indicating a slight decrease. 2021 recorded an overall accuracy of 89% and Kappa Statistic of 86% as also contrasted from Table 4.11 which had values of 85% and 83%, respectively. Finally, 2022 recorded an overall accuracy of 85% and Kappa Statistic of 80% a decrease when compared to the main study area values of 89% and 83%.

Table 4.16 Area values in square kilometers for 2018, 2019, 2020, 2021 and 2022

AREA (SQKM) SUBSET					
CLASS	**2018**	**2019**	**2020**	**2021**	**2022**
Water	120.18	103.89	104.88	109.09	105.70
Trees	746.20	721.47	641.92	676.42	669.36
Flooded Vegetation	15.51	65.91	40.46	19.98	43.16
Crops	1217.22	1357.45	1167.95	1024.59	1165.77
Built Area	325.28	331.62	353.93	362.28	382.60
Bare Ground	14.47	13.51	12.83	15.02	15.81
Rangeland	3862.99	3709.03	3974.93	4095.32	3935.04

As a comparison to the main study area in Table 4.12, the main area values for the subset were also analyzed as shown in Table 4.16. The main purpose was to articulate the accuracy and analyze the trend in change of the values over the five-year period. The class for Water showcased a fair consistency and trend over the years. The recorded area value for 2018 was 120.18 square kilometers, in 2019 was 103.89 square kilometers a gradual increase from 2018. 2020 however, recorded 104.88 square kilometers while 2021 had 109.09 square kilometers a tremendous increase from the previous years and the highest values when compared to all the years. Finally, 2022 had 105.70 square kilometers showcasing a decrease from the previous year.

Furthermore, Trees also showcased a similar trend with the year 2018 showing the highest value of 746.20 square kilometers as shown in Table 4.16. 2019 also recorded a value of 721.47 square kilometers a decrease from the previous year while 2020 also showed a decrease of 641.92 square kilometers compared to the two years. In addition, 2021 and 2022 showed an increase from the area value recorded in 2020. 2021 recorded 676.42 square kilometers while 2022 recorded a value of 669.36 square kilometers showcasing the trend change in values.

Flooded Vegetation, however, recorded 15.51 square kilometers in 2018 and 65.91 square kilometers in 2019 a drastic increase which can have been attributed to factors such as misclassification or mixed pixels or sudden changes in the climate conditions for 2019 in the study area. To add on, 2020 also recorded an area value of 40.96 square kilometers a 20 square kilometer change from 2019 while 2021 had recorded a decrease to 19.98 square kilometers. Finally, 2022 recorded an increase of 43.16 square kilometers from the initial 19.98 square kilometers obtained. Crops like water showed a consistency and trend in the change of values with less to minimal changes over the study period. 2019 recorded an area of 1357.45 square kilometers a slight increase from 2018. 2020 however, saw a decline in the area value of 1167.95 square kilometers when compared to the previous years. The decline further went on 1024.59 square kilometers in 2021 and 1165.77 square kilometers in 2022.

Built Area been the main focus of analyzing the trend and changes in LULC in the subset saw a steady change overtime. However, to obtain the values the algorithm was run several times in the Earth Engine to obtain an acceptable trend that was used for this study. 2018 recorded 325.28 square kilometers, 2019 a value of 331.62 square kilometers and 2020 an increase of 353.93 square kilometers. Furthermore, the area value went on to increase from 353.93 square kilometers in 2020 to 362.28 square kilometers in 2021. As 2022 being the last year, it was expected to have the highest value of Built Area with an initial value of 382.60 square kilometers validating the expected results.

Like Water and Flooded Vegetation, Bare Ground also recorded a change with 2018 recording a value of 14.47 square kilometers while 2019 recorded 13.51 square kilometers. Furthermore, 2020 had a value of 12.83 square kilometers a reduction from the values obtained from the two previous years. 2021 and 2022, however, recorded the highest values with areas of 15.02 square kilometers and 15.81 square kilometers. Finally, the last classified class was Rangeland with values of 3862.99 square kilometers in 2018 and 3709.03 square kilometers in 2019 while 3974.93 square kilometers was recorded in 2020. 2021 however, recorded the highest value of 4095.32 square kilometers as opposed to the previous 3 years and 2022 which also saw a drop in Rangeland to 3935.04 square kilometers as shown in Table 4.16.

4.5. Change Detection

This chapter will closely analyze the results and provide information in changes between the classes of both the main study area and subset for practical comparison. The change detection between the main study area and the subset is to understand the differences in LULC characteristics and specific changes that might have occurred within the selected subset and study area. Analyzing the results from both is essential in understanding the key knowledge of how land cover types that are difficult to classify such as Built Area, Crops and Bare Ground change over time. A subset analysis allowed for a more in-depth interpretation of the changes within the study area. It enabled an understanding of the factors driving the observed changes, such as land use patterns, human activities or natural phenomena and their implications within that particular context. Key land cover areas such as Built Area, Crops and Bare Ground were a focus in the subset to better highlight and get accurate results needed for the study. By combining results from the main study area and subset it was easier and clear to interpret the changes and underline the difficulties related to LULC classification.

To perform a change detection, the percentage change of each class from 2018 to 2022 for both the main study area and subset was compared and calculated using the following formula;

$$\% \, change = \frac{(value \; current \; year - value \; previous \; year)}{value \; previous \; year} * 100 \tag{4.1}$$

For example, for the Water class in the main study area between 2018 and 2019, the % change can be written as $(137.38 - 103.35)/103.35 * 100$ equals to 32.92%. Similarly, for the water class in the subset between 2018 and 2019, the % change is $(103.89 - 120.18)/120.18 * 100$ equals to -13.54%. Table 4.17 and Table 4.18 below illustrate the change in percentage information for both the main study area and Subset;

Table 4.17 Change in LULC (Study Area) Values

CHANGE IN LULC (Main Study Area)					
CLASS	**2018-2019**	**2019-2020**	**2020-2021**	**2021-2022**	**2018-2022**
Water	+32.92%	-0.82%	-13.16%	+9.75%	+25.64%
Trees	+42.86%	-4.88%	-11.67%	+0.15%	+20.18%
Flooded	-6.06%	-25.86%	+10.67%	+25.00%	-3.60%
Crops	+0.91%	-2.01%	+13.64%	+7.45%	+20.76%
Built Area	+1.52%	+18.99%	+0.34%	+1.45%	+22.99%
Bare	+14.58%	-9.47%	-14.90%	-34.62%	-42.67%
Rangeland	-18.81%	-7.80%	-1.44%	-4.33%	-17.71%

Table 4.18 Change in LULC (Subset) Values

CHANGE IN LULC (SUBSET)					
CLASS	**2018-2019**	**2019-2020**	**2020-2021**	**2021-2022**	**2018-2022**
Water	-13.54%	+0.95%	+4.01%	-3.10%	-12.02%
Trees	-3.31%	-11.02%	+5.37%	-1.04%	-10.31%
Flooded Vegetation	+324.98%	-38.58%	-50.63%	+115.91%	+178.33%
Crops	+11.53%	-13.96%	-12.29%	+13.78%	-4.23%
Built Area	+1.94%	+6.73%	+2.36%	+5.61%	+17.61%
Bare Ground	-6.63%	-5.04%	+17.05%	+5.26%	+9.25%
Rangeland	-3.98%	+7.17%	+3.03%	-3.91%	+1.86%

The main study area and Subset region showed different trend of change in the area of different classes from 2018 to 2022 as shown in Table 4.16 and Table 4.17, respectively. The main study area saw an increase in Water, Trees, Crops and Built Area classes, with the largest rise occurring from 2018 to 2019 for Water and Trees, from 2020 to 2021 for Crops and from 2019 to 2020 for Built Area. The main study area also saw a decrease in Flooded Vegetation and Bare Ground classes, with the largest drop occurring from 2019 to 2020 for Flooded Vegetation and from 2021 to 2022 for Bare Ground. Furthermore, the main study area saw a decrease in Rangeland class, with the largest decline occurring from 2018 to 2019.

The Subset area experienced more changes in Water, Trees and Flooded Vegetation classes than the main study area, while the main study area experienced more changes in Crops, Built Area and Bare Ground classes than the Subset area. The Subset area saw a decrease in Water and Trees classes, with the largest drop occurring from 2018 to 2019 for Water and from 2019 to 2020 for Trees. The Subset area also saw an increase in Flooded Vegetation class, with the largest rise occurring from 2018 to 2019. The Subset area also saw a slight decrease in Crops class, with the largest fall occurring from 2019 to 2020 and from 2020 to 2021. In addition, the Subset area showed an increase in Built Area and Bare Ground classes, with the largest growth occurring from 2019 to 2020 for Built Area and 2020 to 2021 for Bare Ground. A slight increase in Rangeland class was also recorded, with the largest increase occurring from 2019 to 2020.

The Subset area had more fluctuations in the percentage change of Water, Trees and Flooded Vegetation classes than the Main Region area, while the Main Region area had more fluctuations in the percentage change of Crops, Built Area and Bare Ground classes than the Subset area.

Overall, as it was extremely complicated to analyze the change in area for each year due to irregularities that might have had occurred and were not known to the user and because of the shortest amount taken for a yearly basis to observe or acquire major changes, the overall change from 2018 to 2022 was put into consideration as a last resort to analyze changes for a 5-year period. The main study saw an increase in Water, Trees, Crops and Built Area classes, with Water and Built Area having the largest percentage change of +25.64% and +22.99%, respectively. The main study also saw a decrease in Flooded Vegetation, Bare Ground and Rangeland classes, with Bare Ground having the largest percentage change of -42.67%. The main study had experienced more changes in Crops, Built Area and Bare Ground classes than the subset.

The subset also saw a decrease in Water and Trees classes, with Water having the largest percentage change of -12.02%. The subset has also seen an increase in Flooded Vegetation, Built Area and Bare Ground classes, with Flooded Vegetation having the largest percentage change of +178.33%. The subset had a slight decrease in Crops class and a slight increase in Rangeland class. The subset had experienced more changes in Water, Trees and Flooded Vegetation classes than the main study.

4.5.1. Problems Related to Change Detection

The change detection for that study showed common errors. Some values in the change matrix were not realistic. For example, the percentage change rate of +42.86% recorded for Trees in the same period of 2018 to 2019 of the main study area shown in Table 4.16. As stated, before and by other researchers the accuracy depends on the classified images. If a class is wrongly classified, this will result in a false information. Despite high classification accuracies, there were several false interpretations that were caused by misclassifications. Different data sources may have different resolutions, frequencies, spatial and temporal extents, and data quality hence making it very difficult to acquire the right datasets for the study. Additionally, dealing with noise, errors, and uncertainties in the data and the results that may arise from various sources, such as sensor errors, atmospheric effects, geometric distortions, radiometric corrections, cloud cover, shadows, or classification errors may affect the quality and reliability of the data and the results hence giving irregularities in some classes and change detection values as mentioned above. The other point that should be taken into account is the subset area a small portion of the main study area resulting in different area of classes.

However, using more advanced data sources or higher resolution data to capture more details or variations of the changes can significantly improve the change detection and capture all spatial details.

4.6. Ground Truth Data

In this section, the ground truth data is given from Google Earth Engine for the selected sample locations for the classes Water, Built Area, Crops and Flooded Vegetation for the year interval of 2018 to 2022 with reference to the classified dataset from 2022 shown in (Figure 4.43) which is given to have an understanding of the classified information provided for the study period.

Ground Truth Data is crucial and a necessity in validating and corroborating the classified information obtained through remote sensing and classification processes. By thoroughly comparing the classified data with ground truth data sourced from platforms such as Google Earth Engine (GEE) used for our study, researchers, analysts and scientist can easily assess the reliability and precision of the classification results.

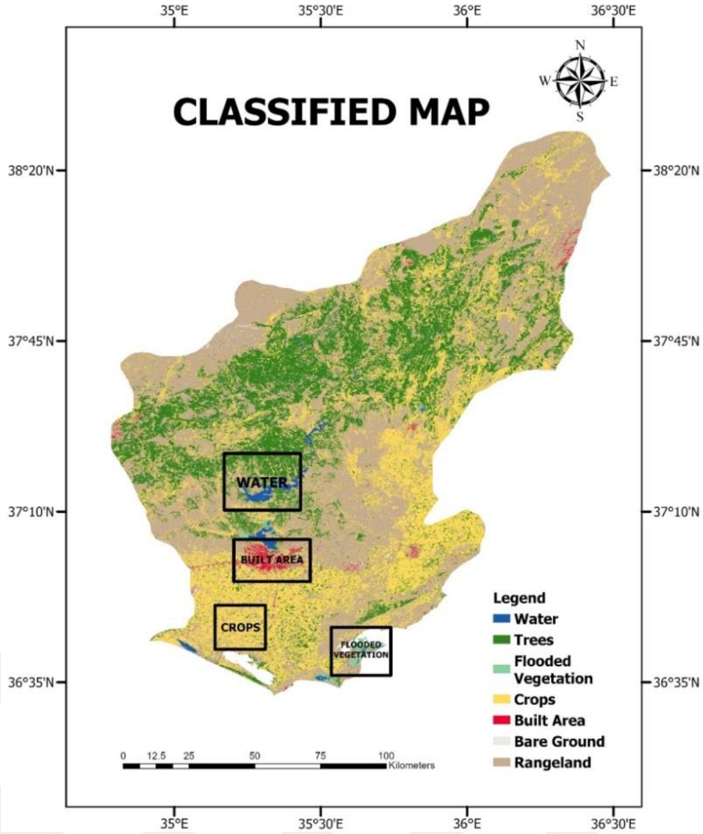

Figure 4.43 Classified Map of Adana

By thoroughly comparing the classified data with ground truth data sourced from platforms such as GEE used for our study, researchers, analysts and scientists can easily assess the reliability and precision of the classification results. The visual comparison is usually done between a classified map such as the one on Figure 4.43 with a high resolution RGB true image referenced from a platform of choice as GEE in our case. The classified information and the actual land cover conditions observed from all the classes involved on the RGB imagery are verified and validated prior to the acceptance of the classification results.

In addition to the validation process, ground truth data also plays a pivotal role in improving the classification algorithms. By analyzing the instances where the classification results diverge from the ground truth data, researchers can gain insights into the limitations of their current algorithms. This could lead to the development of more sophisticated algorithms that can handle complex scenarios, improve classification accuracy, and reduce errors.

Moreover, ground truth data acts as a quality control measure, detecting errors or biases in the classification process. Accurate classification, validated against ground truth, not only supports informed decision-making in diverse fields but also enhances the scientific credibility of research and studies utilizing classified information. Overall, it fosters continuous improvement in classification methodologies, ensuring dependable and precise interpretations of satellite imagery.

Lastly, ground truth data is not static but evolves over time. As landscapes change due to natural processes or human activities, the ground truth data must be updated to reflect these changes. This dynamic nature of ground truth data underscores the need for continuous data collection and updating. It also highlights the importance of platforms like Google Earth Engine, which provide access to timely and updated satellite imagery. Thus, ground truth data is not just a tool for validation and improvement, but an ongoing commitment to accuracy and relevance in the field of remote sensing and classification.

Figure 4.43 shows the classified map of Adana used as a reference for the comparison with Ground Truth Data obtained from GEE. Four (4) distinct classes were selected from the classified dataset as Water, Built Area, Crops and Flooded Vegetation. Each class was closely analyzed and further visualized for actual information to confirm the authenticity of the class on GEE obtained Ground Truth Data.

The obtained classes in terms of distinct polygons were taken as RGB images from Google Earth Engine and each with selected observation polygons shown in red circles on Figure 4.44 to Figure 4.63. The observation polygons were drawn to show key changes in the classes and as a guide to show the changes over the period of time from 2018 to 2022.

The observation polygons showed clear changes over the years and illustrated changes that had taken into effect for the classes as a way to validate information from the classified datasets.

Figure 4.44 Water Map of Adana (2018)

Figure 4.45 Water Map of Adana (2019)

Figure 4.46 Water Map of Adana (2020)

Figure 4.47 Water Map of Adana (2021)

Figure 4.48 Water Map of Adana (2022)


Figure 4.49 Built Area Map of Adana (2018)


Figure 4.50 Built Area Map of Adana (2019)


Figure 4.51 Built Area Map of Adana (2020)

Figure 4.52 Built Area Map of Adana (2021)

Figure 4.53 Built Area Map of Adana (2022)

Figure 4.54 Crops Map of Adana (2018)


Figure 4.55 Crops Map of Adana (2019)


Figure 4.56 Crops Map of Adana (2020)


Figure 4.57 Crops Map of Adana (2021)

Figure 4.58 Crops Map of Adana (2022)

Figure 4.59 Flooded Vegetation Map of Adana (2018)

Figure 4.60 Flooded Vegetation Map of Adana (2019)


Figure 4.61 Flooded Vegetation Map of Adana (2020)


Figure 4.62 Flooded Vegetation Map of Adana (2021)


Figure 4.63 Flooded Vegetation Map of Adana (2022)

Figure 4.44 to Figure 4.48 show the Ground Truth Data of Water a selected sample polygon obtained from the classified image as a reference and further processed in Google Earth Engine to give a comprehensive analysis and validation of the accuracy in relation to real features of classes in both the classified imagery and imagery used as ground truth data. The Sentinel 2 imagery with a resolution of 10 m was used as a reference for ground truth data as it is able to capture all the fine details of the Earth's surface, enabling precise identification and delineation of land cover classes. Furthermore, as it is openly accessible on Google Earth Engine platform, it allows researchers, analysts and practitioners to retrieve data without financial constraints, promoting a wider usage and analysis.

The water polygon drawn on Figure 4.43 on the Classified Map of Adana was closely analyzed with reference from images obtained from 2018 to 2022 of the same polygon and area as shown on Figure 4.44 to Figure 4.48. Water features were validated to be accurately classified in all the datasets from the 5-year interval as shown in blue color on Figure 4.43. The observed classes in terms of polygons were taken as RGB images from Google Earth Engine and each with selected observation polygons shown in red circles on Figure 4.44 to Figure 4.63. The observation polygons were drawn to show key changes in the classes and as a guide to show the changes over the period of time from 2018 to 2022. The observation polygons showed clear changes and illustrated changes that had taken effect to validate information from the classified datasets.

However, as the study was conducted over consecutive concurrent years it was tricky to fully see large changes in the classes. With the help of drawn observation polygons, it was easier to observe the trend in changes. Upon comparison of Figure 4.44 and Figure 4.45 it was observed that water appeared bluer in the edges and middle parts. Furthermore, more Trees were observed in Figure 4.45 than in Figure 4.44. Figure 4.47 also showed more bare land in the northern observation polygons than all the other figures. Figure 4.48 and Figure 4.46 also showed similar changes with both showing more Trees and Cropland.

Built Area however, as shown from Figure 4.49 to Figure 4.53 was also referenced as Water. A distinct polygon was obtained from the classified image dataset and labeled Built Area as shown on Figure 4.43. It was also observed that Built Area was classified accurately for the interval from 2018 to 2022 as shown in red color on Figure 4.43 in relation to Ground Truth Data obtained from Google Earth Engine. When Built Area polygons were analyzed, Figure 4.49 and Figure 4.50 showed class differences, with Figure 4.50 showing more cleared lands in the bigger observation polygon and more croplands in the northern and southern parts. Additionally, it was also observed that the bridge constructed was progressing in both figures as shown in the smallest observation polygon. When Figure 4.51 and Figure 4.52 were contrasted, Figure 4.52 showed more cleared land and built-up areas in the observation polygons. Furthermore, the bridge could be seen at an advanced stage in the smaller observation polygon in Figure 4.52 than Figure 4.51. Lastly, Figure 4.53 representing the year 2022 showed more Built up areas and cleared land than all the other figures and was evidently observed that the bridge construction was near completion as shown in the smallest observation polygon.

To add on, the third obtained sample polygon from the classified image dataset was Crops as shown in Figure 4.43. Five separate samples from the year 2018, 2019, 2020, 2021 and 2022 were obtained from Google Earth Engine as shown on Figure 4.54 to Figure 4.58 in reference to the drawn polygon on the classified dataset. It was also observed that crops were accurately classified in all the years for the study interval. Crops were also put into consideration to observe the changes. Figure 4.55 representing 2019 showed a different pattern of crop structure and cultivated fields when contrasted with Figure 4.54 through the observation polygons. Figure 4.57 for 2021, also showed a different part when compared to Figure 4.56 and Figure 4.55. Figure 4.57 showed more areas with structures shown in white referring to greenhouses for agriculture. Furthermore, 2021 also showed a different pattern in the crops and cultivated land when compared to the other years. Lastly, Figure 4.58 depicting 2022 showed more built-up structures shown in white validating the technological advancement of agriculture in the region which requires more intensive and mechanized method such as greenhouses.

Finally, the last obtained polygon was for Flooded Vegetation as shown on the classified map on Figure 4.43 and was also accurately classified as shown in blue color. Areas classified as Flooded Vegetation were easily seen in the Figures 4.59 to Figure 4.63 validating the results to be true. Furthermore, distinct observation polygons were also drawn to give an insight in the changes and differences between years. The observation polygons in Figure 4.60 were different from Figure 4.59. Figure 4.59 showed more darker areas in the largest observation polygon than Figure 4.60 while Figure 4.62 showed more darker flooded vegetation regions than Figure 4.61. Other areas observed to be different were bareland and crop areas in the polygon. Lastly, Figure 4.63 looked more familiar with Figure 4.61 with lighter flooded vegetation regions and more bareland as could be seen on the maps. Darker and lighter conditions to the appearance of the flooded vegetation regions can be attribute to factors such as vegetation density, vegetation type and water content. Due to high concentration of vegetation areas with denser vegetation appear to be darker as light and sunshine is blocked, while vegetation type affects the results in the essence that dense forests or thick vegetation absorb more light, resulting in darker areas on the map, while lighter vegetation, such as grasslands or shrubbery, reflect more light and appear lighter on the maps. In addition, areas with higher water content in the vegetation may appear darker due to increased absorption of light.

It was therefore stated that from the training samples given as shown below in Figure 4.64 for the Training Sample Map of Adana and Figure 4.65 of the Subset Training Sample Map of Adana, the obtained classified datasets for both the main study area and subset were validated to be accurately classified.

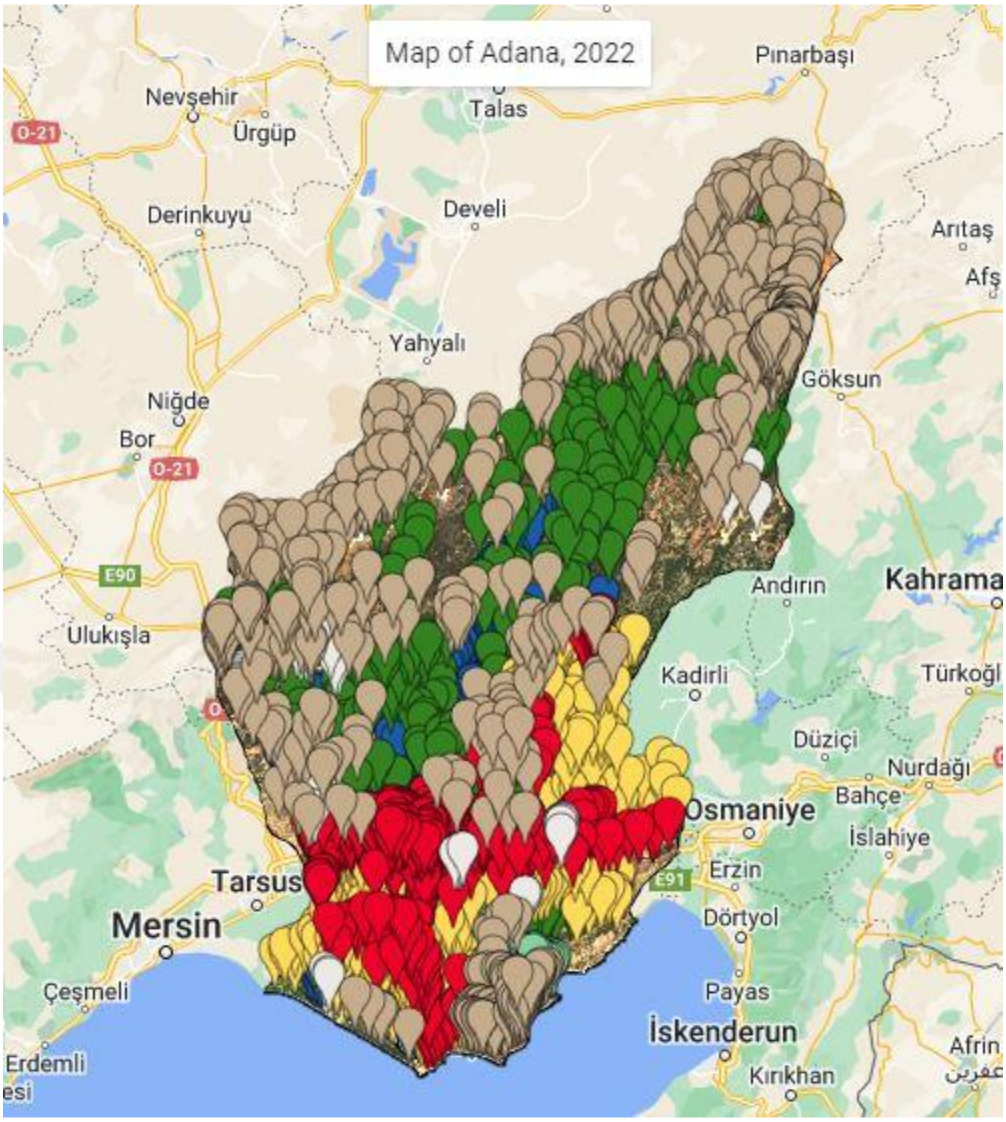

Figure 4.64 Training Sample Map of Adana

Figure 4.64 shows the geometry inputs used as training samples for the study area. A total of 2687 training points were scattered over the whole study area to maximize and get clear accurate results of the classified classes. Water was defined by blue color with a total of 189 training points, Trees in green color with a total of 287 training points, Flooded Vegetation in light green color with a total of 104 training points, Crops in yellow color with 401 training points, Built Area in red color with 618 training points, while Bare Ground in white color had 78 training points as the lowest and Rangeland in grey color with the highest training points of 1010.

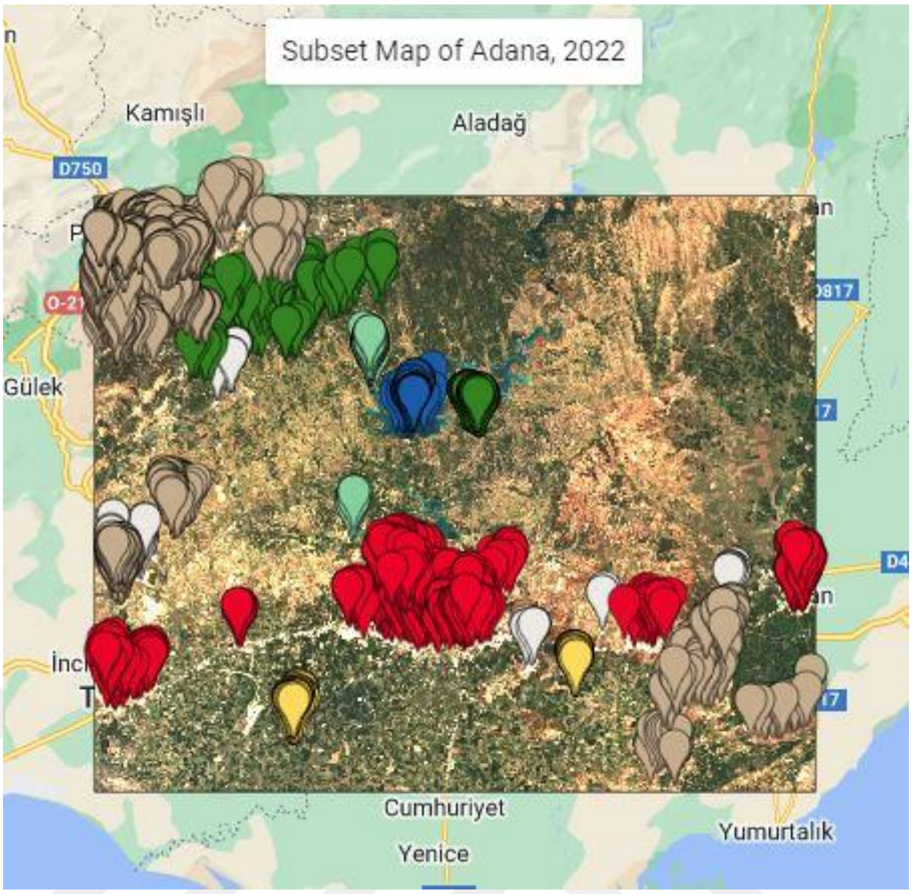

Figure 4.65 Subset Training Sample Map of Adana

The same was also certain for the subset region shown in Figure 4.65 showcasing the training sample points. A total of 2929 training points were also spread on the subset region to capture all the classes. The class Water assigned with blue color had 197 training points, Trees assigned with green color had 382 training points, Crops with yellow color was assigned with 297 training points, Rangeland assigned with grey color was given 1153 training points, Bare Ground assigned with white was given 70 training points while Flooded Vegetation assigned with light green color was given 90 training points and finally Built Area with red color was given 543 training points. To define the training data as previously explained in the sub chapter 3.2.3.1.6, the training data was split into 90% of the total training samples as a trainset and 10% of the total as test set for the Random Forest Classifier in Google Earth Engine. It's crucial to note that the effectiveness of the classification process is heavily dependent on the quality and distribution of these training points. The selection of training points is also a critical in the classification process which is also followed by validation from the Ground Truth Data to access the accuracy of obtained results.

5. CONCLUSION

Despite these intriguing findings, it's crucial to acknowledge the limitations and challenges faced during the study process. The study revealed anomalies in some percentage change values, suggesting potential misclassifications and errors in the classification process. Such inaccuracies can arise from various sources as explained in the previous chapter. Additionally, as the study was limited to the usage of Sentinel- 2 imagery with a resolution of 10 m, it would be advisable to use a more high-resolution dataset for the study to cater for the confusion in classification of certain classes and pixels. The Exploration of advanced data sources and higher-resolution imagery to capture finer details of land cover changes and enhance the reliability of results can be considered as one of the first and vital steps in obtaining accurate results.

Additionally, incorporating ground truth data into an analysis is critical and helps in validating the results with field surveys and ground-based measurements thereby adding a layer of confidence to the results. Unfortunately, taking accurate ground truth data across the whole study region can be problematic if the area is large. Error correction is another crucial step that classification involves. Identifying and rectifying errors and outliers in results through visual inspection and error correction procedures differs by user experience, a more professional GIS expert is likely to perform a better post classification analysis compared to a regular user.

The findings and results of the study provide valuable insights into the dynamic changes in land cover classes within both the main study area and the subset region over a five-year period from 2018 to 2022. Notably, these two geographical regions exhibited distinct patterns of change, shedding light on the complex interplay of environmental factors and human activities within each area. The observed variations in land cover changes between the main study area and the subset region emphasize the significance of conducting localized assessments and monitoring efforts. These findings underscore the need for region-specific land management strategies and policies to address the diverse environmental challenges and human activities that contribute to these changes. Additionally, the disparities in land cover changes within the two areas highlight the importance of tailored conservation and restoration efforts, taking into account the unique characteristics and drivers of change in each region.

Furthermore, the study serves as a reminder of the complexities and potential uncertainties inherent in classification and change detection analyses, particularly when relying on remote sensing data and classification processes. The discrepancies and anomalies identified in some percentage change values underscore the importance of rigorous research to find practical accurate methods of improving all remote sensing-based studies, including new post-classification methods and quality control procedures. Researchers and practitioners should exercise caution when interpreting results and consider the possibility of misclassifications and errors, especially when dealing with abrupt and extreme changes that may not align with the expected patterns.

The quest for identifying the best methods for image classification and analysis remains an ongoing challenge in the fields of remote sensing and machine learning. Despite extensive research efforts, a singular, universally applicable best method has not emerged. This lack of a one-size-fits-all solution can be attributed to several key factors. One of the primary reasons for the diversity of image classification methods is the wide range of data and applications within this domain. Images can originate from various sources, including satellite imagery each presenting unique challenges and opportunities for classification. The method that proves effective for one type of data or application may not necessarily perform optimally for another.

Furthermore, the complexity of image features further complicates the search for the best classification method. Images contain a multitude of features, often at different scales, resolutions, and levels of detail. Developing algorithms capable of effectively capturing these diverse features across different domains and contexts is inherently challenging. Algorithm complexity is another factor to consider. While more complex methods, such as deep learning models, have achieved state-of-the-art results, they require substantial computational resources and large datasets. Simpler methods may offer computational efficiency but might not reach the same level of accuracy. The complexity of image features further complicates the search for the best classification method. Images contain a multitude of features, often at different scales, resolutions, and levels of detail. Developing algorithms capable of effectively capturing these diverse features across different domains and contexts is inherently challenging.

Looking forward, this study lays the groundwork for future research endeavors and monitoring initiatives aimed at gaining a deeper understanding of the dynamics of land cover changes over time in similar regions and globally. The integration of higher-resolution data sources, advanced machine learning algorithms, and improved classification techniques can contribute to more accurate and reliable analyses. Additionally, ongoing efforts to enhance data quality, consistency, and accessibility will be instrumental in facilitating comprehensive and timely assessments of land cover changes, thus supporting evidence-based decision-making in environmental management and sustainable land use planning.

REFERENCES

Achard, Frédéric, and Matthew C Hansen. 2012. *Global forest monitoring from earth observation* (Taylor & Francis).

Akyürek, D, Ö Koç, EM Akbaba, and F Sunar. 2018. 'Land use/land cover change detection using multi–temporal satellite dataset: A case study in Istanbul new airport', *The International Archives of the Photogrammetry, Remote Sensing and Spatial Information Sciences*, 42: 17-22.

Alam, Akhtar, M. Sultan Bhat, and M. Maheen. 2020. 'Using Landsat satellite data for assessing the land use and land cover change in Kashmir valley', *GeoJournal*, 85: 1529-43.

Alphan, Hakan, and K. Tuluhan Yilmaz. 2005. 'Monitoring Environmental Changes in the Mediterranean Coastal Landscape: The Case of Cukurova, Turkey', *Environmental Management*, 35: 607-19.

Antrop, Marc. 2004. 'Landscape change and the urbanization process in Europe', *Landscape and urban planning*, 67: 9-26.

Breiman, Leo. 2001. 'Random forests', *Machine learning*, 45: 5-32.

Chapin Iii, F Stuart, Erika S Zavaleta, Valerie T Eviner, Rosamond L Naylor, Peter M Vitousek, Heather L Reynolds, David U Hooper, Sandra Lavorel, Osvaldo E Sala, and Sarah E Hobbie. 2000. 'Consequences of changing biodiversity', *Nature*, 405: 234-42.

Congalton, Russell G, and Kass Green. 2019. *Assessing the accuracy of remotely sensed data: principles and practices* (CRC press).

Das, Sandipta, and Dasharatha P Angadi. 2020. 'Land use-land cover (LULC) transformation and its relation with land surface temperature changes: A case study of Barrackpore Subdivision, West Bengal, India', *Remote Sensing Applications: Society and Environment*, 19: 100322.

Dash, Prasanjit, F-M Göttsche, F-S Olesen, and Herbert Fischer. 2002. 'Land surface temperature and emissivity estimation from passive sensor data: Theory and practice-current trends', *International journal of Remote sensing*, 23: 2563-94.

del Mar López, Tania, T Mitchell Aide, and John R Thomlinson. 2001. 'Urban expansion and the loss of prime agricultural lands in Puerto Rico', *Ambio: a Journal of the Human environment*, 30: 49-54.

Diouf, A, and EF Lambin. 2001. 'Monitoring land-cover changes in semi-arid regions: remote sensing data and field observations in the Ferlo, Senegal', *Journal of Arid Environments*, 48: 129-48.

Ettehadi Osgouei, Paria, Sinasi Kaya, Elif Sertel, and Ugur Alganci. 2019. 'Separating built-up areas from bare land in mediterranean cities using Sentinel-2A imagery', *Remote Sensing*, 11: 345.

Faruque, Md Jamal, Zoltan Vekerdy, Md Yeasir Hasan, Kamal Ziaul Islam, Beverly Young, Mohammad Tofayal Ahmed, Minhaj Uddin Monir, Shaik Muntasir Shovon, Jannatul Ferdaus Kakon, and Prionti Kundu. 2022. 'Monitoring of land use and land cover changes by using remote sensing and GIS techniques at human-induced mangrove forests areas in Bangladesh', *Remote Sensing Applications: Society and Environment*, 25: 100699.

Genzano, Nicola, Nicola Pergola, and Francesco Marchese. 2020. 'A Google Earth Engine tool to investigate, map and monitor volcanic thermal anomalies at global scale by means of mid-high spatial resolution satellite data', *Remote Sensing*, 12: 3232.

Goetz, Alexander FH, Gregg Vane, Jerry E Solomon, and Barrett N Rock. 1985. 'Imaging spectrometry for earth remote sensing', *science*, 228: 1147-53.

Göksel, Cigdem, and Filiz Bektaş Balçık. 2019. 'Land Use and Land Cover Changes Using Spot 5 Pansharpen Images; A Case Study in Akdeniz District, Mersin-Turkey', *Turkish Journal of Engineering*, 3: 32-38.

Grimm, Nancy B, Stanley H Faeth, Nancy E Golubiewski, Charles L Redman, Jianguo Wu, Xuemei Bai, and John M Briggs. 2008. 'Global change and the ecology of cities', *science*, 319: 756-60.

Hastie, Trevor, Robert Tibshirani, Jerome H Friedman, and Jerome H Friedman. 2009. *The elements of statistical learning: data mining, inference, and prediction* (Springer).

He, Chunyang, Zhifeng Liu, Jie Tian, and Qun Ma. 2014. 'Urban expansion dynamics and natural habitat loss in China: A multiscale landscape perspective', *Global change biology*, 20: 2886-902.

Herold, Martin, Philippe Mayaux, CE Woodcock, A Baccini, and C Schmullius. 2008. 'Some challenges in global land cover mapping: An assessment of agreement and accuracy in existing 1 km datasets', *Remote Sensing of Environment*, 112: 2538-56.

Iban, Muzaffer Can, and Ezgi Sahin. 2022. 'Monitoring land use and land cover change near a nuclear power plant construction site: Akkuyu case, Turkey', *Environmental monitoring and assessment*, 194: 724.

Ikiel, Cercis, Beyza Ustaoglu, Ayse Atalay Dutucu, and Derya Evrim Kilic. 2013. 'Remote sensing and GIS-based integrated analysis of land cover change in Duzce plain and its surroundings (north western Turkey)', *Environmental monitoring and assessment*, 185: 1699-709.

Inoue, Shimpei, Akihiko Ito, and Chinatsu Yonezawa. 2020. 'Mapping Paddy fields in Japan by using a Sentinel-1 SAR time series supplemented by Sentinel-2 images on Google Earth Engine', *Remote Sensing*, 12: 1622.

Jensen, John R. 1996. *Introductory digital image processing: a remote sensing perspective* (Prentice-Hall Inc.).

Karakuş, Can Bülent. 2019. 'The impact of land use/land cover (LULC) changes on land surface temperature in Sivas City Center and its surroundings and assessment of Urban Heat Island', *Asia-Pacific Journal of Atmospheric Sciences*, 55: 669-84.

Lambin, E., and H. Geist. 2006. 'Land-Use and Land-Cover Change: Local Processes and Global Impacts.' in.

Lee, Jong-Sen, Mitchell R Grunes, Thomas L Ainsworth, Li-Jen Du, Dale L Schuler, and Shane R Cloude. 1999. 'Unsupervised classification using polarimetric decomposition and the complex Wishart classifier', *IEEE Transactions on Geoscience and Remote Sensing*, 37: 2249-58.

Lillesand, Thomas, Ralph W Kiefer, and Jonathan Chipman. 2015. *Remote sensing and image interpretation* (John Wiley & Sons).

Lim, Kevin, Paul Treitz, Michael Wulder, Benoît St-Onge, and Martin Flood. 2003. 'LiDAR remote sensing of forest structure', *Progress in physical geography*, 27: 88-106.

Lu, Dengsheng, and Qihao Weng. 2007. 'A survey of image classification methods and techniques for improving classification performance', *International journal of Remote sensing*, 28: 823-70.

Masri, T., Mohamad Khawlie, and Ghaleb Faour. 2002. 'LAND COVER CHANGE OVER THE LAST 40 YEARS IN LEBANON', 3.

Mather, Paul M, and Magaly Koch. 2011. *Computer processing of remotely-sensed images: an introduction* (John Wiley & Sons).

Mauro, Giovanni. 2020. 'Rural–urban transition of Hanoi (Vietnam): Using Landsat imagery to map its recent peri-urbanization', *ISPRS International Journal of Geo-Information*, 9: 669.

Mora, Brice, Nandin-Erdene Tsendbazar, Martin Herold, and Olivier Arino. 2014. 'Global Land Cover Mapping: Current Status and Future Trends.' in Ioannis Manakos and Matthias Braun (eds.), *Land Use and Land Cover Mapping in Europe: Practices & Trends* (Springer Netherlands: Dordrecht).

Munthali, Maggie G, Joel Ongego Botai, Nerhene Davis, and Abiodun Morakinyo Adeola. 2019. 'Multi-temporal analysis of land use and land cover change detection for Dedza district of Malawi using geospatial techniques'.

Phinn, Stuart R, Chris M Roelfsema, and Peter J Mumby. 2012. 'Multi-scale, object-based image analysis for mapping geomorphic and ecological zones on coral reefs', *International journal of Remote sensing*, 33: 3768-97.

Qian, Shenhua, Danya Qin, Xue Wu, Siwei Hu, Linyu Hu, Dunmei Lin, Liang Zhao, Kankan Shang, Kun Song, and Yongchuan Yang. 2020. 'Urban growth and topographical factors shape patterns of spontaneous plant community diversity in a mountainous city in southwest China', *Urban Forestry & Urban Greening*, 55: 126814.

Rich, P. M., & Dubayah, R. 2012. ' Remote sensing of wetlands: Applications and advances. Wetlands', *Sustainability*, 932: 237-45.

Roy, Parth, and Arijit Roy. 2010. 'Land Use and Land Cover Change: A Remote Sensing & GIS Perspective', *Journal of the Indian Institute of Science*, 90: 489-502.

Seto, Karen C, Burak Güneralp, and Lucy R Hutyra. 2012. 'Global forecasts of urban expansion to 2030 and direct impacts on biodiversity and carbon pools', *Proceedings of the National Academy of Sciences*, 109: 16083-88.

Skog, Kristine Lien, and Margrete Steinnes. 2016. 'How do centrality, population growth and urban sprawl impact farmland conversion in Norway?', *Land use policy*, 59: 185-96.

Sobrino, José A, Juan C Jiménez-Muñoz, and Leonardo Paolini. 2004. 'Land surface temperature retrieval from LANDSAT TM 5', *Remote Sensing of Environment*, 90: 434-40.

Spruce, Joseph, John Bolten, Ibrahim N Mohammed, Raghavan Srinivasan, and Venkat Lakshmi. 2020. 'Mapping land use land cover change in the Lower Mekong Basin from 1997 to 2010', *Frontiers in environmental science*, 8: 21.

Thenkabail, Prasad S, Murali Krishna Gumma, Pardhasaradhi Teluguntla, and AM Irshad. 2014. 'Hyperspectral remote sensing of vegetation and agricultural crops', *Photogrammetric Engineering & Remote Sensing (TSI)*, 80: 695-723.

Ulaby, Fawwaz T, Richard K Moore, and Adrian K Fung. 1986. 'Microwave remote sensing: Active and passive. Volume 3-From theory to applications'.

Unal, Muge, and Cengiz Uslu. 2018. ''Evaluating and Optimizing Urban Green Spaces for Compact Urban Areas: Cukurova District in Adana, Turkey.'' In *ISPRS International Journal of Geo-Information*.

Wang, Shuren, Lanlan Guo, Bin He, Yanli lyu, and Tiewei Li. 2020. 'The stability of Qinghai-Tibet Plateau ecosystem to climate change', *Physics and Chemistry of the Earth, Parts A/B/C*, 115: 102827.

Wehr, Aloysius, and Uwe Lohr. 1999. 'Airborne laser scanning—an introduction and overview', *ISPRS Journal of photogrammetry and remote sensing*, 54: 68-82.

Weng, Qihao, Dengsheng Lu, and Jacquelyn Schubring. 2004. 'Estimation of land surface temperature–vegetation abundance relationship for urban heat island studies', *Remote Sensing of Environment*, 89: 467-83.

Wulder, Michael A, Joanne C White, Thomas R Loveland, Curtis E Woodcock, Alan S Belward, Warren B Cohen, Eugene A Fosnight, Jerad Shaw, Jeffrey G Masek, and David P Roy. 2016. 'The global Landsat archive: Status, consolidation, and direction', *Remote Sensing of Environment*, 185: 271-83.

Yang, Jun, Peng Gong, Rong Fu, Minghua Zhang, Jingming Chen, Shunlin Liang, Bing Xu, Jiancheng Shi, and Robert Dickinson. 2013. 'The role of satellite remote sensing in climate change studies', *Nature climate change*, 3: 875-83.

Yılmaz, Rüya. 2010. 'Monitoring land use/land cover changes using CORINE land cover data: a case study of Silivri coastal zone in Metropolitan Istanbul', *Environmental monitoring and assessment*, 165: 603-15.

Yu, Guangting, Tongwen Liu, Qi Wang, Tao Li, Xiujing Li, Guanhan Song, and Yougui Feng. 2022. 'Impact of Land Use/Land Cover Change on Ecological Quality during Urbanization in the Lower Yellow River Basin: A Case Study of Jinan City', *Remote Sensing*, 14: 6273.

Zadbagher, Elaheh, Kazimierz Becek, and Suha Berberoglu. 2018. 'Modeling land use/land cover change using remote sensing and geographic information systems: case study of the Seyhan Basin, Turkey', *Environmental monitoring and assessment*, 190: 494.

CURRICULUM VITAE

Mwila LAMPI, completed my primary, secondary, and high school education, I earned a bachelors degree from Cukurova University, Faculty of Engineering, Department of Civil Engineering, in 2016-2021. In 2022, I started my Masters at Cukurova University, Institute of Natural and Applied Sciences, Department of Remote Sensing and Geographic Information Systems.